DOCTORAL (PhD) DISSERTATION

University of Sopron

Roth Gyula Doctoral School of Forestry and Wildlife Management

Spatial statistics analyses and modeling of land cover and land use change in the Prishtina region

Ferat Krasniqi

Supervisor:
Dr. KIRÁLY, Géza
associate professor

Sopron,
2025

Spatial statistics analyses and modeling of land cover and land use change in the Prishtina region

Written by in order to obtain Doctoral (PhD) degree:

Ferat Krasniqi

_____

Prepared by the University of Sopron
ROTH GYULA DOCTORAL SCHOOL

Supervisor(s): Dr. KIRÁLY, Géza
associate professor

Acceptance recommended (yes / no)

_____ _____
(signature) (signature)

I propose to accept the dissertation as a reviewer (yes / no)

1st Reviewer (Dr _____) yes / no _____
(signature)

2nd Reviewer (Dr _____) yes / no _____
(signature)

(Opt. 3rd Reviewer (Dr _____) yes / no) _____
(signature)

Result of the public dissertation defense: _____%

Sopron, ____day _____month _____ year _____
Chairman of the Public Defence Committee

Qualification of the doctoral (PhD) diploma _____

_____
Chairman of the UDHC

DECLARATION

I, the undersigned **Ferat Krasniqi** by signing this declaration declare that my PhD thesis entitled **Spatial statistics analyses and modeling of land cover and land use change in the Prishtina region** was my own work; during the dissertation I complied with the LXXVI and the rules of the doctoral dissertation prescribed by the Roth Gyula Doctoral School, especially regarding references and citations.[1]

Furthermore, I declare that during the preparation of the dissertation I did not mislead my supervisor(s) or the programme leader with regard to the independent research work.

By signing this declaration, I acknowledge that if it can be proved that the dissertation is not self-made or the author of a copyright infringement is related to the dissertation, the University of Sopron is entitled to refuse the acceptance of the dissertation.
I further declare that I am not in the process of obtaining a doctoral degree in the same discipline, that I am not in the process of having my doctoral degree revoked, and that I have not had a previously awarded doctoral degree revoked within 5 years.
Refusing to accept a dissertation does not affect any other (legal, civil law, misdemeanour law, criminal law) consequences of copyright infringement.

Sopron, 20....year……..month…….day

……..

PhD candidate

[1] **Act LXXVI of 1999** Article 34 (1) Anyone is entitled to quote details of the work, to the extent justified by the nature and purpose of the recipient work, by designating the source and the author specified therein.

Article 36 (1) Details of publicly lectures and other similar works, as well as political speeches, may be freely used for the purpose of information to the extent justified by the purpose. For such use, the source, along with the name of the author, shall be indicated, unless this is impossible.

List of Tables

List of Figures

List of Abbreviations

ANN — Artificial Neural Network

ARC — Annual Rate of Change

AVHRR — Advanced Very high Resolution Radiometer

BN — Band Number

CA — Cellular Automata

CCRS — Canada Centre for Remote Sensing

CFMask — C Function of Mask (cloud and shadow detection algorithm, also called Fmask)

CLC — CORINE Land Cover

CNES — Centre National d'Études Spatiales (French Space Agency)

DEM — Digital Elevation Model

ENVI — Environment for Visualizing Images (remote sensing software)

ESA — European Space Agency

ERTS — Earth Resources Technology Satellite (later renamed Landsat 1)

ETM+ — Enhanced Thematic Mapper Plus (Landsat 7 sensor)

EOSDIS — Earth Observing System Data and Information System (NASA)

GIS — Geographic Information System

IGBP — International Geosphere-Biosphere Programme

IR — Infrared

JM — Jeffries–Matusita

KC — Kappa Coefficient (Cohen's Kappa)

LCCS — Land Cover Classification System

LCLU — Land Use/Land Cover

MD — Minimum Distance (classifier)

ML — Maximum Likelihood (classifier)

MLP — Multilayer Perceptron

MODIS — Moderate Resolution Imaging Spectroradiometer

MOLUSCE — Modules for Land Use/Cover Change Simulation (QGIS plugin)

NIR — Near-Infrared

OA — Overall Accuracy

OLI — Operational Land Imager (Landsat 8/9 sensor)

PA — Producer's Accuracy

QA_PIXEL — Quality Assessment Pixel band

QGIS — Quantum Geographic Information System (open-source GIS software)

RGB — Red, Green, Blue (composite bands)

RBF — Radial Basis Function (SVM kernel)

SPOT — Satellite Pour l'Observation de la Terre (French Earth observation satellites)

SVM — Support Vector Machine

SWIR — Short-Wave Infrared

TIR — Thermal Infrared (spectral region)

TIRS — Thermal Infrared Sensor (Landsat 8/9)

TM — Thematic Mapper (Landsat 4/5 sensor)

UA — User's Accuracy

USGS — U.S. Geological Survey

UTM — Universal Transverse Mercator

UV — Ultraviolet

WGS84 — World Geodetic System 1984 (reference coordinate system)

WL — Wavelength

Kivonat

Ez a kutatás a földborítás és a földhasználat változásainak területi statisztikáit elemzi 2001 és 2019 között, valamint a 2019 és 2039 közötti változások előrejelzését a koszovói Prishtina régióban. A Landsat TM5, ETM+7 és OLI8 műholdérzékelők használatával, valamint a felügyelt osztályozási módszerrel távérzékelési technológiát alkalmaztak az LCLU-térképek létrehozásához: 2001-re, 2009-re és 2019-re. Négy algoritmust teszteltünk, és egy pontosságértékelő eszközt használtunk a teljesítményük értékelésére. Összességében a Support Vector Machine with Radial Basis Function (SVM-RBF) osztályozója volt a legpontosabb 2001-ben, 87,21%-os OA-val és 0,83-as KC-vel. A neurális hálózat (NN) osztályozója volt a legpontosabb 2009-ben, 87,21%-os OA-val és 0,83-as KC-vel, 2019-ben pedig a legpontosabb 81,86%-os OA-val és 0,77-es KC-vel.

Az LCLU-térképek elemzése jelentős elmozdulásokat mutatott ki, a mezőgazdasági osztályon belül 111,25 km²-es veszteséggel, a városi osztályon belül pedig 47,71 km²-es növekedéssel a teljes vizsgálati időszakban, 2001 és 2019 között, a gyors urbanizáció és az ipari terjeszkedés hatására. A Cellular Automata (CA) és a Mesterséges Neurális Hálózat (ANN) modellek használata az LCLU változásainak előrejelzésére azt mutatja, hogy a városok továbbra is 20,63 km²-rel, az erdők 2,87 km²-rel nőnek, a víztestek pedig további 1,39 km²-t veszítenek 2039-re. A tanulmány rávilágít az LCLU-politikák nyomon követésének és előrejelzésének hatékonyságára a fenntartható földgazdálkodási hatások mérséklése érdekében a városok környezeti hatásainak csökkentésében.

Abstract

This research analyses the spatial statistics of land cover and land use (LCLU) changes from 2001 to 2019, as well as the prediction of changes from 2019 to 2039 in Prishtina region, Kosovo. By using Landsat TM5, ETM+7, and OLI8 satellite sensors, along with the supervised Machine Learning classification method, remote sensing technology was used to generate the LCLU maps into three times: 2001, 2009, and 2019. We tested four algorithms and used an accuracy assessment tool to evaluate their performance. Overall, the Support Vector Machine with Radial Basis Function (SVM-RBF) classifier was the most accurate in 2001, with an overall accuracy (OA) of 87.21% and a kappa coefficient (KC) of 0.83. The Neural Network (NN) classifier was the most accurate in 2009, with an OA of 87.21% and a KC of 0.83, and the most accurate in 2019 with an OA of 81.86% and a KC of 0.77.

Analysis of LCLU maps revealed significant shifts, with a loss of 111.25 km² in agricultural class and a gain of 47.71 km² in urban class for the whole study period, 2001 to 2019, driven by rapid urbanisation and industrial expansion. Using Cellular Automata (CA) and Artificial Neural Network (ANN) models to predict changes in LCLU shows that cities will continue to grow by 20.63 km², forests will gain by 2.87 km^2, and water bodies will lose another 1.39 km^2 by 2039. The study highlights the effectiveness of monitoring and predicting LCLU changes for sustainable land management policies to mitigate environmental impacts and support balanced urban development.

Table of contents

1. INTRODUCTION

The cartographic representation of LCLU provides a comprehensive depiction of the materials present on the Earth's surface and the extent of human utilisation, systematically categorised using a well-defined categorization system. These maps are not fixed illustrations but rather fluid portrayals of many natural zones, encompassing forests, meadows, bodies of water, and landscapes influenced by human activity. Every map accurately records these zones at specific time intervals. The escalating frequency of anthropogenic alterations to the Earth's surface underscores the necessity for the creation of dynamic LCLU maps to effectively track and adapt to these transformations.

These maps have become more significant, finding application in several domains, including urban planning, agriculture, forestry, environmental conservation, and forecasting future land utilisation patterns. The development and progress of geospatial technologies, including Remote Sensing and Geographic Information Systems (GIS), have significantly enhanced the efficiency and accuracy of mapping dynamic landscapes. Remote sensing allows for non-invasive data collection through the use of sensors deployed on satellites, aircraft, or unmanned aerial vehicles. The subject matter is categorised into two primary approaches: active and passive. Active remote sensing involves the emission of a signal towards a target and the subsequent detection of the reflected signal. Technologies such as Radar and LiDAR are used to illustrate this point. Passive remote sensing uses sunlight to capture the emitted or reflected solar radiation released by objects on Earth. The Landsat satellite's multispectral sensors are a noteworthy illustration of this methodology.

Since its launch in 1972, the Landsat programme has served as the primary source of satellite-based earth observation, providing unmatched and continuous documentation of the Earth's surface. The accessibility of the Landsat data repository, along with progress in image processing methodologies, digital classification approaches, and analytical instruments, has empowered researchers to precisely monitor and quantify alterations in land utilisation with remarkable accuracy and comprehensiveness.

This thesis aims to enrich the academic field by documenting the evolution of land use in the Prishtina administrative region over several decades. This methodology utilises the Landsat archive as the primary data source and employs supervised digital image classification methods and post-classification comparison tools to authenticate changes in

different land use categories. This study investigates the alterations in land use within the region during three distinct time intervals: 2001, 2009, and 2019, enabling a sequential analysis. This scholarly endeavour seeks to conduct a comprehensive analysis of the region's trajectory of growth and its ecological repercussions.

2. AIM AND SCOPE

The objective of this study is to analyse and assess the general trends of changes in LCLU in the Prishtina Region over a period of 18 years. I used in my Thesis Landsat satellite images, remote sensing change detection, and a modelling-based technique for data analysis. To achieve the aim of this study, the following goals will be pursued:

1. To provide LCLU maps for the designated research area at defined time intervals (2001, 2009, and 2019).
2. To use supervised image classification methods using different algorithms: Maximum Likelihood and Minimum Distance algorithms, Support Vector Machine and Neural Network.
3. To evaluate the precision of the categorization outcomes and methodologies used in this investigation.
4. To examine the patterns and dynamics of changes in LCLU throughout certain time periods.
5. To assess the benefits and drawbacks of various LCLU categories, analyse the changes in LCLU throughout time.

2.1 RESEARCH QUESTIONS

The primary objective of this study is to examine the changes in LCLU in the Prishtina region. To do this, the following research questions were formulated:

1. Did the land cover and use undergo substantial changes within the chosen study periods?
2. What was the spatial distribution of LCLU growth observed throughout the study periods?
3. What was the influence of various land cover categories on the growth of a certain land cover or land use type in the designated research region?
4. What is the level of reliability of Landsat satellite imagery for monitoring changes in LCLU in the specified region?
5. What type of classification method is the best to estimate LCLU?
6. Was the categorization and change detection approach sufficient for the purpose of mapping and identifying changes?

3. LITERATURE OVERVIEW

3.1 LAND COVER AND LAND USE CHANGE: DEFINITIONS

It is helpful to have a thorough understanding of LCLU in order to have a deeper understanding of the concepts and meanings of these terms. Land cover refers to the visible (bio) physical layer that covers the surface of the Earth. It specifically includes the identification of plant and anthropogenic characteristics (Gregorio & Jansen, 1998). According to Fisher, Comber, and Wadsworth (2005), the reflected energy levels that result from the interaction with electromagnetic emissions determine the visual representation of the Earth's surface in a satellite image. The landscape comprises many surface elements, including flora, grassland, bare ground, and bodies of water such as lakes and seas. Land use refers to the specific arrangements, actions, and inputs that people engage in to generate, alter, or preserve a certain form of land cover. Furthermore, several studies and initiatives have shown significant disparities in the core principles and criteria used to develop a LCLU categorization system. In their study, Fisher et al. (2005) examine the ambiguity notation of the land cover and land use words, exploring their characteristics, underlying implications, and sources of misunderstanding. Despite variations in fundamental principles, there are instances when the classification of land cover aligns with land use, such as in the case of the pasture class (Fisher et al., 2005). While land cover and land use words are sometimes used interchangeably in land categorization systems, it is widely argued that they have separate meanings.

Land cover types are crucial for comprehending the Earth's diverse physical characteristics and monitoring temporal alterations. Land use focuses on the human aspect of the landscape, highlighting the intended purpose and function of certain areas of land. Rindfuss et al. (2004) define land use as a broad spectrum of activities, including residential, commercial, and industrial purposes, as well as agricultural, leisure, and conservation efforts. Land use classifications offer valuable insight into the social and cultural factors that shape the landscape. Land use classifications establish a connection between the physical attributes of land cover and the human aspirations and actions that influence the landscape.

An in-depth comprehension of LCLU change dynamics is essential for comprehending the transformations occurring in our world. According to Turner et al. (2015), land cover change refers to alterations in the physical characteristics of the Earth's surface. These alterations

may manifest as deforestation, urban expansion, wetland depletion, shifts in plant cover, or variations in surface materials. These alterations, whether occurring naturally or caused by human activities, are frequently noticeable and can have significant ecological and environmental consequences. Rindfuss et al. (2004) define land use change as an alteration in the purpose and land use. Examples of this include agricultural intensification, urbanisation, reforestation, and changes in land management practices. These advancements demonstrate the ability of human civilizations to adapt and respond to changing needs and external factors.

Satellite and aerial imagery have become essential instruments for monitoring and assessing alterations in LCLU. Lu and Weng (2007) highlight the significance of remote sensing in acquiring data, objective monitoring without physical contact, cost-efficiently, rapidity, measuring differences, and examining alterations in the landscape. These technologies can be utilised for land management, urban planning, resource allocation, and environmental impact assessments. They provide global observation and documentation of the dynamic interplay between human activities and the natural environment, enabling the study of LCLU trends and their associated environmental consequences.

Due to the intricate nature of land systems and the ongoing interactions between humans and the environment, the task of identifying and categorising LCLU can be challenging. Olofsson et al. (2014) argue that the use of standardised classification methods and the integration of geographical data are essential for addressing these challenges. Such standardisation not only enhances the capacity to compare and maintain consistency in evaluations and reporting, but it also facilitates the harmonisation of data obtained from many sources and jurisdictions. The diverse and situation-dependent nature of land systems, along with the ever-changing dynamics of human-environment interactions, frequently pose difficulties. It is crucial to overcome these challenges in order to generate comprehensive and coherent knowledge about LCLU. This will enable more informed decision-making in the fields of environmental management, urban planning, and sustainable development.

Both natural and socio-economic phenomena have altered the land cover throughout history. Understanding ecological processes and implementing long-term sustainable management practices are essential for identifying and examining changes in land cover. The rapid increase in population and economic development have led to the swift urbanisation of the Earth's land area. This process has resulted in the transformation of land cover into other

land uses, including residential and leisure areas, industrial zones, business and transit areas, agricultural areas, and more. Campbell et al. (2003) provide illustrations of land use changes and their underlying causes, as well as the factors that drive these changes, resulting from the interplay between biophysical and social processes. These changes occur at various sizes (global, regional, and local) and over different periods of time and geographical areas. Furthermore, Turner, Meyer, and Skole (1994) depicted an illustrationand examined the influence of human driving variables and their interplay, which may result in changes in LCLU.

3.2 LAND COVER AND LAND USE CLASSIFICATION SYSTEMS

Classification is the process of organising objects into groups or sets based on their relationships, as defined by Sokal (1974). According to Jansen and Di Gregorio (2002), the term "classification system" refers to a systematic framework that includes the names of classes, the criteria used to distinguish them, and the connections between the classes. Furthermore, it is imperative to establish explicit and well-defined parameters for class distinctions, which should be unambiguous, quantifiable, and grounded in objective criteria. The legend is created by categorising a specific area using a certain map size and a unique dataset (United Nations Programme & Food and Agriculture Organization [FAO], 2000). The endeavours to establish a systematic and orderly framework for categorising land cover types and land use are in their early stages.

To ensure the precision and effectiveness of these systems, both global and local initiatives have been established, each making substantial contributions to the mapping and monitoring of our environment. Among the most influential global initiatives, the United Nations' Land Cover Classification System (LCCS) offers a standardised framework for characterising land cover through a hierarchical approach (Di Gregorio & Jansen, 2005). This system provides a universal language for land cover classification, facilitates cross-border analyses, and harmonises assessments. LCCS plays a pivotal role in global environmental assessments, ensuring consistency and comparability in land cover mapping. The IGBP classification system is significant for its focus on characterising LCLU within the context of Earth's major ecosystems (Loveland et al., 2000). By identifying broad categories, such as forests, croplands, and urban areas, this system supports global-scale assessments of ecosystem changes, making it an invaluable tool for comprehending the Earth's evolving landscape.

In recent years, remote sensing-based classification systems have gained prominence in the fields of LCLU mapping. These systems use the spectral, spatial, and temporal data that satellite and aerial imagery provide to classify and track changes in land cover. Common Machine Learning algorithms include Maximum Likelihood, Support Vector Machines, and Random Forest (Lu & Weng, 2007).

Local initiatives, frequently spearheaded by regional governments and agencies, are crucial in adapting LCLU classification systems to address particular regional needs. One notable example is the Corine Land Cover (CLC) program, which the European Environment Agency developed. The CLC system offers a highly detailed nomenclature encompassing a wide array of land cover classes and has been instrumental in environmental monitoring and management within Europe (Büttner et al., 2021). In the United States, the Anderson Land Use Land Cover Classification System is widely employed. This systematic approach classifies land cover based on hierarchical categories and is used by organisations like the U.S. Geological Survey to generate land cover datasets (Anderson et al., 1976).

In conclusion, global and local initiatives in LCLU classification systems, such as worldcover (European Space Agency [ESA], n.d.) are mutually reinforcing components of our endeavours to understand and manage the Earth's ever-evolving landscape. Yang et al. (2017) and Nedd et al. (2021) conducted a comprehensive analysis of LCLU classification systems that utilise optical remote sensing data. These systems are categorised into three groups based on their scale and level of cartographic detail: national, regional, and global. The LCCS are displayed in Table 1.

Category	Classification System	Year	Location
National	National Land Cover Data Classification System	1992; 2001; 2006; 2011	USA
	National Land Survey Classification System	1984; 2007	China
	National Institute of Statistics, Geography and Informatics	1993; 2000	Mexico
	South African Standard Land Cover Classification System	1996	South African
	US National Vegetation Classification Standard	1997	United States
	National Forest Inventory Land Cover Classification Scheme	1999	Canada
	National Land Use Database (NLUD)	2001	United Kingdom

	Sistema de Información de Ocupación del Suelo en España (SIOSE)	2000	Spain
	The MapBiomas LULC Classification Scheme	2020	South Africa
	ALUM Classification System	2005	Australia
	New Zealand Land use Class	1984	New Zealand
Regional	CORINE Land Cover	1990/2000/2006 /2012/2018	Europe
	AFRICOVER Land Cover Classification System	1995/2002	Africa
	AARS Land Cover Classification	1999	Asia
	North American Land Change Monitoring System Legend	2005	North America
Global	USGS Land Use/Land Cover Classification Systems (National)	1972/1976	USGS
	Land Cover Classification System	1996	FAO
	International Geosphere-Biosphere Programme-Data and Information System	1996	IGBP
	EarthSat GeoCover Land Cover Legend	1990	EarthSat
	UNEP/FAO Land Cover Legend	1993	UNEP/FAO
	GOFC/GOLD Land and Forest Cover Classification System	1998	CEOS
	UMD Global Land Cover Classification	1998	UMD

Table 1. Land Cover Classification System (LCCS) framework

Kosovo has not yet established or put into effect a national classification system for LCLU, as indicated in Table 1. Nevertheless, on a regional scale, it has established and executed the CORINE Land Cover (CLC) classification system as part of the collaborative European project (GMES). The European Commission launched the CORINE (coordination of information on the environment) Land Cover programme in 1985 to address a range of environmental issues (Büttner et al., 2021). Using the CLC terminology, inventories have been created for the years 1990, 2000, 2006, 2012, and 2018. Additionally, inventories of the changes in the CLC for these years have also been generated. The CLC terminology comprises three hierarchical levels, encompassing a combined total of 44 groups for LCLU. The CLC employs a minimum mapping unit (MMU) of 25 hectares (ha) and a minimum width of 100 meters for linear features. Additionally, it detects changes in land cover using a minimum MMU mapping unit of 5 hectares (ha) (Büttner et al., 2021).

3.3 REMOTE SENSING APPLICATION FOR LAND COVER/USE MAPPING

Remote sensing (RS) is defined by multiple definitions. Remote sensing is the practice of gathering information about the characteristics of objects on the Earth's surface using data received from aircraft and satellites (Schowengerdt, 2006). The term "remote" pertains to the act of observing something from a distance without any direct physical engagement. Sensing involves the use of sensor systems, such as those present on aircraft or satellites, to detect and document the energy that is either reflected or emitted by a target. The primary objective of remote sensing is to get, analyse, and interpret data in order to gain a more profound comprehension of the Earth's traits, properties, and temporal fluctuations. It offers a unique perspective by allowing the exploration of physically inaccessible regions.

According to reliable sources, there are numerous essential ideas that underpin the field of remote sensing. Jensen (2007) and Campbell & Wynne (2015) emphasise the utmost significance of the electromagnetic spectrum, which encompasses a wide range of wavelengths, such as radio waves, microwaves, infrared (IR), visible light, ultraviolet, X-rays, and gamma rays. Different sensors are purposefully designed to capture various portions of this spectrum, allowing for a variety of distant sensing applications. Spatial resolution and spectral resolution are two crucial parameters that have a significant impact on the quality and richness of remote sensing data. Campbell (2015) and Lillesand, Kiefer, and Chipman (2015) emphasised this. The choice of platforms for data gathering is a critical factor, encompassing a range of choices such as satellites, aircraft, unmanned aerial vehicles, balloons, and ground-based sensors. The precise objectives of the research will determine the platform choice (Jensen, 2007; Mather, 2016).

Many sources have explained that remote sensing uses a wide range of techniques and technologies to collect data. According to Campbell and Wynne (2011), passive remote sensing involves the collection of naturally emitted electromagnetic radiation. This technique is especially suitable for applications like optical imaging, where sunlight is used to produce images of the Earth's surface. Jensen (2007) and Mather & Koch (2011) describe active remote sensing as involving the emission of radiation and subsequent detection of the returning signal. Exemplary instances of this can be observed in the utilisation of radar and LiDAR systems, which are utilised for the objectives of cartography and target identification. Lillesand, Kiefer, and Chipman (2015) state that multispectral and hyperspectral imaging techniques employ multiple wavelength bands to collect information

about the Earth's surface. Although multispectral sensors have a limited number of bands, hyperspectral sensors offer a more complex and detailed spectral signature. According to Jensen (2007) and Mather and Koch (2011), IR and thermal imaging are crucial for achieving specific goals like tracking the health of vegetation, mapping heat patterns, and spotting anomalies.

The utilisation of remote sensing encompasses a wide range of fields and exerts a substantial impact on various disciplines, as seen by the references. Remote sensing plays a vital role in agriculture as it enables farmers to precisely monitor the condition of their crops, estimate crop yields, and effectively allocate resources (Campbell & Wynne, 2011; Mather & Koch, 2011). Environmental monitoring is a crucial technique used to observe alterations in ecosystems, identify deforestation, assess air and water quality, and supervise the administration of natural resources (Jensen, 2007; Campbell, 2015). Remote sensing applications are essential for urban planning and development since they monitor the growth of cities, the construction of infrastructure, and the risks of disasters. This aids in the development of sustainable urban blueprints (Campbell, 2015; Lillesand et al., 2014). The field of remote sensing is especially good at collecting valuable data on the Earth's surface, atmosphere, and water bodies while also conducting systematic environmental monitoring over large geographic areas (Khatami, Mountrakis, & Stehman, 2016).

Geological exploration uses remote sensing to carry out geological mapping, mineral exploration, and hazard assessment. This supports the efficient use of resources and improves our understanding of geological phenomena (Jensen, 2007; Lillesand et al., 2014). As Mather (2016) points out, remote sensing is essential for disaster management because it quickly and accurately provides information to gauge the extent of damage and organise rescue operations.

The field of remote sensing is continuously advancing as a result of advancements in sensor technology, data processing, and Machine Learning algorithms. Future advancements will involve integrating data from several sensors to enhance decision-making by providing more extensive information. The utilisation of small satellites and drones is on the rise, enabling the acquisition of high-resolution and frequent data. Moreover, the utilisation of remote sensing in domains such as climate monitoring, cultural asset protection, and wildlife conservation is on the rise, underscoring its growing significance in our rapidly evolving world.

3.3.1 ELECTROMAGNETIC SPECTRUM

Electromagnetic radiation (EMR) is the form in which energy is transmitted. The sun, the Earth's thermal radiation, and active platform sensors are all sources of this energy. Waves produced by electromagnetic fields (electric and magnetic fields) make up electromagnetic radiation (EMR). These waves travel across space at the speed of light and possess both velocity and energy. In order to comprehend the remote sensing process, it is crucial to consider two key attributes of electromagnetic radiation (EMR): wavelength and frequency (Canada Centre for Remote Sensing [CCRS], 2019). The wavelength is the spatial interval between consecutive peaks of a wave, and it can be quantified in meters (m) or smaller units such as micrometers (μm, 10-6 meters) or nanometers (nm, 10-9 meters). On the other hand, frequency refers to the number of complete oscillations of a wave passing through a specific point within a given time period, and it is measured in hertz (Hz). The relationship between frequency and wavelength is inseparable: as frequency increases, wavelength decreases, and vice versa. The EMR is categorized into several wavelength zones of the electromagnetic spectrum (EMS) based on this inverse relationship (Albertz, 2007; SEOS Project, n.d.). The EMS is shown in Figure 1.

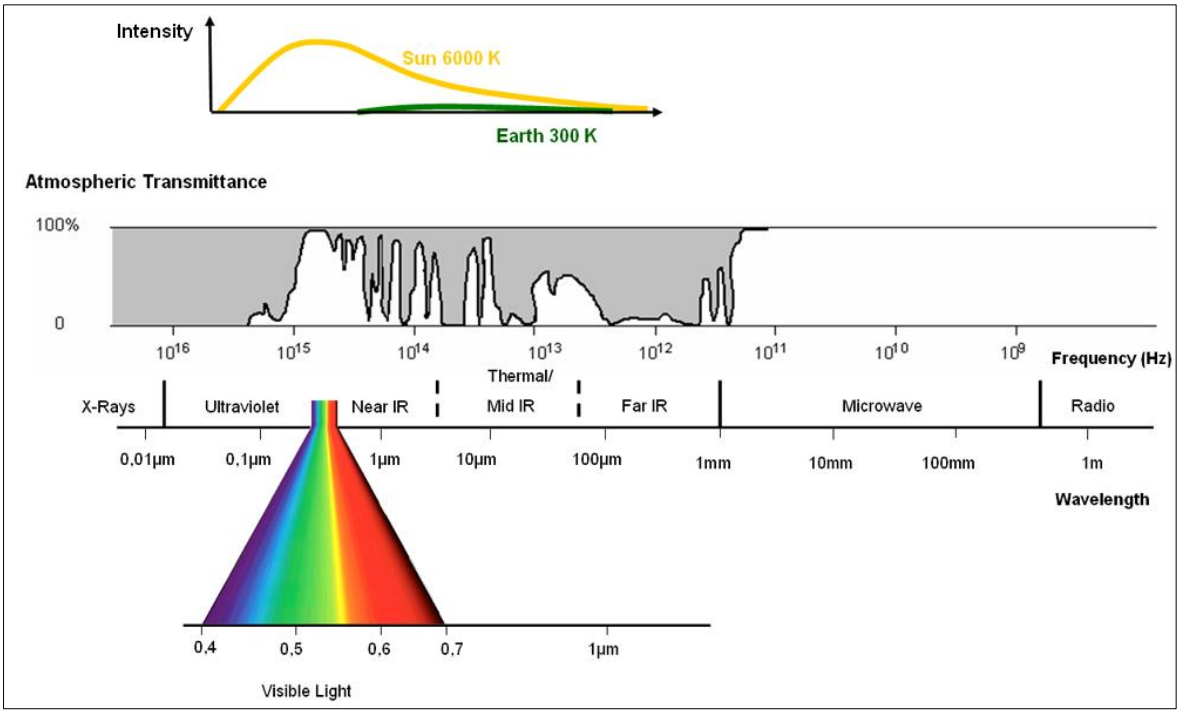

Figure 1. The electromagnetic spectrum. Adapted from Einführung in die Fernerkundung: Grundlagen der Interpretation von Luft- und Satellitenbildern (Albertz, 2007), via SEOS Project (n.d.), https://seos-project.eu/remotesensing/remotesensing-c01-p01.html

The various parts of the electromagnetic spectrum (EMS) are classified based on their wavelength and frequency. These sections are designated as follows: gamma rays, x-rays, ultraviolet (UV) radiation, visible (light) radiation, IR, microwaves, and radio waves. In the field of remote sensing, there are several segments within the electromagnetic spectrum (EMS) that are valuable and relevant for the collection of geographical data.

The ultraviolet (UV) spectrum, with a wavelength of 0.1 μm, is valuable for identifying rocks and minerals on the Earth's surface that reflect visible light when exposed to UV radiation (CCRS, 2019). The majority of geographical data captured using remote sensing is obtained in the visible and IR regions of the electromagnetic spectrum (EMS). The light that our eyes sense is part of the visible spectrum, which is the smallest section of the electromagnetic spectrum. The visible light spectrum, which corresponds to different colours, spans from about 0.4 μm to 0.7 μm. Specifically, violet light ranges from 0.4 to 0.446 μm, blue light ranges from 0.446 to 0.500 μm, green light ranges from 0.500 to 0.578 μm, yellow light ranges from 0.578 to 0.592 μm, orange light goes from 0.592 to 0.620 μm, and red light ranges from 0.620 to 0.7 μm (CCRS, 2019). The subsequent segment of the electromagnetic spectrum that encompasses longer wavelengths is referred to as the IR spectrum. The IR wavelengths may be categorised into two forms: reflected IR (near IR, mid IR), which spans from 0.7 μm to 3 μm, and Thermal IinfraRed (TIR), which ranges from 3 μm to 14 μm (Liu & Mason, 2016). The reflected IR spectrum is very valuable for classifying plant types, detecting deforestation, and monitoring vegetation health.

Satellites with thermal sensors in the TIR region are able to identify and capture the heat energy that the Earth's surface emits. Two examples of remote sensing (RS) applications that use the TIR spectrum are the mapping of land surface temperature and the detection of forest fires. The microwave segment of the electromagnetic spectrum has the greatest range of wavelengths, ranging from around 1mm to 1 m. This segment holds significant importance in remote sensing applications owing to its unique features. Microwaves are impervious to weather conditions and have the ability to pierce through clouds, fog, dust, and precipitation. This allows them to continuously monitor the Earth's surface without any hindrance. As solar radiation travels towards the earth's surface, it undergoes three interactions in the atmosphere: scattering, absorption, and transmission.

3.3.2 ATMOSPHERIC SCATTERING

Scattering occurs when the sun's rays come into contact with particles or gas molecules in the atmosphere, resulting in the redirection of electromagnetic energy from its initial trajectory. The atmospheric distribution is influenced by several elements, including the wavelength of radiation, the concentration of particles or gases, and the distance travelled by the radiation in the atmosphere. Rayleigh scattering occurs when solar radiation interacts with minuscule dust particles and molecules of nitrogen (NO_2) and oxygen (O_2) that are smaller than the wavelength of light. Rayleigh scattering distorts the spectrum properties of visible light, hence adversely impacting the digital categorization of multispectral images. Mie scattering occurs when the wavelength of electromagnetic radiation matches the dimensions of particles present in the environment, such as aerosols, gases, water vapour, and dust. This interaction between the radiation and particles leads to Mie scattering. The Mie distribution primarily impacts the spectrum with longer wavelengths, ranging from near UV to mid-IR. It is prevalent in the lower regions of the atmosphere, where bigger and more plentiful particles are present. Additionally, it prevails under overcast meteorological circumstances. The clouds seen in the image captured by optical sensors exemplify non-selective scattering, which is the third kind of atmospheric scattering. Scattering can occur when particles, such as water droplets and dust particles, have a size much greater than the wavelength of the radiation (Bakker et al., 2001).

3.3.3 ATMOSPHERIC ABSORPTION

The molecules in the atmosphere partially absorb electromagnetic radiation at various wavelengths. Ozone (O_3), water vapour (H_2O), and carbon dioxide (CO_2) are the primary components in the atmosphere that absorb solar energy. The sections of EMS that are transmitted into the atmosphere without significant interference from gas absorption and are valuable for distant sensing are known as "atmospheric windows." Figure 1 displays the proportion of atmospheric window transmittance at various wavelengths of the electromagnetic spectrum. The atmospheric transmission window spans from 0.4 to 2 μm and mostly consists of reflected radiation in the visible, near-infrared (NIR), and Shortwave Infrared (SWIR) wavelength bands. The TIR wave spectrum has three transmission intervals within its atmospheric window. The first interval is around 3 μm, the second interval is approximately 5 μm, and the third interval is a broader window ranging from 8 μm to 14 μm

(Lillesand et al., 2015). The window that extends beyond a wavelength of 1 mm is associated with the microwave area.

3.3.4 ATMOSPHERIC TRANSMISSION—EARTH'S SURFACE INTERACTION

To create detailed maps of LCLU characteristics, it is crucial to accurately understand the solar radiation that the Earth's surface reflects back and collect this data using remote sensing. Electromagnetic radiation that reaches the Earth's surface undergoes three sorts of interactions: absorption, transmission, and reflection. The characteristics of the target substance and the energy level of the wavelength both have an impact on these interactions. Specular reflection and diffuse reflection are two distinct forms of reflection that arise from this interdependence.

Specular reflection is the phenomenon when energy encounters a smooth surface and is mostly redirected away from the surface in a singular direction. Conversely, diffuse reflection happens when energy encounters a surface with irregularities, resulting in the reflection of almost all the energy in a uniform manner in all directions. According to Lillesand, Kiefer, and Chipman (2015) in their book *Remote Sensing and Interpretation*, spectral reflectance is the proportion of incoming energy that objects on the Earth's surface reflect or radiate at various wavelengths. In order to differentiate the characteristics of the spectrum response for various features, we may create a spectral response curve. Figure 2 (Penn State e-Education Institute, n.d.) demonstrates the variations in spectral response curves for plants, water, and bare soil across several wavelength bands in the visible spectrum.

Vegetation plays a fundamental role in the development of ecological processes. It is one of the most targeted land cover classes for Remote Sensing study due to its distinct spectral characteristics. Furthermore, understanding the interaction of vegetation with electromagnetic radiation helps in assessing forest health, monitoring growth patterns, mapping land cover, monitoring forest utilisation, etc. The spectral response of vegetation in a specific spectral band is determined by leaf characteristics such as pigment content, thickness, cell structure, and water content during the growth cycle. The reflectance curve demonstrates that vegetation absorbs energy in the blue and red channels as a result of chlorophyll, while reflecting a comparatively higher amount in the green channel. The NIR band has the most reflectance, while the SWIR (mid- and far-IR) band has less reflectance

and changes depending on how much free water is in the leaf tissue (Bakker et al., 2001). The spectral reflectance of plant cover fluctuates throughout the year at various visible wavelengths.

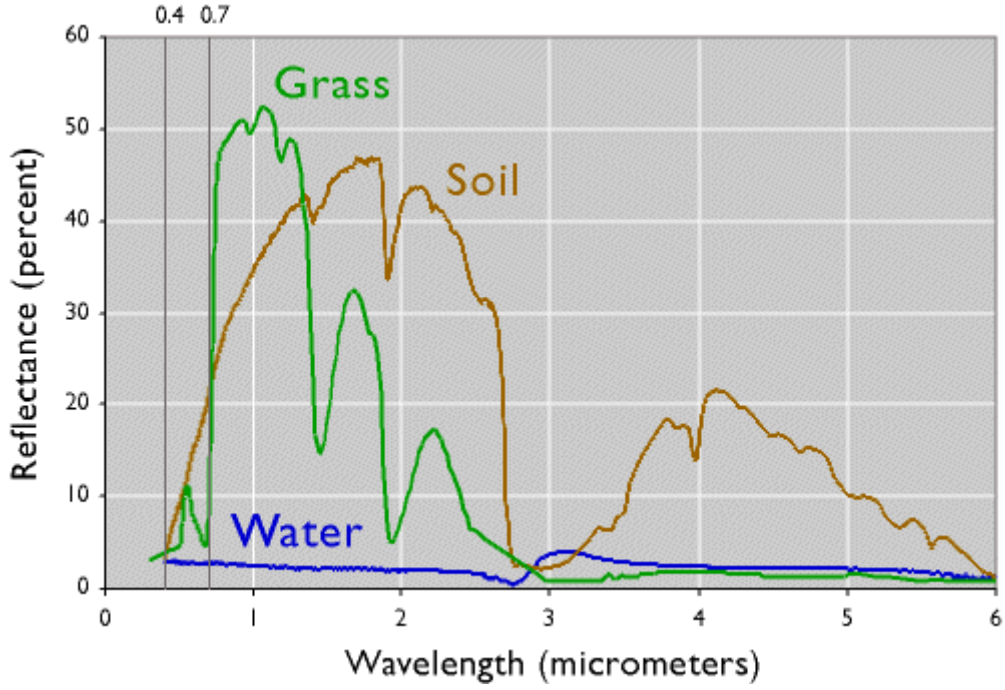

Figure 2. Spectral reflectance of water, soil, and vegetation in the VIS and NIR regions. From "Spectral Response Patterns" (The Nature of Geographic Information, Penn State e-Education Institute, n.d., https://www.e-education.psu.edu/natureofgeoinfo/node/1906).

Soil. The reflectance curve of bear earth rises steadily from visible to IR wavelengths. Hence, the establishment of a soil reflectance curve is challenging due to several elements that affect reflectance, such as moisture content, soil colour, canonates, and iron oxide (Bakker et al., 2001).

Water. Water bodies have a spectral response curve that is significantly different from that of plant and bare soil types. According to Bakker et al. (2001), water has a poor spectral reflectance in the visible wavelength range and essentially no reflection in the NIR wavelength area.

3.4 Optical remote sensing in Earth Observation: a brief history

The impetus for remote sensing emerged with the commencement of rocket launches, particularly during the period from 1946 to 1950. Cameras of reduced size were affixed to confiscated V-2 rockets at the White Sands test site in New Mexico (Lillesand, Kiefer, &

Chipman, 2004). The use of satellites for remote sensing began with the launch of the TIROS-1 (Television and Infrared Observation Satellite) in 1960. The spacecraft, which was equipped with IR rays, was the pioneering weather satellite and was developed with the aim of remotely observing the Earth's surface (Lillesand, Kiefer, & Chipman, 2004). As a component of the ERTS project, NASA launched the ERTS-1 satellite in 1972. The satellite, subsequently dubbed Landsat 1, was purposefully designed to gather uninterrupted data pertaining to the land surfaces of Earth. The system used a multispectral scanner installed aboard the spacecraft, which offered a moderate level of spatial resolution (U.S. Geological Survey [USGS], n.d.). The decision to initiate the deployment of this satellite was predicated upon the examination of imagery obtained from meteorological satellites and other spacecraft.

The successive Landsat missions, such as Landsat 8 and 9, have consistently supplied multispectral images that have played a significant role in monitoring changes in land cover and conducting environmental assessments (USGS Landsat Programme). The French SPOT (Satellite Pour l'Observation de la Terre) project started its mission in 1986 with the launch of SPOT 1 (Centre National d'Études Spatiales [CNES], n.d.). This initiative aims to provide high-resolution optical imaging for many applications, such as agriculture, forestry, and urban planning (CNES). The consecutive missions, spanning from SPOT 2 to 7, have been crucial in enhancing the calibre of the optical data that is now available (CNES, n.d.). The sensors of the Moderate Resolution Imaging Spectroradiometer (MODIS) are installed on NASA's Terra and Aqua spacecraft, which were launched in 1999 and 2002, respectively. The devices are essential for conducting climate research, analysing land cover, and investigating the atmosphere (NASA Earth Observing System Data and Information System [EOSDIS], n.d.). The use of MODIS data has significantly improved the efficacy of optical remote sensing (NASA EOSDIS, n.d.). The corporate sector has made notable progress in the domain of optical remote sensing. Introduced in 2001 by DigitalGlobe, QuickBird revolutionised the collection of data for urban planning and disaster management by providing high-resolution optical images (DigitalGlobe, n.d.). The WorldView series, including WorldView-1, WorldView-2, WorldView-3, and WorldView-4 enhanced the capabilities of high-resolution optical remote sensing (European Space Agency [ESA], n.d.).

Compact satellites have emerged as significant contributors in the field of optical remote sensing. Planet has successfully deployed several miniature satellites outfitted with optical

sensors, using the PlanetScope constellation (Planet Labs, n.d.). These satellites provide daily global coverage with high-resolution images, revolutionising the use of technology in agriculture, forestry, and environmental monitoring. The Sentinel series, namely Sentinel-2A and 2B, are crucial components of the Copernicus project (European Space Agency [ESA], n.d.). The ESA Sentinel 2 provides multispectral photography for the purposes of environmental monitoring, disaster management, and land use planning.

China has significantly bolstered its optical remote sensing capabilities via efforts like Yaogan and Gaofen (China National Space Administration [CNSA], n.d.). The Yaogan series, launched in 2006, comprises satellites specifically engineered for optical reconnaissance purposes. The China National Space Administration (CNSA, n.d.) asserts that the Gaofen series, which has been operational since 2013, provides high-resolution optical and radar data, especially intended for land and resource management objectives.

The advancement of optical remote sensing has greatly enhanced our ability to monitor and analyse the Earth's surface. These missions have together improved our ability to collect vital data for environmental assessment, scientific research, and other applications, ensuring continuous progress in optical remote sensing technology for Earth observation.

3.4.1 SENSORS AND ORBIT PLATFORMS

In order to transmit information to ground stations, sensors on board satellites or aeroplanes detect, quantify, and document the amount of reflected electromagnetic (EM) radiation in either analogue or digital format (Bakker et al., 2001). Active sensors emit self-generated light and direct it towards the target, as opposed to passive sensors that rely on solar radiation for lighting. To categorise these sensors, we examine the specific spectral region in which they operate. Visible-light passive sensors include a range of devices such as multispectral scanners, image spectrometers, satellite line cameras, aerial cameras, and video cameras. On the other hand, microwave passive sensors specifically refer to passive microwave radiometers. Laser scanners are a kind of active sensor that function within the visible spectrum, whereas imaging radars and radar altimeters work within the microwave range (Bakker et al., 2001).

These earth observation sensors may be deployed on many platforms, ranging from terrestrial to extraterrestrial, including spacecraft (Bakker et al., 2001). The sensors can

gather more accurate data from the surroundings when the platform is positioned closer to the ground, and conversely.

Satellite-based remote sensing is an ongoing process that takes data from the Earth's surface to assist in environmental monitoring at local, regional, and global levels. Weather satellites and communications satellites use geostationary or geosynchronous orbits due to their constant observation of a specific area. These orbits are positioned around 36,000 km above the Earth's surface and move in time with the Earth's rotation. Satellites in polar orbits, characterised by inclinations ranging from 80 to 100 degrees, provide global observation capabilities and typically orbit at altitudes between 600 km and 1,000 km above the Earth. Sun-synchronous orbits, seen in satellites such as Landsat and SPOT, are ideal for consistent and synchronised observations due to their ability to maintain a steady local solar clock for each studied area (Bakker et al., 2001).

3.4.2 IMAGE RESOLUTIONS

Based on the sensor characteristics used for remote sensing data acquisition, four distinct image resolutions are identified: spatial, spectral, radiometric, and temporal resolutions (Thenkabail, 2016). The term "spatial resolution" pertains to the size of the ground unit (measured in centimetres, metres, or kilometres) that is shown by a single pixel in an image. The instantaneous field of view (IFOV) and height at which the sensor is positioned determine this size (Canada Centre for Remote Sensing [CCRS], 2019). Satellite images may be classified into five types based on their spatial resolution: extremely high resolution (0.5–4.9 m), high resolution (5.0–9.9 m), medium/moderate resolution (10.0-39.9m), moderate resolution (40.0–249.9 m), and coarse/low resolution (250 m–1.5 km) (Thenkabail, 2016).

Spectral resolution refers to a sensor’s ability to distinguish and classify narrow wavelength intervals within the electromagnetic spectrum (CCRS, 2019). Figure 3 shows how the spectral resolution changed over the course of the Landsat satellite series (1–9). Landsat 8 OLI/TIRS and Landsat 9 OLI-2/TIRS-2 contain eleven spectral bands each, but Landsat 7 ETM+ only has eight (National Aeronautics and Space Administration [NASA], n.d.).

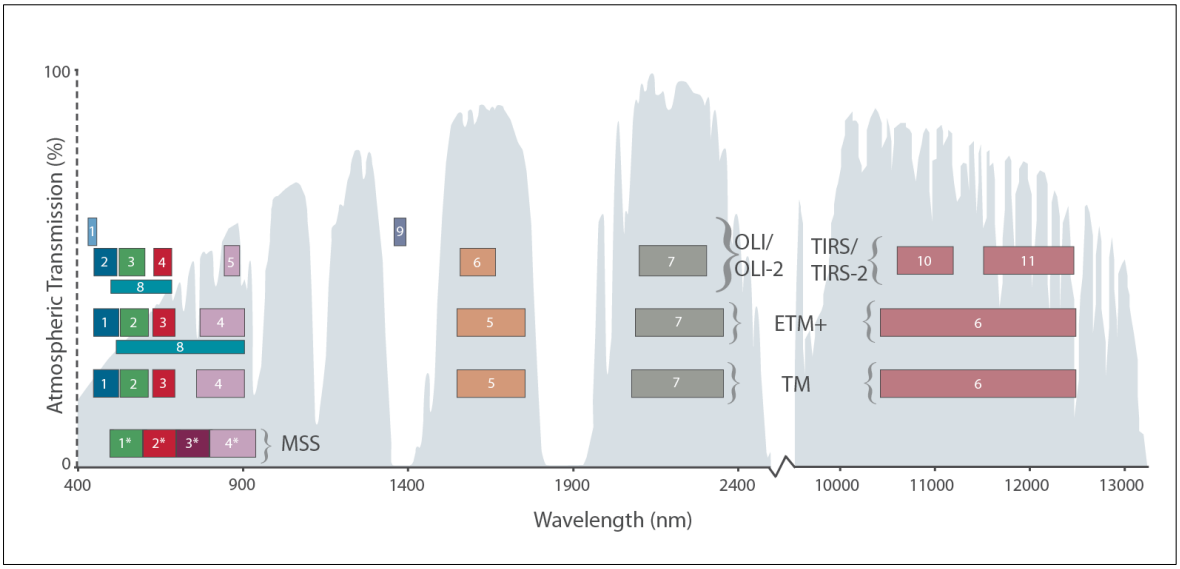

Figure 3. Spectral band evolution of Landsat satellites (Landsat 1 to Landsat 9). From NASA Landsat (n.d.), https://landsat.gsfc.nasa.gov/satellites/landsat-9/landsat-9-bands/

The radiometric resolution refers to the sensor's capacity to detect and distinguish the intensity and range of reflected radiation from the Earth's surface. This information is then converted into a digital number (DN), which is a binary format used to represent numbers in bits (CCRS, 2019).

The radiometric resolution of Landsat satellites has also undergone changes. The Landsat 9 sensor captured data using a 16-bit exponent, allowing it to distinguish up to 16,384 shades of grey per wavelength. In comparison, Landsat 8 (12-bit) and Landsat 7 (8-bit) have lesser radiometric resolution. Temporal resolution pertains to the duration required for a satellite to complete a single orbit around the Earth in relation to the time needed to monitor the same region (CCRS, 2019). For instance, in the case of Landsat 8, the time required to return to a certain region is 16 days.

Remote sensing has made it easier to observe the Earth's surface, allowing for the monitoring of changes in land and land use over a wide range of locations and time periods. This includes activities such as deforestation and urban expansion.

3.4.3 LANDSAT SATELLITE SERIES CHARACTERISTICS

Since its inception in 1972, the Landsat satellite series has consistently played a significant role in the area of Earth observation, offering a valuable collection of essential image data.

The use of this extensive dataset has significantly enhanced scholars' comprehension of changes in LCLU across time.

The National Aeronautics and Space Administration (NASA) and the United States Geological Survey (USGS) worked together on the Landsat project (U.S. Geological Survey [USGS], 2022). The project has effectively deployed a total of eight satellites throughout the years, with the next addition being Landsat 9, which was launched in 2021.

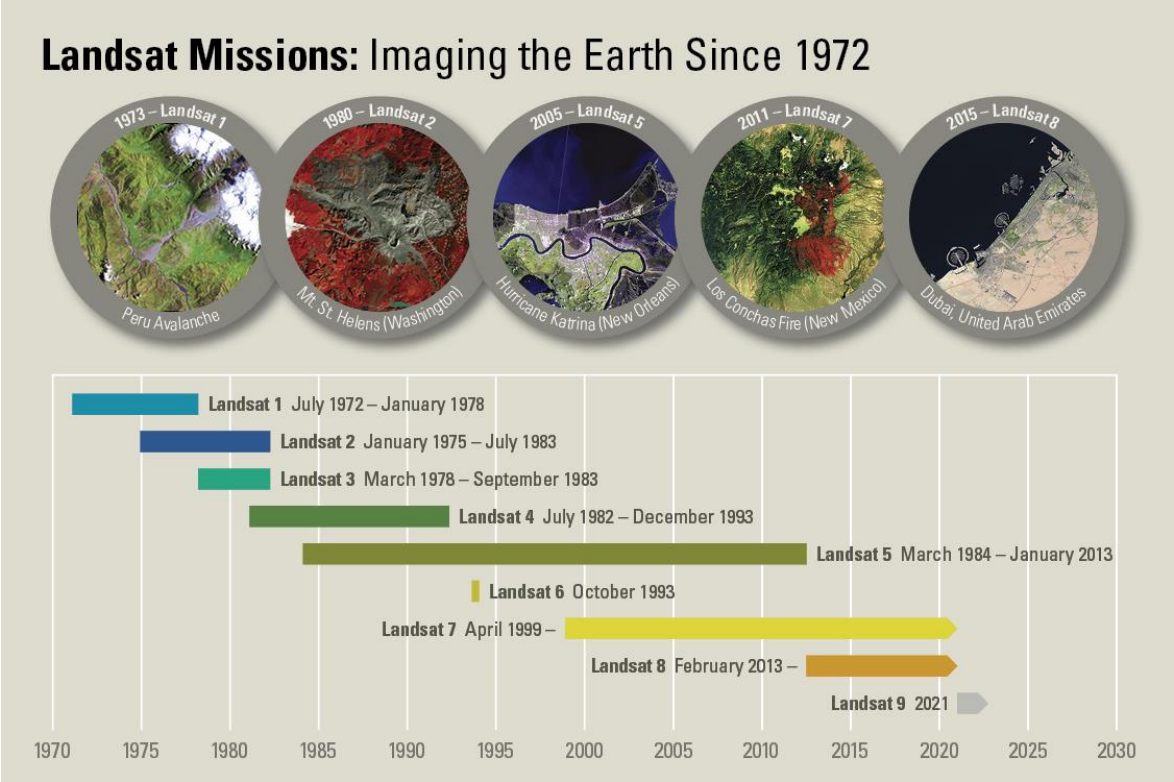

Figure 4. The Landsat mission timeline from 1972 to today. From USGS (2022), Landsat—Earth observation satellites. https://www.usgs.gov/landsat

The Earth Resources Technology Satellite (ERTS-1) was the first satellite launched in 1972, subsequently renamed Landsat 1. The Landsat series progressed with the deployment of Landsat 2 in 1975, Landsat 3 in 1978, Landsat 4 in 1982, and Landsat 5 in 1984. Unfortunately, the failure of Landsat 6 to reach its intended orbit in 1993 attracted more attention than the launch itself. With the deployment of Landsat 7 in 1999 and the launch of Landsat 8 in 2013, the series of satellite launches resumed. In 2021, Landsat 9 was added to the group of spacecraft dedicated to Earth surface surveillance, along with the other three satellites.

The progress made in the development of Landsat sensors has been remarkable. The sensors were originally equipped with four broad spectral bands, but they have since evolved to include narrower, more abundant, and strategically placed wavelength ranges (Wuder, 2019). Landsat 1, 2, and 3 were equipped with two sensors: the Multispectral Scanner (MSS) and the Return Beam Vidicon (RBV) camera (Table 2). The MSS obtained images in four spectral bands (green, red, and NIR) with a spatial resolution of 80 metres (resampled at 60 metres). On the other hand, the RBV sensor captured data on black and white film with a maximum size of 70 millimetres (USGS, 2022).

Landsat 4 and Landsat 5 included the Thematic Mapper (TM) sensors, which represented a significant advancement over the previous Multispectral Scanner (MSS) technology. The TM sensor included SWIR bands, added a 120-metre TIRs band, and enhanced the spatial resolution to 30 metres for visible, NIR, and SWIR bands.

Landsat 7 improved upon its predecessor by introducing the Enhanced Thematic Mapper Plus (ETM+), which had a 60-metre TIR band and an additional 15-metre panchromatic band, among other enhancements. Landsat 8 and Landsat 9 are equipped with the Operational Land Imager (OLI) and the TIRs. The OLI sensors include two additional spectral bands compared to Landsat 7 ETM+: Coastal/Aerosol (band 1) for observing coastal/aerosol phenomena and Cirrus (band 9) for identifying cirrus clouds (NASA Science, 2023).

Landsat 8 and Landsat 9 orbit the Earth in a synchronised path with the sun at a height of 705 kilometres, covering a breadth of 185 kilometres. The satellites possess a temporal resolution of 16 days, but their orbits are deliberately shifted to provide an 8-day repetition cycle over the same Landsat scene region on the Earth's surface. Landsats 4, 5, and 7 have the same orbit parameters as Landsats 8 and 9, whereas Landsats 1, 2, and 3 operated at an altitude of 920 km.

Band	L8–9 OLI/TIRS		L7 ETM+		L4–5 TM		L4–5 MSS		L1–3 MSS	
	BN	WL	BN	WL	BN	WL	BN	WL	BN	WL
Coastal/Aerosol	1	0.43–0.45	----	------	--	--	---	---	---	---
Blue	2	0.45–0.51	1	0.45–0.52	1	0.45–0.52	---	---	---	---
Green	3	0.53–0.59	2	0.52–0.60	2	0.52–0.60	1	0.5–0.6	4	0.5–0.6
Panchromatic	8	0.50–0.68	8	0.52–0.90	---	---	---	---	--	----

Red	4	0.64–0.67	3	0.63–0.69	3	0.63–0.69	2	0.6–0.7	5	0.6–0.7
NIR	5	0.85–0.88	4	0.77–0.90	4	0.77–0.90	3	0.7–0.8	6	0.7–0.8
NIR	--	----	--	----	---	---	4	0.8–1.1	7	0.8–1.1
Cirrus	9	1.36–1.38	--	----	---	---	---	----	---	---
SWIR-1	6	1.57–1.65	5	1.55–1.75	5	1.55–1.75	---	----	---	----
SWIR -2	7	2.11–2.29	7	2.09–2.35	7	2.08–2.35	---	----	----	-----
Thermal	10 - T1	10.60–11.19	6- T2	10.40–12.50	6- T2	10.40–12.50	---	----	----	----
Thermal	11 - T1	11.50–12.51	----	-----	---	---	---	----	---	-----

Table 2. Characteristics of Landsat satellites. Adapted from U.S. Geological Survey (2015), Landsat—overview and satellite characteristics (https://doi.org/10.3133/fs20153081)

The USGS offers unrestricted access to Landsat data, following a policy of openness and free availability since 2008. As part of this, USGS (2022) states that it will provide users worldwide with carefully processed, high-quality data. This includes systematic, geometric, radiometric, and terrain-corrected aspects at different reprocessing levels. The Landsat Collection 2 scene-based products demonstrate the use of cutting-edge data processing methodologies, algorithm development, and improved access and sharing of data (USGS, Landsat Collection 2, 2021). The extensive data collection and extensive archive of Landsat, along with its open and free data policy, allow users to access time series data for huge geographical regions and track changes in LCLU over time (USGS, 2022). The Landsat mission is anticipated to undergo further advancements before the end of 2030 (U.S. Geological Survey [USGS], 2023. The new Landsat Next satellite, consisting of three observatories housed in a single spacecraft, is set to be sent into orbit by NASA and the USGS. This advanced satellite will provide enhanced capabilities to cater to the needs of the next generation of Landsat users.

3.5 IMAGE CLASSIFICATION APPROCHES

Image classification is the task of categorising pixels in a digital image into distinct classifications of land cover or land use, depending on their spectral features (CCRS, 2019). The approach described is often referred to as spectral pattern identification. It involves grouping pixels with comparable spectral responses to a certain surface feature in order to represent a specific land cover or use class (Lillesand, Kiefer, & Chipman, 2015). A pattern

is a multidimensional vector of characteristics derived from the spectral response values of an image. It is computed by performing computations on groups of features and may be visualised as axes in an n-dimensional space (Tso & Mather, 2009). The left graph in Figure 5 illustrates the visualisation of a two-band image as a two-dimensional feature space, while the right graph depicts the visualisation of a three-band image in a three-dimensional feature space (ITC, n.d.).

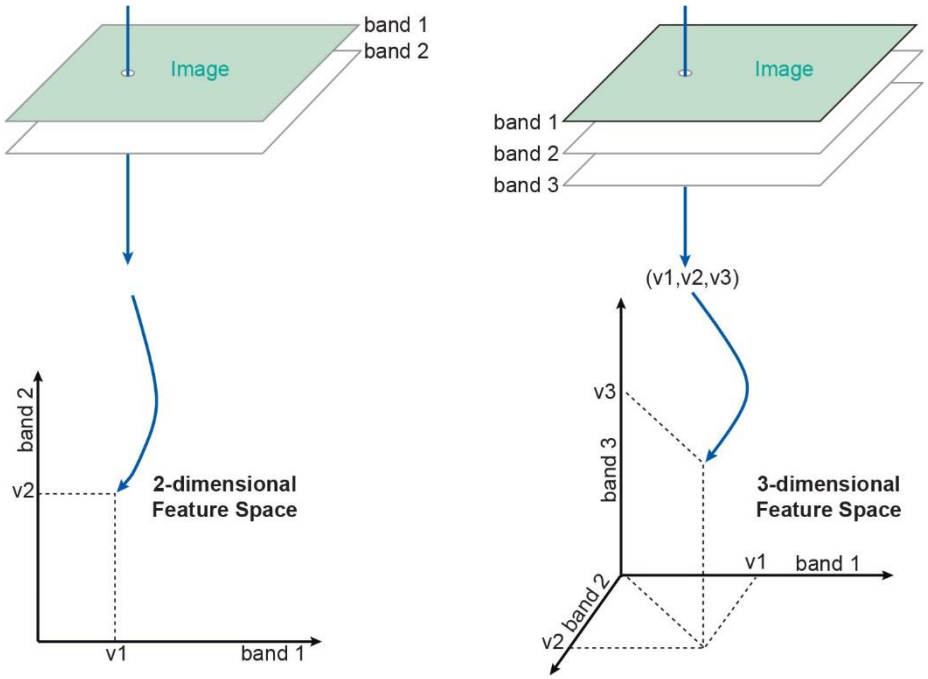

Figure 5. Feature vectors plotted in two- and three-dimensional feature space From ITC (n.d.), https://ltb.itc.utwente.nl/page/498/concept/81578

Simultaneously, different feature objects in a satelite image, such as crops, identified in a single or group of pixels, can be plotted in n-dimensional feature space to analyse their differences on spectral properties during the classification process.

Two common methods used in the image classification process are supervised classification and unsupervised classification. The supervised classification technique involves the use of training samples to train the algorithm to recognise different classes in feature space (Tso & Mather, 2009). An expert manually selects the training samples, which represent various land cover classes such as forest, water, urban area, etc.

On the other hand, in an unsupervised classification technique, the clustering algorithm identifies groups of pixels that have similar spectral properties and assigns each group to a different class (CCRS, 2019). The analyst determines the number of classes. The purpose of

image classification is to extract information about specific characteristics of the land cover, such as forest or urban cover, or to create a categorical thematic map, such as a land cover and use map.

The process of digital classification of images is mainly carried out through these steps: selection and preparation of satellite images; definition of culusters in the feature space; selection of the classification method (supervised or unsupervised); selection of the classification algorithm and its execution; and verification of the results (Bakker et al., 2001).

3.5.1 SUPERVISED CLASSIFICATION

The first responsibilities of an analyst are choosing and preparing images for digital calcification, which is contingent upon the intended use of the data. The most prevalent images used for image classification are multi-spectral and multi-temporal images. The identification and collection of holding areas that reflect the various land cover or use categories is a crucial step in the supervised image classification approach, after the selection of images. The analyst selects the samples based on their familiarity with the many geographic entities included in the visual scenario. The characteristics and dimensions of the training regions have a significant impact on and determine the division of the feature space during algorithm training (Tso & Mather, 2009). A general guideline for determining the number of samples required per labelled class is to gather around 30 samples for each spectral band used in the classification process (Bakker et al., 2001). After the analyst has specified the tracking zones, the image categorization may be performed by using the classifier (algorithm). The MD and ML methods are the most often used techniques in supervised categorization of images (Bakker et al., 2001).

3.5.1.1 Minimum Distance algorithm

The MD approach computes the Euclidean distance between the spectral characteristics of each pixel in a image and the centroid of each feature class (Bakker et al., 2001). The pixel is allocated to the class with the smallest distance. The MD classifier exhibits computational efficiency, yet it is subject to certain constraints. Specifically, it may assign pixels to a class even if they are located farthest from the class centre. Additionally, it does not account for the spectral variability present in the data (Lillesand, Kiefer, & Chipman, 2015).

Figure 6, illustrates the operational principle of the MD method in a scenario where a two-dimensional feature space is divided into partitions. The sketch in the upper right corner depicts the scenario where the separation threshold for the dividing borders of the classes is not specified, while the sketch in the bottom right corner illustrates the scenario when the threshold is defined to determine the dividing boundaries of the classes.

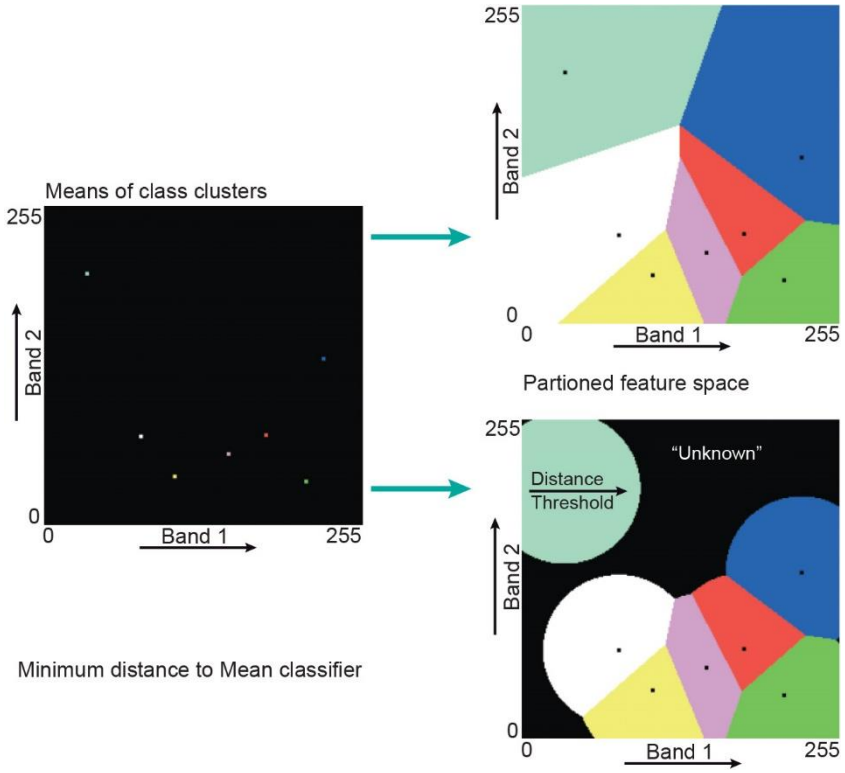

Figure 6. Illustration of the MD method in feature space, with and without threshold parameters. From ITC (n.d.), https://ltb.itc.utwente.nl/page/498/concept/81518

3.5.1.2 Maximum Likelihood algorithms

The ML classifier operates under the assumption that the spectral values of each class conform to a multivariate normal distribution. It then proceeds to estimate the distribution's parameters for each class using a training dataset. The training dataset comprises a set of pixels that have been labelled by an expert to represent their respective classifications. The training data is used to produce the mean vector, which represents the centre of each class in the feature space, and the covariance matrix, which describes the distribution of the data around the mean. During the classification phase, the Machine Learning classifier computes the probability of a pixel belonging to each class by using the estimated mean vector and covariance matrix. The probability is a metric that quantifies the degree to which the spectral values of the pixel conform to the normal distribution of each class. The pixel is allocated to

the class with the greatest probability. Figure 7 depicts the functional elements of the ML classifier for dividing the feature space and determining partition boundaries. The upper right portion shows how this is done without using threshold parameters, while the bottom right portion demonstrates the process with the use of threshold parameters.

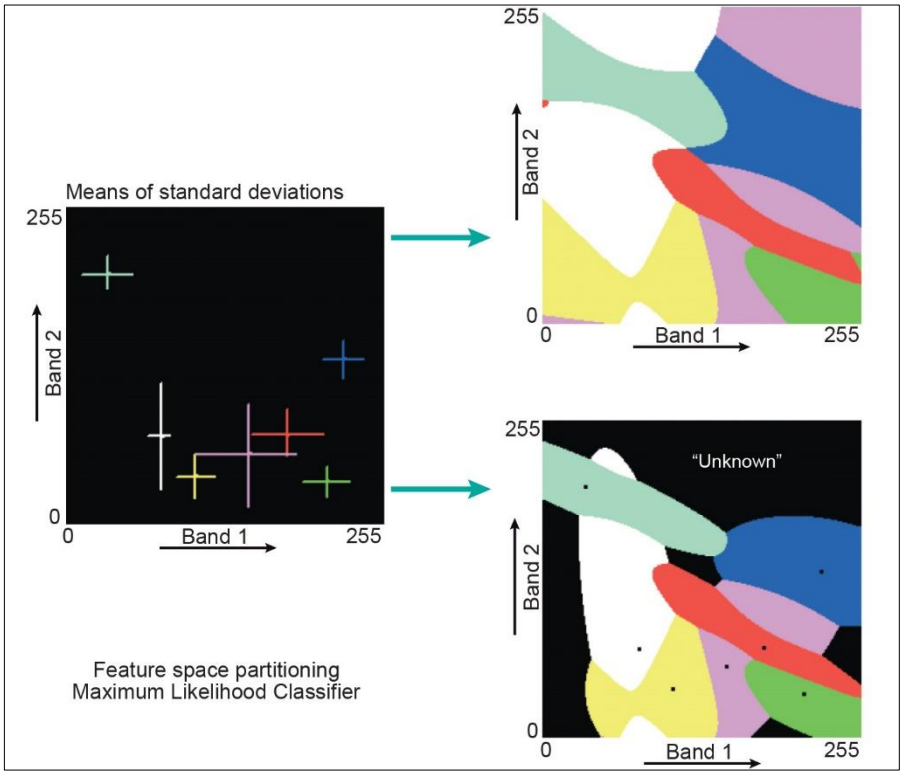

Figure 7. Illustration of the ML method in feature space, with and without threshold parameters. From ITC (n.d.), https://ltb.itc.utwente.nl/page/498/concept/81518

3.5.1.3 Support vector machine (SVMs) algorithms

Introduced first by Vapnik and his colleagues in the late 1970s, the Support Vector Machine (SVM) method is among the most frequently used kernel-based learning algorithms in many different machine learning applications, including image classification (Mountrakis et al., 2011). The Support SVM is an effective classifier capable of handling both linear and nonlinearly separated data (Sheykhmousa et al., 2020). Figure 8 illustrates a graphic example of the implementation of SVM with linearly separable data. Originally linear binary classifiers, SVMs build a separation hyperplane (decision boundary) using the characteristics of the training samples—more specifically, their distribution in feature space (Tso & Mather, 2009). In a data space, the decision boundary is a line or surface separating several areas, each linked with a class label. The decision boundary in the SVM algorithm may be a line or plane separating the data space into two regions, one connected with the

class label +1 and the other with the class label -1 (Vapnik, 1982). The SVM technique discovers the ideal decision boundary to maximise the margin between the two regions.

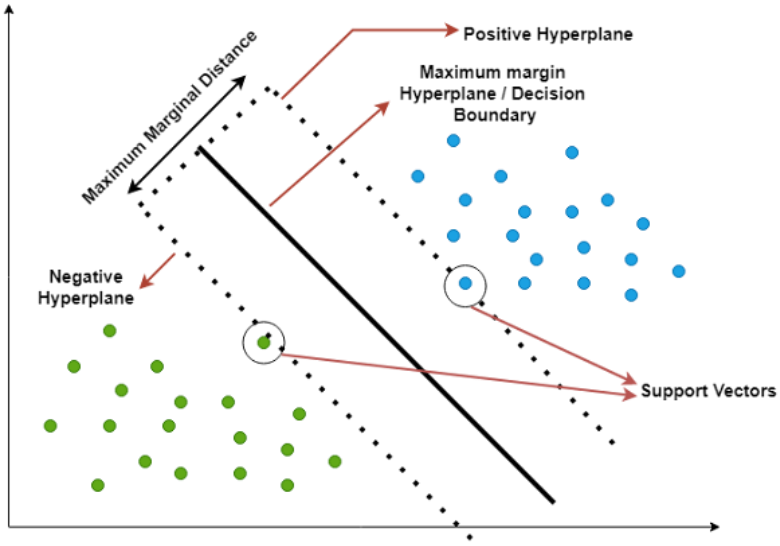

Figure 8. Schematic representation of the SVM method. From PyCodeMates (2022), https://www.pycodemates.com/2022/07/support-vector-machines-detailed-overview.html

In an SVM algorithm, the data points closest to the dividing line separating the two classes constitute the support vectors. The best decision boundary for a classifier is found by using nonlinear kernels and by extending SVMs to multiclass classifiers through the integration of multiple binary classifiers (Cortes & Vapnik, 1995). Common kernels for nonlinear data include polynomial, radial basis function, Gaussian radial basis function, and sigmoid function (Hsu et al., 2010). Amongst them, radial basis function (RBF) and polynomial kernels are often utilised for remotely sensed image processing (Mountrakis et al., 2011).

RBF kernel support SVMs classify remotely sensed data effectively. Their capacity to handle high-dimensional feature spaces and capture complex decision boundaries makes them ideal for satellite image classification, hyperspectral image analysis, and land cover mapping (Cristianini & Shawe-Taylor, 2000). Research such as Pal and Mather (2005) has shown that SVM-RBF can increase remote sensing classification accuracy and computational efficiency (Hsu et al., 2010).

Remote sensing supports urban planning, environmental monitoring, and resource management by classifying LCLU. Studies have demonstrated that SVM-RBF categorise multispectral satellite images more accurately than traditional methods such as ML and MD (Zhang et al., 2023; Pal & Mather, 2005).

3.5.1.4 Neural Network algorithms

ANN are Machine Learning algorithms that resemble the neurones of the human brain, where, through layers of neurones, they process input data into useful results. Artificial ANN were therefore developed and have been progressively applied in remote sensing for imagine classification (Rodríguez-Galiano et al., 2012; Giacinto & Roli, 2001). ANNs are nonparametric models that rely on the quality of training samples to derive rules for classifying unknown data. Their implementation requires the specification of parameters such as the learning rate, among others (Tso & Mather, 2009). There exist many types of ANN that have been developed over time such as: Feedforward Neural Networks, Convolutional Neural Networks (CNN), Recurrent Neural Networks (RNN), Long Short-Term Memory Networks (LSTM), Gated Recurrent Units (GRU), Radial Basis Function Networks (RBFN), Self-Organizing Maps (SOM), Deep Belief Networks (DBN), etc., that find use in machine learning (GeeksforGeeks, n.d.).

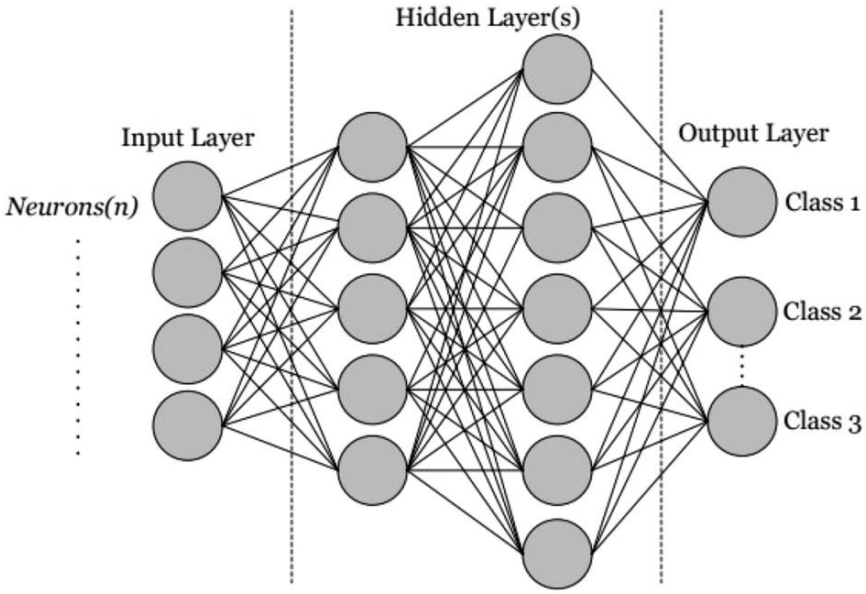

Figure 9. Neural network scheme. From Khan and Minallah (2023), Remote sensing based forest cover classification using machine learning, Scientific Reports, 13, Article 50863. https://doi.org/10.1038/s41598-023-50863-1

The development of the backpropagation algorithm enabled multilayer perceptrons (MLPs) to learn complex patterns, thus driving renewed interest in neural networks in the 1980s.

The MLP, one of the most commonly used ANN models, applies the backpropagation learning method (Rumelhart et al., 1986). As a type of feedforward neural network (FNN), the MLP uses interconnected neurons across three layers—input, hidden, and output—for

information processing and transmission. The input layer receives data, the hidden layer computes weighted sums, and the output layer produces classification results.

Several studies (Xia et al., 2017; Mochizuki & Murakami, 2012) have shown that the use of MLPs in LCLU classification is common. Comparative research (Benediktsson & Sveinsson, 1997; Bischof et al., 1992; Kulkarni & Patil, 2011) suggests that ANN classifiers often perform more accurately than traditional classifiers such as ML and MD.

3.6 ACCURACY ASSESSMENT OF IMAGE CLASSIFICATION

Evaluating thematic correctness is a crucial stage in remote sensing and GIS analysis to verify the reliability and validity of the classification outcome. Congalton and Green (2009) provide a comprehensive overview of the theoretical and practical ideas involved in designing and implementing a quantitative accuracy evaluation for a classification result. The evaluation of classification accuracy may be accomplished by analysing the confusion matrix, which is a report that combines the classification output and reference data. The confusion matrix is also known as the error matrix or contingency table. The error matrix is a symmetrical arrangement of numerical values, structured in rows and columns. Each row corresponds to the classification output, while each column corresponds to the reference data, which is believed to be accurate (Congalton & Green, 2009). The error matrix table provides a clear representation of the specific faults in each class category, including inclusion-commission errors and exclusion-omission errors (Congalton, 2001). The error matrix table provides the necessary information to determine several accuracy measures, such as OA, User's Accuracy (UA), producer's accuracy, and the kappa coefficient. These metrics provide a rough approximation of the accuracy of the classification and aid in identifying the strengths and shortcomings of the classification outcome.

To develop an accurate classification evaluation, it is crucial to examine the sampling strategy, sample size and unit, reference data collection, and geographic autocorrelation (Congalton, 1991). When it comes to the sample design, random sampling and stratified random sampling are highly recommended methodologies for LCLU categorization output (Bakker et al., 2001). During a classification procedure, the sample unit might be used as individual pixels, clusters of pixels, or polygons. For map classes with fewer than 12 categories or an area smaller than 1 million acres (4046.86 km^2), it is recommended to collect at least 50 samples for each class. Conversely, for maps with more than 12 categories or an

area larger than 4046.86 km^2, it is necessary to gather 75 to 100 samples per class category (Congalton, 1991). Field surveys, the interpretation of high-resolution images, or the use of pre-existing maps are all possible ways to acquire the training samples for classification and the reference data samples.

3.7 CHANGE DETECTION CLASSIFICATIONS

The fundamental aspect of digital change detection is analysing temporal events using images from different dates, usually obtained using multi-spectral satellite-based sensors (Coppin et al., 2004). Change detection refers to the process of recognising variations in the condition of an item or phenomenon at distinct points in time (Singh, 1989). This technique is highly valuable in various domains, such as analysing changes in land cover and use, monitoring shifting cultivation, assessing deforestation, studying changes in vegetation phenology, observing variations in seasonal pasture production, evaluating damage from different sources, detecting crop stress, monitoring disasters, measuring snowmelt, analysing thermal characteristics in day-night cycles, and conducting other environmental observations (Singh, 1989).

Several change detection approaches have been created in recent years, and there have been comprehensive descriptions and evaluations of these methods published Singh (1989), Deer (1995), Coppin and Bauer (1996), Jensen et al. (1997), Yuan et al. (1998), Serpico and Bruzzone (1999), Lu et al. (2004), and Richards et al. (2005).

In general, these strategies may be categorised into pre-classification and post-classification groups (Yuan et al., 1998). Pre-classification approaches use algorithms such as image differencing, image rationing, vegetation indices differencing, or principal components analysis (PCA). These methods are used on multi-date satellite data to detect regions that have seen "change" and those that have not, necessitating meticulous selection of threshold values within the histogram of change-related data. On the other hand, post-classification comparison involves using separate classifications of spectral images taken at various periods to generate different maps, which provide detailed change information on a pixel-by-pixel basis (Jensen, 2004). This technique provides significant advantages by effectively distinguishing data collected at two different dates. This reduces the need for normalisation and resolves alignment difficulties caused by variations in climatic conditions and sensor characteristics (Singh, 1989; Coppin et al., 2004).

The quality of each categorization and error distribution determines the precision of these maps (Yuan et al., 2005). However, the process of classifying the data from each individual date assists in constructing a chronological sequence that can be regularly updated and used for a multitude of purposes (Yuan et al., 2005).

3.8 MODELING LAND COVER AND LAND USE CHANGES

LCLU change modelling is fundamental for understanding environmental dynamics, future change projection, and guidance of sustainable land management and policy decisions. Many models—inductive, deductive, pattern-based, dynamic, spatial, and regional models—help to explore LCLU dynamics by means of scenario-based investigations (Mas et al., 2013). With different strengths and constraints (Pontius & Malanson, 2005), this analysis focusses on four well-known modelling techniques: ANN, logistic regression (LR), multi-criteria evaluation (MCE), and weights of evidence (WoE).

Designed to handle vast amounts of data and grasp intricate, nonlinear relationships, ANN is a Machine Learning method (Mas et al., 2014). To prevent overfitting, one needs meticulous regularising and large computing resources. One need great computational power and careful regularising to prevent overfitting. Key factors influencing land conversion rates are all those related to land cover types, socioeconomic indicators, accessibility aspects, and environmental circumstances (Almeida et al., 2008). Recent reviews have highlighted the rapid growth of deep learning approaches for LCLU classification, particularly with hyperspectral and multispectral data, showing a steady increase in publications since 2015 and identifying key methodological advances and challenges (Vali et al., 2020). In addition, deep learning combined with object-based image analysis has proven effective for detecting LCLU changes, offering improved accuracy and scalability over traditional pixel-based methods (Liu, Yang, & Lunga, 2021).

LR is a statistical method suitable for binary classification tasks that approximates the likelihood of land use changes dependent on predictor variables (Hosmer et al., 2013; Eastman et al., 2013). Based on important factors such as land use history, ownership, slope, soil type, and population density, the LR implies linearity although it might not be relevant in every situation (Mertens & Lambin, 2000).

MCE aggregates numerous geographic factors (Malczewski, 2006) to evaluate land use change potential, sometimes using the Analytical Hierarchy Process (AHP) to assign weights to several variables (Store & Kangas, 2001). Key factors include transportation systems, land use rules, environmental limitations, and socioeconomic concerns define MCE. These elements affect accessibility, rates of land conversion, environmental limitations, and regional investment appeal (Malczewski, 2006; Chen et al., 2010).

According to Bonham-Carter (1994), the Bayesian statistical method known as the weights of evidence (WoE) is employed to forecast changes in land use by analysing historical data. It finds use in spatial analysis in LUCC research and for categorical data (Dutta et al., 2016). Historical land use patterns, geological characteristics, climatic conditions, and socioeconomic factors like GDP and employment rates are the key variables here. But WoE presupposes statistical independence and calls for large amounts of training data (Cheng & Agterberg, 1999). Often derived from the synergistic application of discipline theory and expertise, new technologies and approaches have expanded our capacity to track and investigate changes in land use and land cover (Verburg et al., 2009). Land scientists can assess current land resources, identify hot-spots of change and indicate ongoing land cover change processes thanks to improvements in remote sensing and land inventory techniques (Herold, 2005).

4. MATERIALS AND METHODS

This chapter begins with a description of the study area, the main physical-geographical, and socio-economic characteristics. Next, the chapter delves into the data, their origins, and the steps taken to prepare them for classification. The chapter delves into the collection and evaluation of samples, provides a detailed description of the classifiers, and assesses their accuracy. The last section outlines the detailed process of applying the model to predict future changes in LCLU classes.

4.1 STUDY AREA

The Prishtina region of Kosovo is situated in the northeastern and central parts of the country (Figure 10). The area spans from latitudes 42.44 to 43.14 °N and longitudes 20.76 to 21.55 °E. The elevation in the area varies between 270 and 2656 metres above sea level. The region is the largest in terms of area, with a total of 2,157 square kilometres. Additionally, it has the highest population density, housing 477,312 people as of the 2011 census. The Prishtina district consists of eight municipalities and 298 smaller villages. Prishtina serves as the primary hub for trade, politics, administration, education, and culture in the region and the nation. Additionally, it is the capital city. The hydrography of the area is characterised by the significant presence of the Sitnica, Llapi, and Drenica rivers. Additionally, the man-made lakes of Badovci and Batllava play a vital role in providing drinkable water to the majority of the local population.

Since the Kosovo war in 1999, several factors have led to the growth of urban areas in the region. These include migration from rural to urban areas for better education and job prospects, the establishment of permanent urban settlements, the expansion of villages near urban boundaries, and the development of inter-regional and national road networks. From 1981 to 2011, a total of 45,905 people moved to the towns of Prishtina and Fushë Kosova, representing 27.84% of all internal migration within the country's municipalities. The internal migration over this time amounted to a total of 196,429 individuals (Kastrati et al., 2014). The influx had a significant influence on the urban expansion and alteration of LCLU in the region.

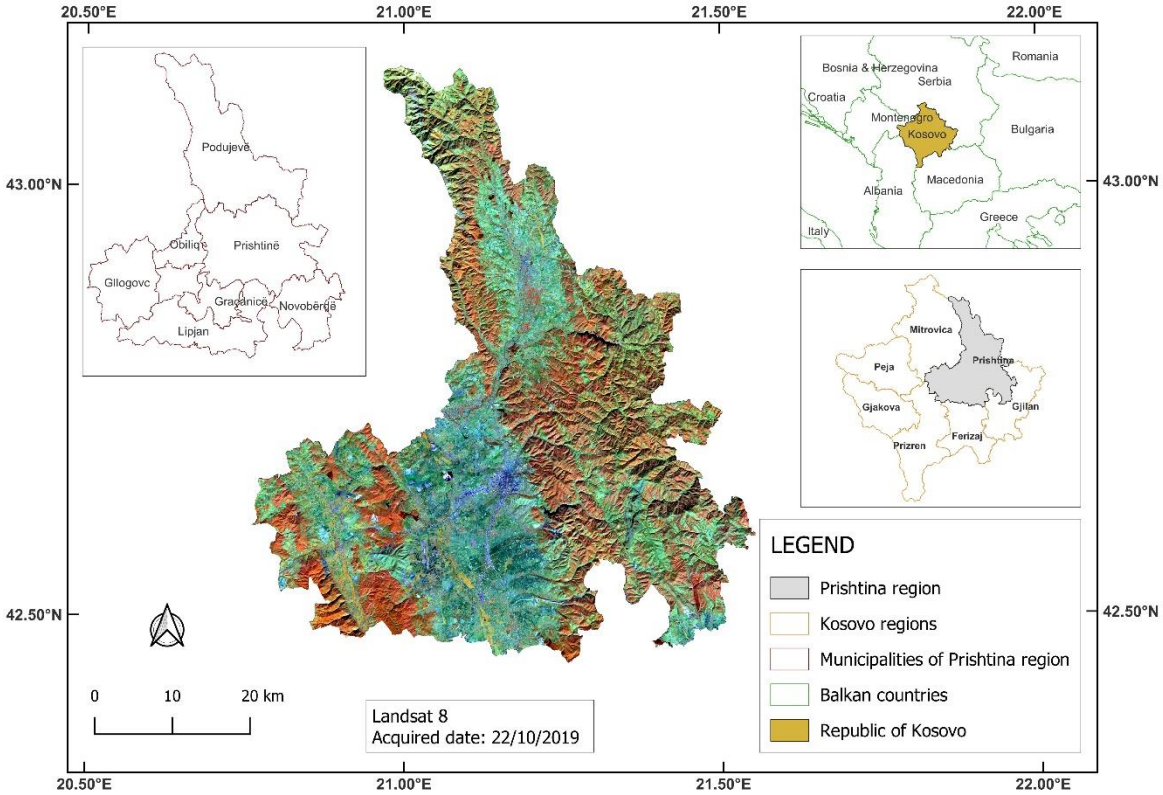

Figure 10. Geographical position of the Prishtina region, Kosovo.

According to the 2018 CLC inventory (Copernicus, 2023; see Figure 12), the region consists mostly of forests and semi-natural areas, which account for 1114.61 km^2, or 48.83% of the land. The region consists of 993.10 km^2, or 43.50%, of agricultural fields and 170.51 km^2, or 7.47%, of artificial surfaces.

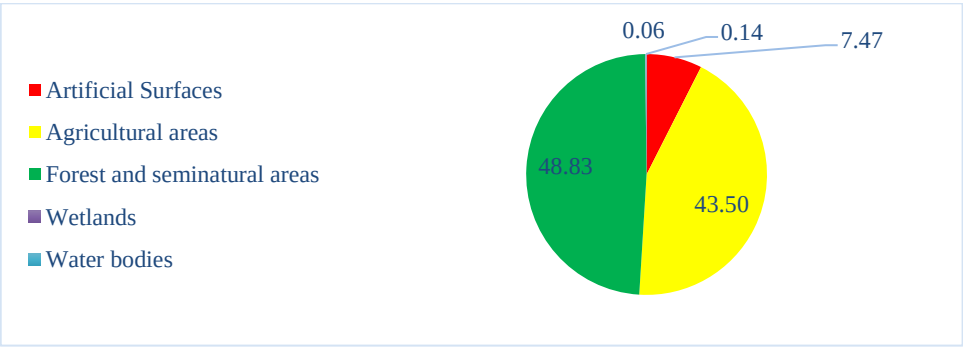

Figure 11. Distribution of LCLU classes in the study area (%).

The wetlands in the region include a relatively modest area of 1.42 km^2, which is equivalent to 0.06% of the total land area. Additionally, water bodies, such as lakes and rivers, occupy 3.15 km^2, accounting for 0.14% of the territory. Figure 11 further illustrates the proportional

distribution of LCLU classes in percentage terms, offering a complementary overview that highlights the relative extent of each class across the study region.

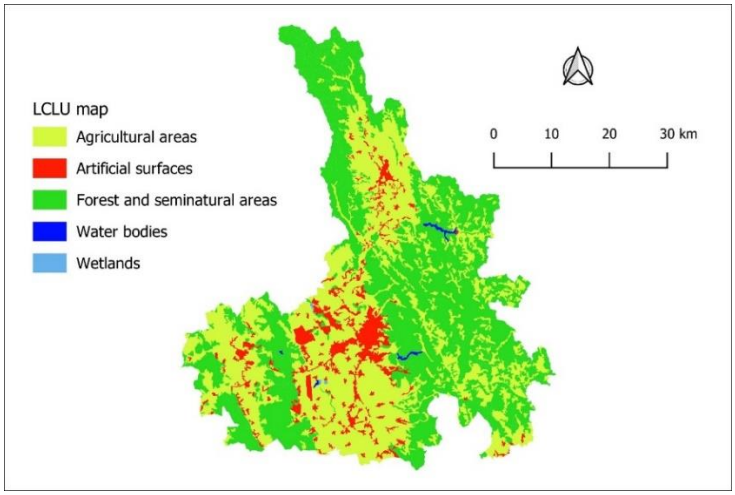

Figure 12. Land cover/land use (LCLU) classes of the study area based on the third-level CLC 2018 inventory.

4.2 DATA AND PROCESSING

The historical multispectral Landsat satellite images obtained from the TM, ETM+, and OLI/TIRS sensors were used as the primary data for this investigation. To classify the land cover for the years 2001, 2009, and 2019, multiple image scenes from Landsat were collected during a one-year timeframe. The multi-temporal, cloud-free images were acquired using the USGS Earth Explorer online platform (https://earthexplorer.usgs.gov/). Their purchase was free of charge. The data gathered by Landsat satellites undergoes a sequence of processing phases. Following these procedures, the data is stored in the Landsat archive with the designation "Collection." Landsat Collection 2 represents the second comprehensive reprocessing of the Landsat archive, incorporating recent advancements in data processing, algorithm development, and data access and dissemination. This has led to significant improvements in data products. Landsat Collection 2 was created by integrating current advancements in data processing, algorithm development, and data access and distribution (U.S. Geological Survey [USGS], n.d.). The Landsat 2 Collection has three distinct processing processes for the data. The data in Collection 2 Level 1 is sourced from satellites 1 to 9, while the data in Levels 2 and 3 are obtained from satellites 4 to 9, respectively.

This research focuses on image scenes obtained from the Landsat 4, 7, and 8 sensors, which are part of the Collection 2 Level-2 Science Products (L2SP). L2SP provides scientific

results in the form of scene-based measurements of global surface reflectance and surface temperature. Sayler and Zanter (2023) use the Land Surface Reflectance Code (LaSRC) algorithm, namely version 1.5.0, to process the data acquired by the Landsat 8 Operational OLI and produce surface reflectance products.

The Landsat Ecosystem Disturbance Adaptive Processing System (LEDAPS) algorithm (Version 3.4.0) is used to make surface reflectance data from Landsat 4-5 TM and Landsat 7 ETM+ (Sayler & Zanter, 2021). By using the metadata text (MTL) file that accompanies the Landsat 4, 7, and 8 scenes, we may explore other attributes of the L2SP downloaded products. The study's scenes have been geographically referenced using the Universal Transverse Mercator (UTM) projection with the World Geodetic System's (WGS) 1984 UTM datum, specifically in zone 34N, and with a spatial resolution of 30 m. The projection also includes the World Geodetic System (WGS) 1984 UTM datum. The whole investigation region was shown in the image of the scene acquired from the WRS-2 (Worldwide Reference System) path and row 185/30. The study uses Landsat scenes and assesses the proportion of scene cloud coverage and land cloud coverage. The MTL file shows that this evaluation ranges from 0% to 2%. Table 4 delineates the primary attributes that differentiate Landsat sensors' scene images from each other.

Landsat Scene identifier	Date acquired	Cloud cover	Datum/UTM zone	Sun elevation	Sun Azimuth
LE71850302001093EDC00	2001/04/03	0	WGS84/34N	47.31	145.81
LE71850302001189SGS00	2001/07/08	2	WGS84/34N	61.74	129.79
LE71850302001221NSG01	2001/08/09	3	WGS84/34N	56.13	136.79
LE71850302001301NSG01	2001/10/28	8	WGS84/34N	31.25	159.32
LT51850302009107MTI00	2009/04/17	20	WGS84/34N	52.11	142.72
LT51850302009203MOR00	2009/07/22	1	WGS84/34N	59.75	131.92
LT51850302009267MOR00	2009/09/24	3	WGS84/34N	42.81	152.63
LT51850302009283MOR00	2009/10/10	14	WGS84/34N	37.34	156.76
LC81850302019087LGN00	2019/03/28	5.37	WGS84/34N	45.79	149.77
LC81850302019167LGN00	2019/06/16	13.66	WGS84/34N	64.52	134.95
LC81850302019183LGN00	2019/07/02	0	WGS84/34N	63.85	133.92
LC81850302019231LGN00	2019/08/19	0.12	WGS84/34N	55.05	144.32
LC81850302019295LGN00	2019/10/22	0.01	WGS84/34N	34.06	161.91

Table 3. Characteristics of Landsat satellite imagery used in this study

4.3 LANDSAT SPECTRAL BAND INFORMATION AND COMBINATIONS

The utilisation of Landsat satellite sensor data, encompassing visible, IR, and thermal spectral channels, has been made possible in a number of academic fields. The data collected by Landsat is used in several fields, such as global change research, agriculture, forestry, geology, land cover mapping, resource management, water studies, and shoreline analysis (USGS, 2022).

Band	L8 OLI/TIRS		L7 ETM+/ L4 TM		Important in mapping
	BN	WL	BN	WL	
Coastal/Aerosol	1	0.43–0.45			Coastal and aerosol research
Blue	2	0.45–0.51	1	0.45–0.52	Bathymetric mapping differentiates soil from vegetation and deciduous from coniferous
Green	3	0.53–0.59	2	0.52–0.60	Peak vegetation assessment aids in plant vigor evaluation
Panchromatic	8	0.50–0.68	8	0.52–0.90	15m resolution, higher detail in images
Red	4	0.64–0.67	3	0.63–0.69	Discriminates vegetation slopes
NIR	5	0.85–0.88	4	0.77–0.90	Focuses on biomass composition and shorelines
Cirrus	9	1.36–1.38			Improved cirrus cloud contamination detection
SWIR-1	6	1.57–1.65	5	1.55–1.75	Discriminates soil and vegetation moisture content; penetrates thin clouds
SWIR -2	7	2.11–2.29	7	2.09–2.35	OLI- Increased soil and plant hydration; breaks through light clouds. TM/ETM+ - Mineral deposits are connected with hydrothermally altered rocks
TIR 1	10	10.60–11.19	6	10.40–12.50	Estimating soil moisture using thermal imagery
TIR 2	11	11.50–12.51			Enhanced thermal mapping and soil moisture estimation

Table 4. Spectral band properties of Landsat 4, 7, and 8, with descriptions of their typical applications. Adapted from "What are the best Landsat spectral bands for use in my research?," U.S. Geological Survey (n.d.).

Table 4 summarises the Landsat sensor bands most advantageous for mapping LCLU. It provides an overview of the spectral bands for Landsat 4, 7, and 8, along with descriptions of how each band can assist users in selecting the most suitable band combinations for data

analysis (U.S. Geological Survey, n.d.). The descriptions of band applications are adapted from the U.S. Geological Survey FAQ on the best Landsat spectral bands for research.

Specific items that are located on the surface of the earth may be recognised, and information can be gleaned about them if the wavelength of each spectral band is taken into account. During the process of image interpretation, more than one band may be picked, and the combination of those bands permits the identification of additional objects, particularly bands that are indiscernible to the naked eye. When attempting to visualise data in colour, the various bands may be blended into a mixture of red, green, and blue, which is denoted by the acronym RGB. The following is a sampling of the most frequently used Landsat RGB (colour composite) band combinations (BC) for object feature delineation. Figure 12 displays the RGB band combination output of Landsat sensors 4, 5, 7, and 8 (Incorporation, 2023) together with their possible informational content (Quinn, 2001).

The "natural colour" RGB combination renders ground characteristics in human-visible colours using visible bands. For urban studies, it shows water purity, silt, and depth. It has trouble distinguishing sparse vegetation from other environments, and clouds and snow seem white. Shallow water does not separate soil from plant species, making it impossible to distinguish (Quinn, 2001).

The "Colour Infrared (CIR)" composite analyses crop, soil, and vegetation development using NIR, red, and green bands. Urban areas are cyan blue, vegetation is red, and soils are dark to light brown. Coniferous trees are deeper red than hardwoods, and intensities reflect vegetation richness, whereas lighter reds suggest grasslands or sparse vegetation. Urban regions are light blue (Quinn, 2001). "False Colour (urban)" with SWIR-1, SWIR-2, and Red penetrates smoke and haze. It depicts sand, dirt, and minerals in different colours and plants and urban buildings in green. Mid-IR band absorption distinguishes water, ice, and snow. This combination helps identify floods and forest fires since hot surfaces, like forest fires, are reddish or yellow.

"Vegetation Analysis" uses SWIR1, NIR, and red bands to contrast bare soil with vegetation in varied environments, suitable for examining plants, soil moisture, and water bodies. The mix's red hue and high plant signals make it ideal for remote sensing in agriculture, forestry, and wetlands. The soil appears purple, and the vegetation is brilliant green. It provides a complete image of soil moisture and water distribution (Incorporation, 2023).

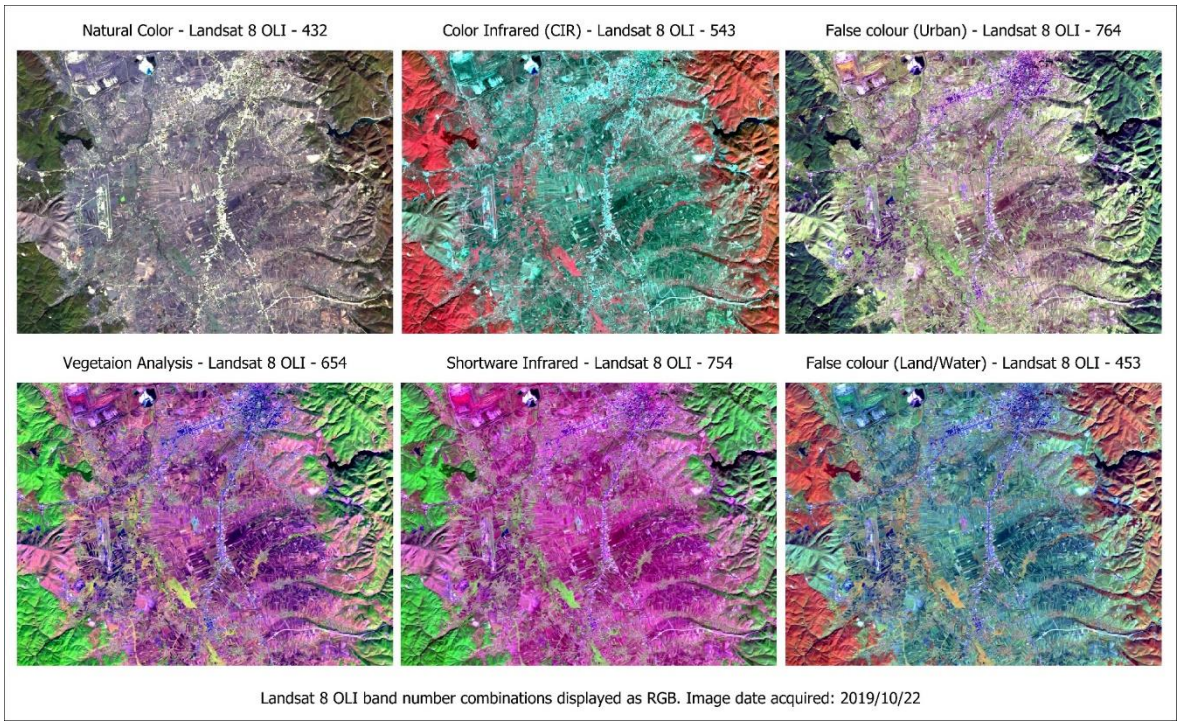

Figure 13. Landsat 8 OLI band combination displayed as RGB for a subset of the study area.

The "Agriculture" combination uses SWIR1, NIR, and blue bands to monitor and identify crops using NIR vegetation reflectance. With low light absorption in water, crops differ from bare soil and trees. Urban areas are darker, making croplands and meadows visible (Incorporation, 2023).

Drainage, soil, vegetation, and agricultural studies employ the "Shortwave Infrared" composite with SWIR2, NIR, and red bands. Vegetation is red, soils are light brown, and cities are cyan blue. Densely inhabited regions are light blue, and hardwoods are lighter red than conifers. It recognises burnt land, lava, flames, and hot landforms and highlights minerals in brilliant colours for geological mapping (Incorporation, 2023).

The "Land/Water" NIR, SWIR1, and Red bands clarify land-water boundaries and expose fine details. Lakes and streams are precisely located, and plant kinds and conditions indicate moisture variations. This combination aids soil and vegetation studies (Quinn, 2001).

4.4 ANICILARY DATA

The additional data we obtained was crucial to our research, improving our capacity to precisely identify and validate the samples gathered for land cover categorization and

precision assessment. Ancillary data has been extensively recorded to aid in distinguishing classes that are often difficult to differentiate using just remotely sensed data (Foody, 1994; McIver & Friedl, 2002).

The research employed high-resolution orthophotos from 2001, 2009, and 2018, obtained through the WMS (http://geoportal.rks-gov.net/wms) of the Kosovo Cadastral Agency, as well as very high-resolution (VHR) satellite imagery from Google Earth Pro (Google, n.d.). Additionally, datasets from the CLC (Copernicus, n.d.). for 2006, 2012, and 2018, along with the OpenStreetMap dataset (OpenStreetMap contributors, n.d.) , were utilised.

These resources were crucial in accurately understanding the training samples that were not clearly visible in the multi-spectral composite Landsat images alone. Other data that were used to create spatial variables are: Digital Elevation Model (DEM), along with its derivative slope, roads, rivers, lakes and settlements.

4.5 SOFWTARE AND TOOLS

The utilisation of many software programmes and technologies in the realm of Remote Sensing greatly enhances data processing, classification analysis, visualisation, and interpretation. The complete accomplishment of the project's objectives was achieved by leveraging the capabilities of both QGIS (QGIS Development Team, 2021) and ENVI (Harris Geospatial Solutions, n.d.). QGIS, short for Quantum Geographic Information System, is a widely recognised open-source Geographic Information System (GIS) software that offers a range of useful functionalities (QGIS Development Team, 2021). ENVI, developed by Exelis Visual Information Solutions in Boulder, Colorado, is a specialised software designed exclusively for image processing and analysis. However, its source code is not accessible to the public (Harris Geospatial Solutions, n.d.).

Google Earth Pro is a software application that provides users with access to historical, high-resolution satellite imagery. It also allows for the visualisation, evaluation, overlay, and creation of geographical data (Google, n.d.).

The creation of text, tables, and graphs was facilitated by the use of Microsoft Word and Excel, which are components of the Microsoft Office suite (Microsoft Corporation, 2021). The MOLUSCE Module (QGIS Plugin) was recently made available to evaluate current

LCLU changes and predict the future of LCLU, which was applied in this study (NextGIS, 2025).

4.6 METHODOLOGY

The first step in the process is to gather spatial datasets from Landsat-5 TM, Landsat-7 ETM+, and Landsat-8 OLI for the years 2001, 2009, and 2019. After preprocessing raster images (cloud masking, clipping, stacking, etc.), samples were collected through photointerpretation of multi-temporal images and auxiliary data, such as local aerial photographs and Google Earth Pro.

Following that, the samples were divided into two groups: eighty percent were used to train the four classifiers (MD, ML, SVM-RBF, and NN), and twenty percent were used to test their classification accuracy. After evaluating the accuracy of the classifier, the LCLU map was selected from the classifier with the best performance for the three time periods: 2001, 2009, and 2019.

The analysis of changes in LCLU in the time intervals 2001–2009, 2009–2019, and 2001–2019 was realised through transit matrix tables, which were presented through maps, tables, and graphs. We used the CA-ANN model for the years 2019, 2029, and 2039 to predict the future of LCLU in the study area. The following sessions show in detail each process of the work methodology applied in this study.

4.6.1 IMAGE PRE-PROCESSING

4.6.1.1 Cloud and cloud shadows masking

The Landsat 4-7 and 8-9 series, which are part of the Collection 2 Level-2 Science Products (L2SP), include a QA_PIXEL band. The band is generated using the CFMask algorithm (version 3.3.1) (Zhu & Woodcock, 2012; Zhu, Wang, & Woodcock, 2015) and is stored in compressed layers, provided by the U.S. Geological Survey [USGS] (n.d.). The purpose of this encoding is to capture information on clouds, their shadows, as well as snow or ice present in an image.

By analysing the values in the QA_PIXEL band, we effectively identified and separated cloud and shadow regions in many temporal situations. Notably, the Landsat 5 and 7 QA_PIXEL band values differ from those of Landsat 8. The following time-lapse images

illustrate the application of masking techniques to clouds and their corresponding shadows. In order to produce these masks, we cropped the QA_PIXEL bands from the multi-temporal images to match the dimensions of our designated study region. We utilised the Landsat Collection 2 Level-2 Science Products Guide (Sayler & Zanter, 2021; Sayler & Zanter, 2023) to establish recommendations. By visually inspecting the scenes, we successfully identified and extracted pixels representing a clear sky and water. We excluded cloud and shadow pixels from this process. To convert these pixels from raster to vector format, we employed the tools available in QGIS (QGIS Development Team, 2021) .

Sensor	Path/row	Date acquired	Pixel value	Interpretation	Area km^2	%
ETM+	185/30	2001-04-03	5440	Clear with low set	2275.12	99.56
ETM+	185/30	2001-07-08	5440	Clear with low set	2283.32	99.92
ETM+	185/30	2001-08-09	5440	Clear with low set	2271.04	99.38
ETM+	185/30	2001-10-28	5440	Clear with low set	2250.45	98.48
TM5	185/30	2009-04-17	5440	Clear with low set	2115.83	92.59
TM5	185/30	2009-07-22	5440	Clear with low set	2282.48	99.88
TM5	185/30	2009-09-24	5440	Clear with low set	2266.78	99.20
TM5	185/30	2009-10-10	5440	Clear with low set	2282.0	99.86
OLI/TIRS	185/30	2019-03-28	21824	Clear with low set	2049.24	89.68
OLI/TIRS	185/30	2019-06-16	21824	Clear with low set	1955.53	85.58
OLI/TIRS	185/30	2019-08-19	21824	Clear with low set	2284.64	99.98
OLI/TIRS	185/30	2019-10-22	21824	Clear with low set	2277.35	99.66

Table 5. Image scenes and application of cloud and shadow masking

We matched images from the Landsat sensor's optical channels (TM, ETM, and OLI) for the selected years (2001, 2009, and 2019). The channels encompassed are Blue, Green, Red, NIR, SWIR 1, and SWIR 2. Subsequently, we utilised related vector mask layers to precisely clip each multispectral band. The area of our investigation was the only place where images were unaffected by cloud cover. The multispectral bands were extracted using the

corresponding vector mask layer for each image scene. Cloud-free portions of the images were clipped to the boundaries of the study area to ensure consistency in spatial coverage. Subsequently, the selected multispectral bands from the bi-temporal images for each time period were stacked using the merge tool. By carefully selecting bands to enhance the visibility of land cover features and adjusting the display from true color to false color composites, the resulting imagery can highlight specific land cover characteristics more effectively.

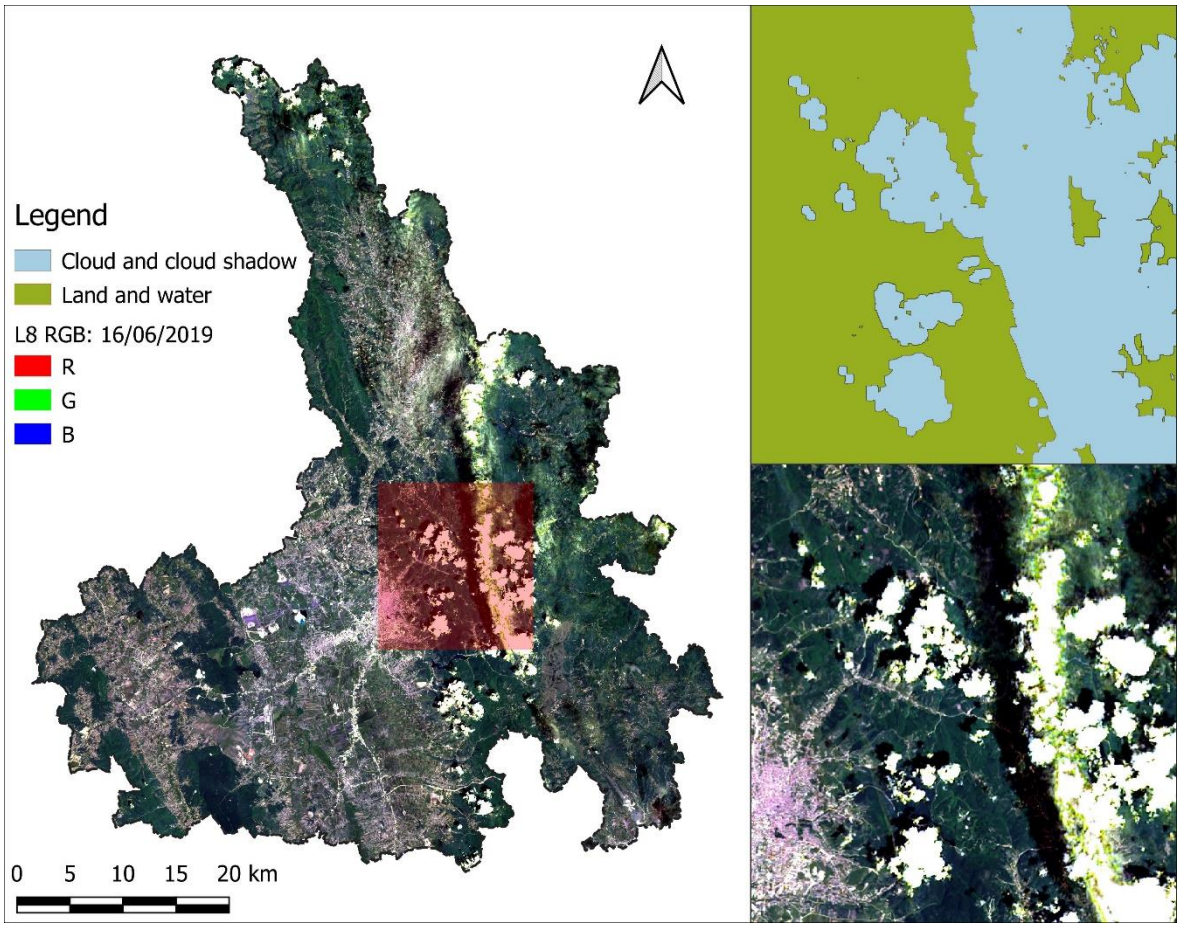

Figure 14. Cloud and shadow masking over the study area.

4.6.1.2 Surface reflectance values

To appropriately use the data, the U.S. Geological Survey [USGS] (n.d.) recommends applying a scaling factor to the Landsat Level-2 surface reflectance and surface temperature outputs. Surface reflection is provided in the L2SP as unsigned 16-bit integer data with a permitted range of 1 to 65455. As a result, each pixel requires a scaling factor of 0.0000275 and a -0.2 offset. This scaling factor must be calculated individually for each layer of the stacked images.

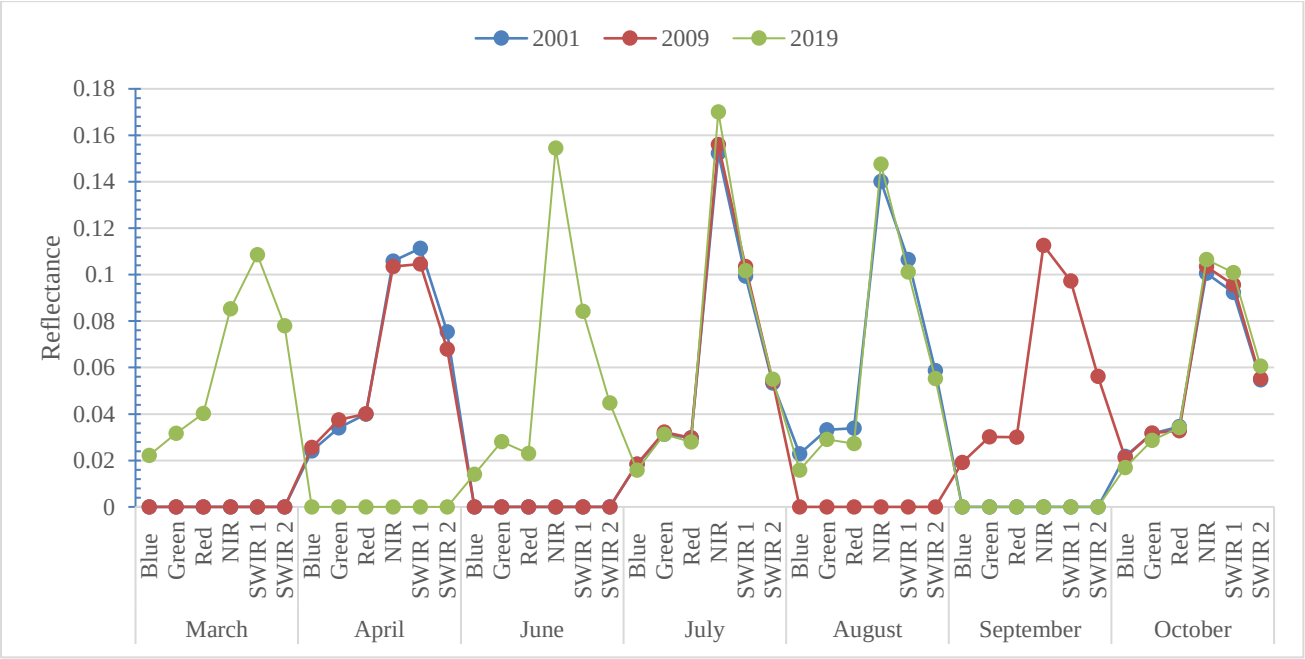

Figure 15. Spectral signature profiles of multi-temporal stack images (2001–2019).

Figure 14 shows a line graph that compares the mean surface reflectance values for the study area across multiple spectral bands (Blue, Green, Red, NIR, SWIR1, and SWIR2) over a period of several months (March to October) from three different Landsat sensors (ETM+ for 2001, TM for 2009, and OLI for 2019).

The red line (2009, TM) and blue line (2001, ETM+) are both at zero in March, indicating no data. The green line (2019, OLI), on the other hand, is above zero for every band and indicates the existence of data for this month. Zero values in months of the multi-temporal sensor data indicate that the image scenes were not used in the study due to the high cloud cover percentages. The blue and red lines (2001, ETM+, 2009, TM) are above zero in April, whereas the green line (2019, OLI) falls to zero. In June, we only have data from the OLI sensor; in July, all Landsat sensor lines are above zero for every band. The red line (2009, TM) drops to zero in August, indicating no available data; however, in September, the TM sensor provides information for additional bands. All of the Landsat sensor bands' lines are above zero in October, showing the existence of data.

Reflectance, or the fraction of sunlight reflected from the surface in each spectral band, is represented by the numbers on the y-axis. This makes it possible to look into temporal variations, which might result from changes in the environment, land use, or seasonal variations. There are clear seasonal trends, with certain bands displaying the highest mean

reflectance value in specific months. There are obvious seasonal patterns, with certain bands peaking in particular months (the NIR band, for example, often increases in the summer and may be related to plant growth).

Comparisons across years reveal a significant increase in NIR over time. The 2001 ETM+ data show a notable peak in NIR in June, indicating a season of lush vegetation. A similar peak is observed in the 2009 data; however, it is less pronounced than in 2001. Similar trends may be seen in the 2019 OLI data, which is somewhat less than in 2001 but greater than in 2009. While variations between months within a given year can be attributed to seasonal influences, differences between the same months over several years may suggest consistent changes in the Earth's surface. The visible spectrum (blue, green, and red) shows constant fluctuations over the years.

4.6.2 LAND COVER AND LAND USE NOMENCLATURES

Before commencing sample collection and classification in a land cover project, it is crucial to first determine the land cover categories. The identification process relies on several factors, such as the project type, the geographical area under study, the diversity of classes found in that area, the characteristics and methodology of the imagery used for classification, the classification techniques employed, and the anticipated project results.

To achieve effective categorization, the scheme must be all-encompassing but exact, with well-defined, non-overlapping groupings that are organised in a hierarchical way. According to Yuan et al. (2005), the goal of this strategy is to lessen misclassifications and meet users' information needs. Our research uses the categorization method, which is based on the CLC terminology (Büttner et al., 2021). We have discovered and classified eight distinct LCLU categories. The specific classifications and descriptions of these classes are outlined in Table 8.

Class	Description
Agriculture	This category contains annual crops such as cereals, root crops, leguminous, fodder, lucerne, vegetables, pastures and bare soil on farmed land.
Bare surfaces	This group includes rocky, bouldery, or rubbly slopes with sparse vegetation of herbaceous, ligneous, and semi-ligneous species.

Forest	Broad-leaved or coniferous tree-dominated forests
Grassland	This category contains natural grasslands with little human impact, poor production, and frequent rough, uneven terrain, steep slopes, and rocky places.
Industrial	This category includes land units used for industrial and commercial purposes, as well as highways, railroads, airports, open-pit extraction sites, public dumps, and construction projects.
Transitional land	This category comprises clear cuts in forest regions, previously burned forest, semi-natural succession with bushes of mineral extraction sites and waste sites, and abandoned agricultural fields.
Urban	Facilities of rural and urban settlements
Water bodies	This class includes running water of the rivers, natural and artificial lakes, man-made reservoirs and canals containing artificial water.

Table 6. Land cover/use classification scheme and legend adopted in the study

4.6.3 IMAGE INTEREPRETATION AND SAMPLE COLLECTION

Following the determination of the land cover nomenclature for the study region, the interpretation and collection of samples were carried out using a false colour combination of satellite images and orthophoto and GE reference data for the years 2001, 2009, and 2019. All samples were obtained in 1969 for eight different land cover groups. When the samples were collected, the geographical class distribution in the research area and the differences in the spectral reflectances of the object features were taken into account.

Stratified sampling is a technique for splitting a population into discrete subgroups based on certain features and then randomly choosing samples from each stratum. This strategy ensures inclusion in several subcategories. A stratum's sample proportion is computed by dividing its size by the entire population size and multiplying the result by the desired overall sample percentage, ensuring that the sample size in each stratum is proportional to its size (Cochran, 1977).

Since the samples were collected simultaneously using very high-resolution images, the training set was divided according to percentage strata: 80% were used for classification, and 20% were reserved for validation. This is accomplished in QGIS using the split train technique and the validation of the Dzetsaka plugin (Karasiak, 2016).

4.6.3.1 Distribution statistics of the training samples

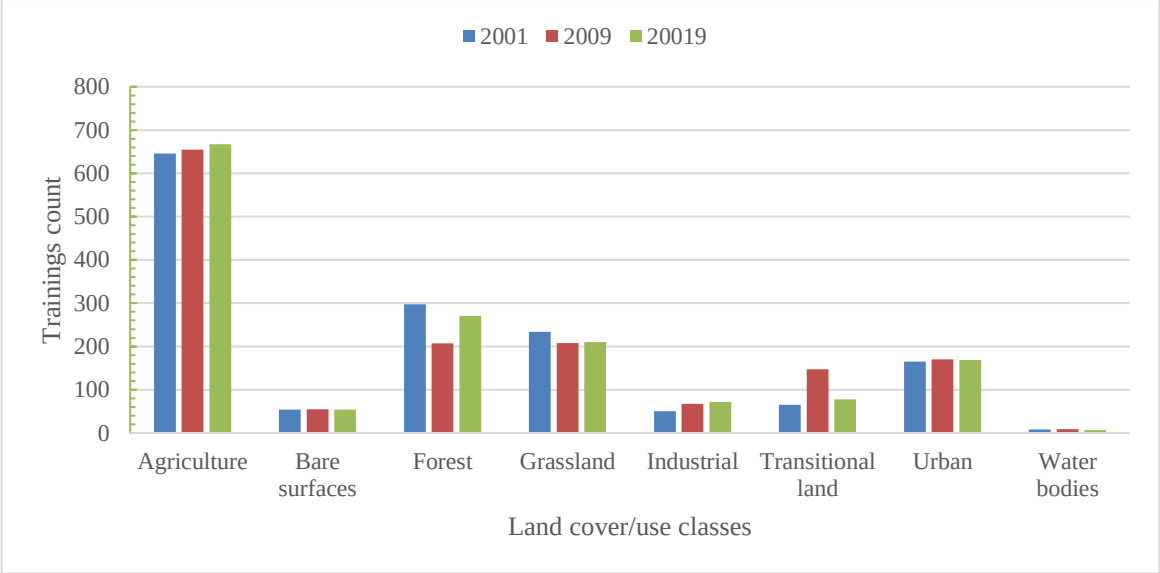

Figure 16. Distribution of training samples for LCLU classes by year.

Figure 15 displays a bar graph illustrating the quantity of training samples gathered for different land cover and use categories in the years 2001, 2009, and 2019. In 2001, agriculture had the highest number of training samples. There was a slight decrease in 2009, although it remained close to the levels seen in 2001. The number of samples obtained for bare surfaces was much lower compared to agriculture, which had the fewest samples. The woodland class initially contained a substantial quantity of samples, around 650, in 2001. However, by 2019, the number had notably risen, surpassing the level observed in 2001.

From 2001 to 2009, the grassland area declined significantly, followed by a slight increase in 2019 compared to 2009. Nevertheless, the 2019 grassland area remained well below the level recorded in 2001. Between 2001 and 2009, the samples of industrial land classes exhibited very low levels and were mostly consistent. Nevertheless, there was a little increase in 2019, indicating a small rise in interest or the availability of samples for this category. The number of samples on transitional land was initially low in 2001, increased in 2009, and then had a little decline in 2019. The quantity of samples gathered in 2019 remained higher than in 2001, demonstrating sustained growth over the course of a decade. In 2019, there was an initial decrease in the number of samples collected from urban areas and transitional land. However, there was an increase that followed, which might indicate changes in land use goals or the accessibility of data. The grassland and industrial classes

exhibit less variability over time, but their sample sizes differ from those of the agricultural and forest classes.

Feature space evaluation of the training samples for the year 2001, 2009 and 2019

As shown in Figure 16, the NIR band in 2001 exhibited elevated reflectance values, which is typical for vegetation due to the strong reflection of chlorophyll. The SWIR bands, particularly SWIR 1, exhibited variability among classes, proving to be efficient in distinguishing both plant and land cover types. Bands of blue, green, and red wavelengths exhibit reduced reflectance values and are commonly used for the identification of features such as bodies of water and urbanised areas. The overlap in the visible bands demonstrates the presence of similar characteristics in the spectral signatures of various classes.

The NIR and SWIR bands exhibited a wider spectrum of values, indicating more dissimilarity, hence facilitating the differentiation of classes based on their spectral characteristics. In general, the reflectance and spectral characteristics of the bands provide valuable data for the classification of vegetation and land cover.

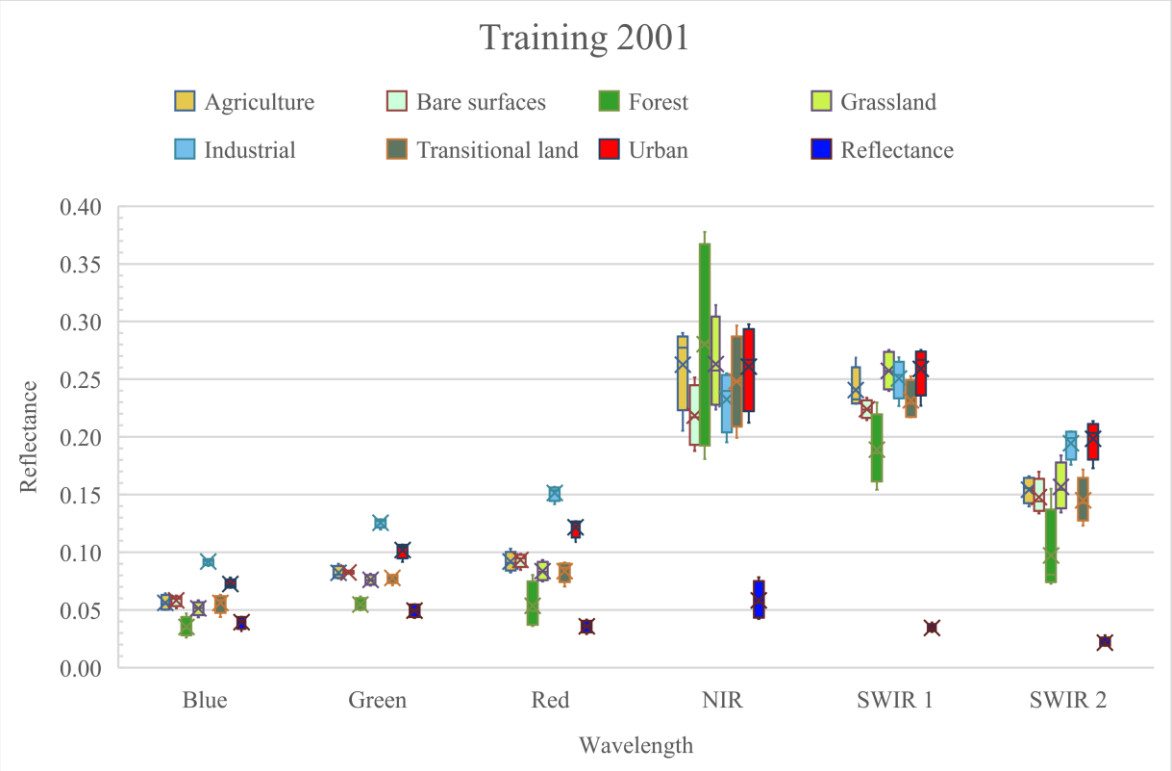

Figure 17. Boxplot of mean spectral signatures for LCLU classes in 2001.

In 2009, the reflectance levels in the NIR and SWIR bands were significantly high for most classes in 2009, indicating the presence of vegetation. The bands exhibited a diverse range of reflectance values, indicating their ability to distinguish between different types of terrain. The reflectance levels in the blue, green, and red bands exhibited a decrease, but the differences were less noticeable. The observable spectral bands (blue, green, and red) showed a comparatively smaller disparity across classes, suggesting that discerning between classes using visible wavelengths could be a greater challenge. The NIR and SWIR bands exhibited clear differentiation, as shown by the dispersion of values that displayed unique spectral characteristics for each land cover category.

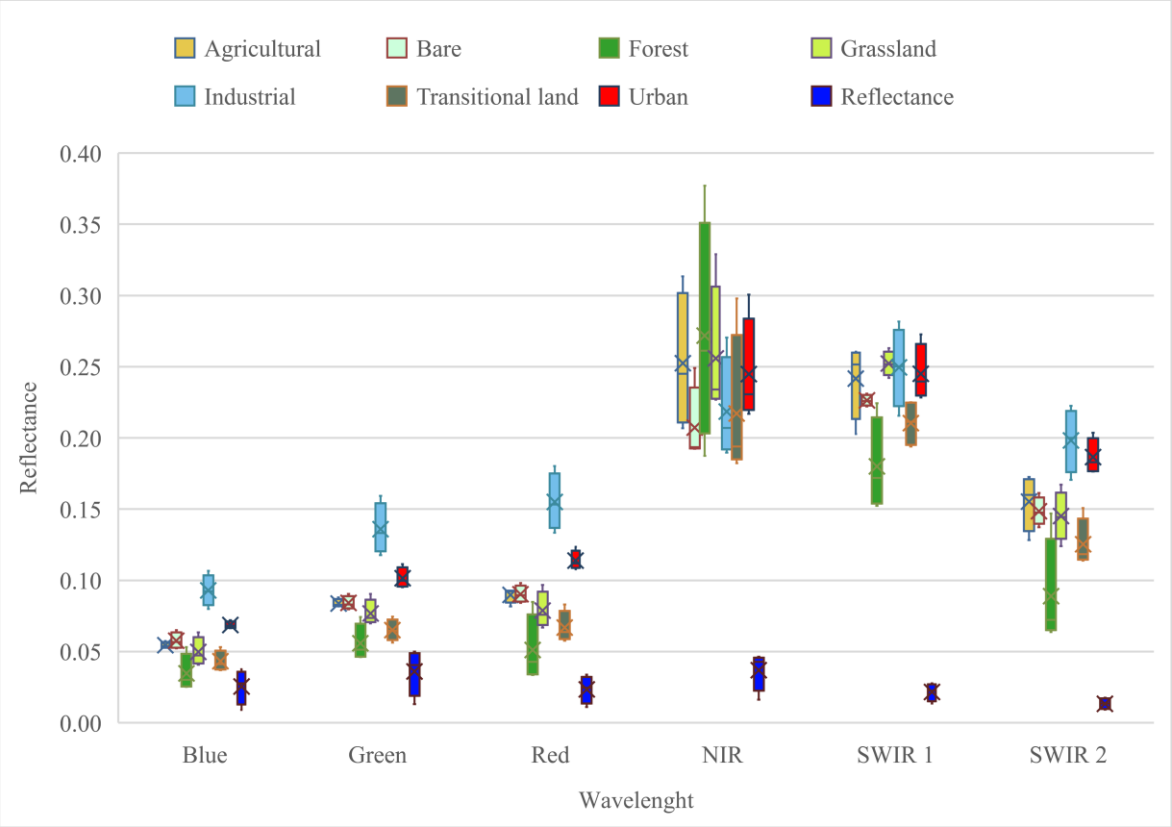

Figure 18. Boxplot of mean spectral signatures for LCLU classes in 2009.

In 2019 reflectance values span from 0 to about 0.45, with greater values indicating a larger amount of light being reflected off the surface at that specific wavelength. The box plots display the median, interquartile range, and range, while representing outliers as individual data points or stars located outside the whiskers.

Different land cover types exhibit distinct variations in reflectance. Forests demonstrate higher reflectance in the NIR wavelength, while both forest and grassland types exhibit

higher reflectance in the NIR wavelength. In contrast, urban and industrial areas display lower reflectance values across all wavelengths compared to natural surfaces. Barren surfaces, on the other hand, exhibit high reflectance in the SWIR wavelengths.

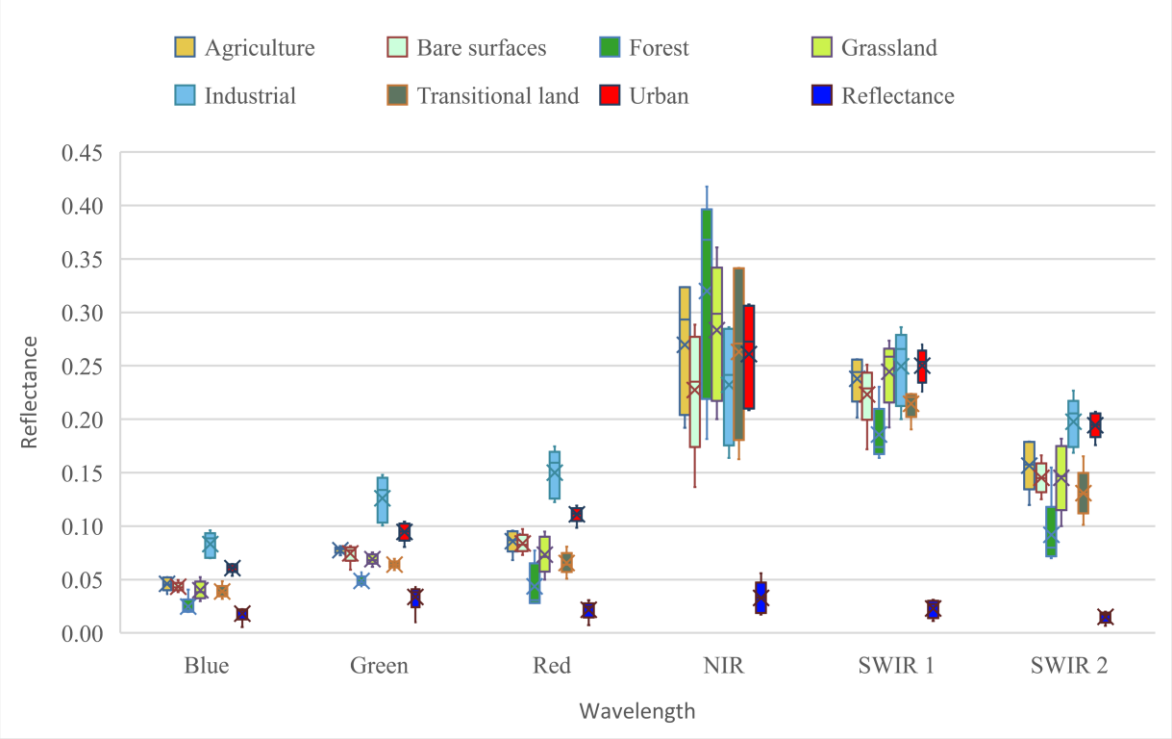

Figure 19. Boxplot of mean spectral signatures for LCLU classes in 2019.

In summary, the reflectance in the visible band was lower in the vicinity of water bodies and urban areas. By contrast, the NIR and shortwave reflectance values consistently indicated the presence of vegetation across all three time periods. The NIR and SWIR bands remained essential for distinguishing various land cover types. The distinctiveness of spectral fingerprints seems to have evolved throughout time.

In 2001, there was a noticeable overlap within bands, but by 2019, there was a significant increase in the range of reflectance values, even those in the visible band. This suggests that some classes may be more distinguishable than others. Using visible light to distinguish various land cover types was easier in 2001, became more difficult in 2009, and improved again by 2019.

4.6.4 QUANTITATIVE EVALUATION OF THE SAMPLES

The Jeffries-Matusita (JM) distance is a statistical measure used in multivariate statistical analysis to find out how different or separable two probability density functions (PDFs) or

classes are from each other. It is very advantageous in the domains of pattern recognition, classification, and remote sensing. Jeffries and Matusita introduced it during the 1960s (Jeffries, 1963; Matusita, 1967; Swain & Davis, 1978), and it functions as a good instrument for evaluating the discernibility of classes in feature space.

The JM distance is a widely used method for quantifying the distinguishability of spectral bands in multidimensional data. This tool is used for selecting the most optimal bands and evaluating the performance of both supervised and unsupervised classification approaches (Dabboor et al., 2014). JM separability is a fundamental and straightforward parametric criterion that may be easily implemented. It has a defined range of values from 0 to 2. The implementation is based on using a statistical distribution of data, often a multivariate normal distribution of the tested class samples.

The JM distance Jxy is computed using the following formula, as described by Richards and Jia (2006):

$$J_{xy} = 2(1 - e^{-B})$$

where:

$$B = \frac{1}{8}(x-y)^t \left(\frac{\Sigma_x + \Sigma_y}{2}\right)^{-1} (x-y) + \frac{1}{2} ln \ln \left(\frac{\left|\frac{\Sigma_x + \Sigma_y}{2}\right|}{|\Sigma_x|^{\frac{1}{2}} |\Sigma_y|^{\frac{1}{2}}} \right)$$

where:

- x = first spectral signature vector;
- y = second spectral signature vector;
- Σx = covariance matrix of sample x;
- Σy = covariance matrix of sample y;

Using the matemathical formula above, we applied the JM distance for the three study years using ENVI tools to assess spectral separability.

Interpretation of the JM results

The diagonal of the matrix is filled with the number 0, which represents the distance between two classes. The lower scores for the highlighted cells indicate that certain combinations of land cover categories may be more challenging to distinguish because of their increased spectral similarity. With a JM distance of 2.00 separating them from all other land cover types, water bodies are the most different groupings.

2001. With JM distances of 1.75 and 1.73, respectively, grassland and agricultural as well as grassland and transitional terrain are the most difficult to differentiate. The urban and industrial groups are somewhat more similar, despite their continued extreme separation (JM distance of 1.88). All things considered, the table provides helpful information on the spectral signatures of various land cover types and their separability.

	Agriculture	Bare surface	Forest	Grassland	Industrial	Transitional land	Urban	Water bodies
Agriculture	-							
Bare surface	1.99	-						
Forest	2.00	1.99	-					
Grassland	1.75	1.93	1.97	-				
Industrial	1.97	1.99	2.00	1.99	-			
Transitional land	1.87	1.97	1.95	1.73	1.97	-		
Urban	1.91	2.00	2.00	1.97	1.88	1.96	-	
Water bodies	2.00	2.00	2.00	2.00	2.00	2.00	2.00	-

Table 7. Jeffries–Matusita spectral distances for 2001

2009. JM distance differences amongst land cover categories are shown in the table 6. The JM distance of 2.00 between agricultural, forest, barren surfaces, forest, and urban land cover classes indicates strong separability. The spectral fingerprints of agriculture and grassland are comparable, with a distance of 1.90. The lowest values, 1.57, show the most spectral signature overlap and the greatest difficulty separating these groups.

With all JM distances between industrial and other land covers at 2 or near it, they are well separated. Water bodies are fully separable (2) from all other land cover categories, supporting the idea that water has a particular spectral signature. Transitional land and

grassland had the lowest JM distance (1.57), indicating strong spectral similarities and probable misunderstanding. Transitional land is likewise close to agricultural (1.88) and barren terrain (1.84), suggesting some similarities.

	Agricultural	Bare surfaces	Forest	Grassland	Industrial	Transitional land	Urban	Water bodies
Agricultural	-							
Bare surfaces	1.98	-						
Forest	2.00	2.00	-					
Grassland	1.90	1.86	1.97	-				
Industrial	1.99	1.99	2.00	2.00	-			
Transitional land	1.88	1.84	1.86	1.57	1.99	-		
Urban	1.90	1.99	2.00	1.98	1.89	1.98	-	
Water bodies	2.00	2.00	2.00	2.00	2.00	2.00	2.00	-

Table 8. Jeffries–Matusita spectral distances for 2009

2019. The Table 9 illustrates JM distance dissimilarities across land cover groups, with values around 2 suggesting good separability and values below 2 indicating poor separability. Agricultural land is more distinct from bare surfaces, woodlands, and aquatic bodies (JM distance of 2.00) than grassland and transitional terrain (1.95). Urban areas are separate (1.98 JM distance). Bare surfaces stand out of all other land covers (JM distance 2.00). The JM distance of 2.00 separates grassland from forest, industrial, urban, and aquatic bodies, but 1.88 from agricultural and transitional terrain. Industrial land is distinct from all other land covers except urban, which has a separation distance of 1.96. Water bodies stand out the most as land cover. JM distance of 1.88 indicates that grassland and transitional terrain are hardest to distinguish. Urban and industrial zones have a JM distance of 1.96, showing spectral similarities.

	Agricultural	Bare surfaces	Forest	Grassland	Industrial	Transitional land	Urban	Water bodies
Agricultural	-							
Bare surfaces	2.00	-						

Forest	2.00	2.00	-					
Grassland	1.95	1.99	2.00	-				
Industrial	2.00	2.00	2.00	2.00	-			
Transitional land	1.95	1.99	1.99	1.88	2.00	-		
Urban	1.98	2.00	2.00	2.00	1.96	1.99	-	
Water bodies	2.00	2.00	2.00	2.00	2.00	2.00	2.00	-

Table 9. Jeffries–Matusita spectral distances for 2019

Using JM class distances for comparison

The JM measures of separability for land cover classes throughout 2001, 2009, and 2019 are presented in Figure 20 wich indicate an increasing trend in agriculture.

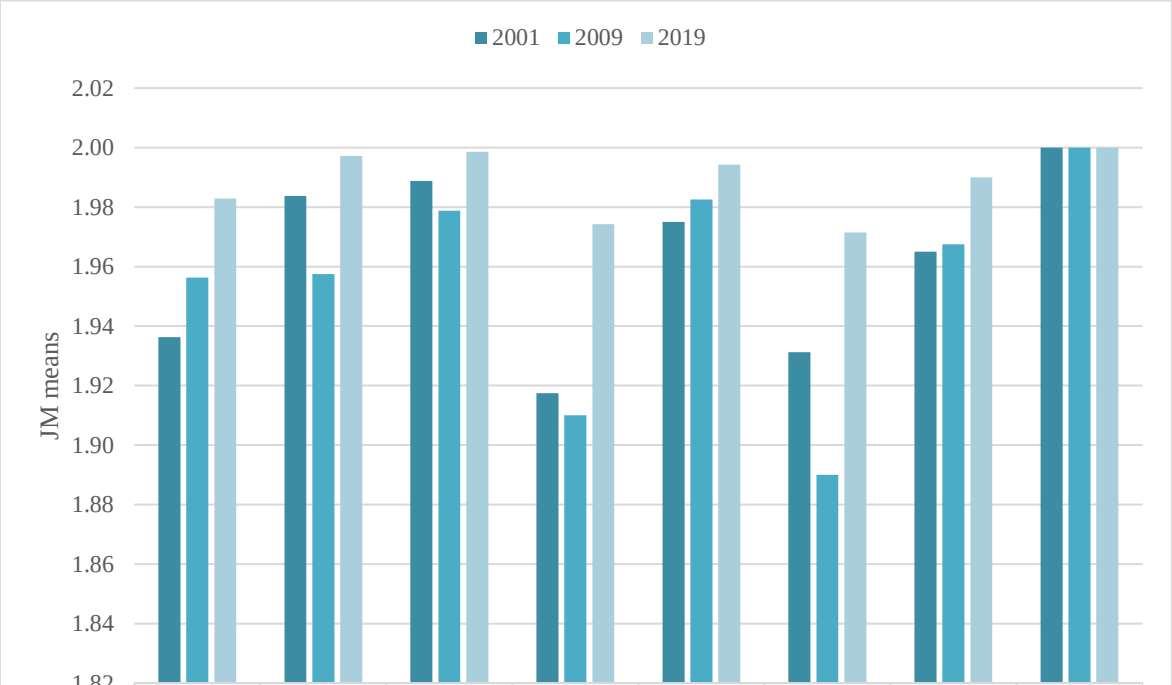

	Agriculture	Bare surface	Forest	Grassland	Industrial	Transitional land	Urban	Water bodies
2001	1.94	1.98	1.99	1.92	1.98	1.93	1.97	2.00
2009	1.96	1.96	1.98	1.91	1.98	1.89	1.97	2.00
2019	1.98	2.00	2.00	1.97	1.99	1.97	1.99	2.00

Figure 20. Jeffries–Matusita (JM) mean distance comparison for the study period.

The forest class has the highest JM mean value, suggesting great separability. Grassland decreased from 2001 to 2009 and then increased significantly in 2019, suggesting that distinguishing grassland from other land cover classes may have been challenging in 2009 but became easier by 2019. The industrial class gradually becomes more distinct from other land cover types. Transitional land decreases from 2001 to 2009 and increases by 2019,

comparable to grassland. Urban areas are becoming more segregated, from 1.97 in 2001 to 1.99 in 2019. Water bodies have a JM mean of 2.00 each year, indicating complete separability and no change over time. The decrease in JM means for grassland and transitional land from 2001 to 2009 may indicate that these classes became more similar to other land cover categories. By 2019, these classifications were more distinct, probably due to land cover changes.

4.7 IMAGE CLASSIFICATION APPROACHES

To realise the classification of the land cover/use for the time periods 2001, 2009, and 2019, the multi-stack images that combine the reflective spectral bands from the spring to the autumn seasons were used. From the supervised classification method, MD, ML, SVM-RBF, and NN algorithms were implemented using the eight LCLU category sample classes.

4.7.1 MAXIMUM LIKELIHOOD

The Maximum Likelihood (ML) classifier is a widely used method in the domains of remote sensing and image analysis for supervised classification (Richards & Jia, 2006). This classification methodology utilises labelled training samples to estimate the statistical properties of each class, such as the mean and covariance. Subsequently, it computes the likelihood of a pixel being assigned to a certain class by using these statistical measures. The ML classifier assigns each pixel to the class with the highest probability (Richards & Jia, 2006), based on the following equation:

where:

$$g_k(x) = \ln p(C_k) - \frac{1}{2}\ln|\Sigma_k| - \frac{1}{2}(x - y_k)^t \Sigma_k^{-1}(x - y_k)$$

n which C_k is class k, x is the spectral vector of the pixel, $p(C_k)$ is the prior probability of the class, $|\Sigma_k|$ and Σ_k^{-1} are the determinant and inverse of the class covariance matrix, and y_k is the class mean vector. A pixel is assigned to class C_k if $g_k(x)$ is greater than for all other classes. Therefore:

$$x \in C_k \Leftrightarrow g_k(x) > g_j(x) \forall k \neq j$$

Using the ENVI program, we applied two main parameters with the aim of perfecting the process: a) Probability Threshold, which determines the minimum probability for classification; b) Data Scale Factor (default 1.00) controls how the covariance matrix is scaled, normally left at default. We applied Single Value threshold for eight LCLU class samples (Agriculture, Bare surfaces, Forest, Grassland, Industrial, Transitional land, Urban, and Water bodies), where each pixel was assigned to its most likely class.

ML is capable of efficiently handling multiclass classification problems, making it highly adaptable for applications involving multiple land cover or land use categories (Richards & Jia, 2006).

4.7.2 MINIMUM DISTANCE

The Minimum Distance (MD) is a supervised learning technique utilised to classify a given data point into one of many classes by evaluating its proximity to the mean vectors of those classes (Wacker & Landgrebe, 1972). The average vector (Congedo, 2021) for each class is calculated as:

$$d(x,y) = \sqrt{\sum_{i=1}^{n}(x_i - y_i)^2}$$

where: x is the spectral signature vector of the pixel; y is the average spectral signature vector of the training samples and n represents the number of spectral bands. Distance is measured for each pixel in the image and categorised by the closest spectral signature. This classification uses a modified discriminant function (Congedo, 2021; Richards & Jia, 2006) derived from Richards and Jia (2006):

$$x \in C_k \Leftrightarrow d(x,y_k) < d(x,y_j) \forall k \neq j$$

where:C_k is the land cover class k and, $y_k$and y_j are the mean spectral signatures of calssses k and class j as well.

We implemented MD through GIS by integrating several of its parameters: a) The maximum standard deviation from the mean (σ), limits the classification to pixels within a defined range σ around the class mean, excluding outliers; b) The maximum distance error, provides an upper bound on the Euclidean distance, leaving pixels unclassified if they exceed this limit. Both parameters can be specified as Single Value or Multiple Values. Single Value applies a global threshold across all classes, while Multiple Values allows for class-specific tolerances. In this study, we applied Single Value and provided uniform thresholds for all LCLU classes.

ML has been successfully used in remote sensing for crop species identification, as it is preferred for its simplicity and effectiveness with limited training samples (Wacker & Landgrebe, 1972).

4.7.3 RADIAL BASIS FUNCTION (RBF) - SVM

The RBF kernel is one of the most popular kernel functions, especially for non-linear data. SVM finds an efficient classification hyperplane using the RBF kernel to transform input data into a higher-dimensional space (Vapnik, 1995). Given that the RBF kernel can describe nonlinear decision boundaries (Schölkopf & Smola, 2002), it is preferable for complicated datasets such as satellite images. The mathematical representations of RBF are described below (Pedregosa et al., 2011):

$$K(\mathbf{x}_1, \mathbf{x}_2) = \exp(-\gamma \cdot \|\mathbf{x}_1 - \mathbf{x}_2\|^2)$$

Where: $K(\mathbf{x}_1, \mathbf{x}_2)$ - measures the similiratiy that exists between data points, $\|\mathbf{x}_1 - \mathbf{x}_2\|^2$ is their squared Euclidean distance, and γ (gamma) controls the influence of each training sample on the decision boundary.

We applied the SVM algorithm in the GIS environment, through its default value parameters: **a)** Gamma (0.033), determines the spread of the RBF kernel; **b)** Penalty Parameter (C) (100.000) balances the complexity of the model and tolerance to misclassification; **c)** Pyramid Levels (0), regulates the extraction of multi-scale features during training, and **d)** Classification Probability Threshold (0.00), allows the rejection of pixels with low classification confidence. These parameters are the basis for the kernel-based discriminant function, which works well on multi-spectral images.

4.7.4 NEURAL NET – MULTI-LAYER PERCEPTRON (MLP)

The MLP is implemented through the following main steps: forward propagation, loss function, backpropagation, and optimization (GeeksforGeeks, n.d.), based on backpropagation algorithm (Tso & Mather, 2009). In feedforward networks, data processing begins at the input layer, passes through the hidden layers, and proceeds to the output layer. The neuron in the hidden layers calculates the weighted sum of the input data (GeeksforGeeks, n.d.):

$$z = \sum_i w_i x_i + b$$

where w_i is the weight, w_i the input, and b the bias. This weighted sum is then passed through a nonlinear activation function such as the Sigmoid:

$$\boldsymbol{\sigma(z) = \frac{1}{1 + e^{-z}}}$$

which compresses values into the (0,1) range and allows real-valued data to be mapped to binary outputs. A loss function, often binary cross-entropy, compares predicted values with true labels:

$$\boldsymbol{L = -N1\sum i = 1N\left[yi\log\left(y^i\right) + (1 - yi)\log\left(1 - y^i\right)\right]}$$

where $\boldsymbol{yi}$ is the actual label, $\boldsymbol{y^i}$ the predicted value, and $\boldsymbol{N}$ the sample size.

The network is trained using backpropagation, which updates weights iteratively by gradient descent:

$$w = w - \eta \cdot \frac{\partial L}{\partial w}$$

where η is the learning rate, controlling the adjustment size at each iteration. This iterative optimization, often using Stochastic Gradient Descent (SGD), refines the weights and biases until convergence.

In the GIS software, we applied the ANN MLP with the default values of the parameters: a) Number of hidden layers (1); b) Learning Rate (η) (0.2000); c) Momentum (0.9000) and d) Number of iterations/epochs (1000). The hidden layers determined the capacity of the network to model complex patterns, while the learning rate and momentum determined the speed and stability of the training. The number of iterations determined how long the model was trained. Together, these settings directly drove the stability of the training, the speed of convergence and the accuracy of the classification.

4.7.5 ACCUARCY ASSESSMENT OF THE CLASSIFICATION

Evaluation of land cover categorization precision is critical for identifying and quantifying mapping errors. This evaluation usually entails creating an error matrix, which compares the map's details against reference data across sample regions (Congalton & Green, 2009).

Table 10 explains an error matrix example that outlines the classification of land cover (Congedo, n.d.).

	Reference 1	Reference 2	...	Reference k	Total
Class 1	a_{11}	a_{11}	...	a_{1k}	a_{1+}
Class 1	a_{11}	a_{11}	...	a_{1k}	a_{2+}
...	...	...	...	...	...
Class 1	a_{k1}	a_{k2}	...	a_{kk}	a_{k+}
Total	a_{+1}	a_{+1}	...	a_{+k}	n

Table 10. Example of a schematic confusion matrix for the accuracy assessment of land cover/land use classes. Adapted from "Accuracy," in Semi-Automatic Classification Plugin documentation (Congedo, n.d.).

The variable k represents the number of classified categories, whereas n represents the total number of gathered sample entities. The items on the primary diagonal (aii) represent the number of examples that have been correctly categorised, whereas the remaining elements show the number of instances that have been misclassified. By examining the error matrix (Congalton & Green, 2009), accuracy measures such as the commission error, the omission error, the OA, UA, PA, and the KC could be generated. The total accuracy can be determined by comparing the count of accurately classified samples (total of the primary diagonal) to the aggregate the number of samples, denoted as 'n' (Congalton & Green, 2009).

The OA which is also represented as a percentage, is defined as:

$$O = \frac{\sum_{i=1}^{k} a_{ii}}{n}$$

The UA for each class is determined by calculating the ratio accurate samples to the total number of samples in that class:

$$U_i = \frac{a_{ii}}{a_{i+}}$$

The commission error refers to pixels that are categorised as class i but really belong to a different class:

$$CE_i = 1 - U_i$$

The PA for each class is computed by dividing the number of accurate samples by the total number of samples in the column:

$$P_i = \frac{a_{ii}}{a_{+i}}$$

The omission error refers to the misclassification of pixels that really belong to class i as a different class:

$$OE_i = 1 - P_i$$

4.7.5.1 Kappa Coefficinet

The agreement between categorical variables X and Y is measured by Cohen's Kappa statistic, or K. Kappa, for instance, may be used to examine how well various raters are able to arrange subjects into several categories (Pennsylvania State University, n.d.). The KC is a statistical measure of land cover classification accuracy, quantifying the agreement between the classified data and ground truth. A Kappa value of 1 implies complete

agreement, whereas 0 or less shows random chance agreement. The KC (also known as the K or Khat statistic) is computed using an error matrix (also known as a confusion matrix) in the general form (Sim & Wright, 2005) :

$$\kappa = \frac{P_o - P_c}{1 - P_c}$$

Where:
P_o indicates the actual agreement ratio;
P_c represents the expected chance agreement ratio.

4.8 LAND COVER AND LAND USE CHANGE DETECTION

The ability of remote sensing to record and store images of land cover over time has enabled the detection of changes and the analysis of digital imagery (Lillesand et al., 2015). Detecting and mapping could be done using different methods. Post-classification change detection is one of the widely used methods and is therefore applied in this study.

4.8.1 POST-CLASSIFICATION CHANGE DETECTION

This method relies on pre-classified images from two different dates, with changes detected and mapped by comparing the pixels of co-registered images between the first and second dates (Singh, 1989). The result is a transitional matrix and map change of land cover and use classes, which tells the spatio-temporal dynamics among them over time. Based on the transition matrix, LCLU change can be further quantified, including the most changed classes (gains or losses) and dominant transitions (e.g., agriculture to transitional land). The most common indicator is the Annual Rate of Change (ARC) for each LCLU category expressed by this equation (Muhammad et al., 2021):

$$\text{ARC}(\%) = \frac{Fy - Iy}{Iy * t} * 100$$

Where: ARC is the annual rate of changes in each lclu classes Iy is the initial year, Fy is the final year and t, represents the time interval beaten classifications.

4.9 LAND COVER AND LAND USE CHANGE MODELING

The modeling and prediction of LCLU are based on temporal classification data, together with spatial indicators and variables, respectively. To achieve this goal, the CA-ANN method was applied in our study. The following sections present the processing steps.

4.9.1 TRANSITION POTENTIAL MODELING AND VALIDATION

To predict the transitional probability of LCLU class changes, the model requires as input periodic classification layers (2001, 2009, and 2019). These are used together with spatial variables such as DEM, proximity to lakes, rivers, roads, and settlements, as well as slope, as shown in Figure 20.

A MLP type of ANN is used for prediction, and its architecture and algorithm are discussed in Section ***3.5.1.4 Neural Network algorithms***. To train the model, different steps and parameters were tested in advance, and the following were selected as appropriate: sampling method (random), sample size (62,000); and for the hyperparameters: neighborhood (1 px), learning rate (0.001), maximum iterations (100), hidden layers (16), and momentum (0.001). With these parameters of the trained model, the potential transition model validation metrics yielded the following results: difference (Δ) in OA (–0.00001), minimum validation overall error (0.02088), and current validation kappa (0.70609). This temporal transition potential model was then used to simulate LCLU for 2019 and 2029.

4.9.2 SIMULATION AND VALIDATION OF THE MODEL

A CA is a grid of cells whose state changes with time depending on guidelines drawn from the state of every cell and its neighbours. Transition probability maps from the ANN allow the CA model to simulate the geographic patterns of land use change over time. Every cell has a specified neighbourhood that shapes its state at the following time step: Moore or Von Neumann neighbourhood (NextGIS, 2025) The algorithm uses a Moore neighborhood as the sampling procedure. In this case, a neighborhood size of 1 (3×3 window) is used as a parameter.

4.9.3 VALIDATION OF SIMULATIONS

The MOLUSCE (NextGIS, 2025) validation module evaluates the precision and dependability of simulations related to land use and cover change. Three fundamental categories of validation are imperative: Kappa Statistics, Error Budget Validation, and Error Map Validation. The Kappa statistic quantifies the degree of agreement between categorical datasets by comparing observed outcomes with expected results. Error budget validation systematically identifies and quantifies errors inherent in the simulation, categorizing them as input data errors or model errors. Error map validation produces visual representations of discrepancies between simulated and actual land use and cover, facilitating model refinement and the assessment of simulation accuracy.

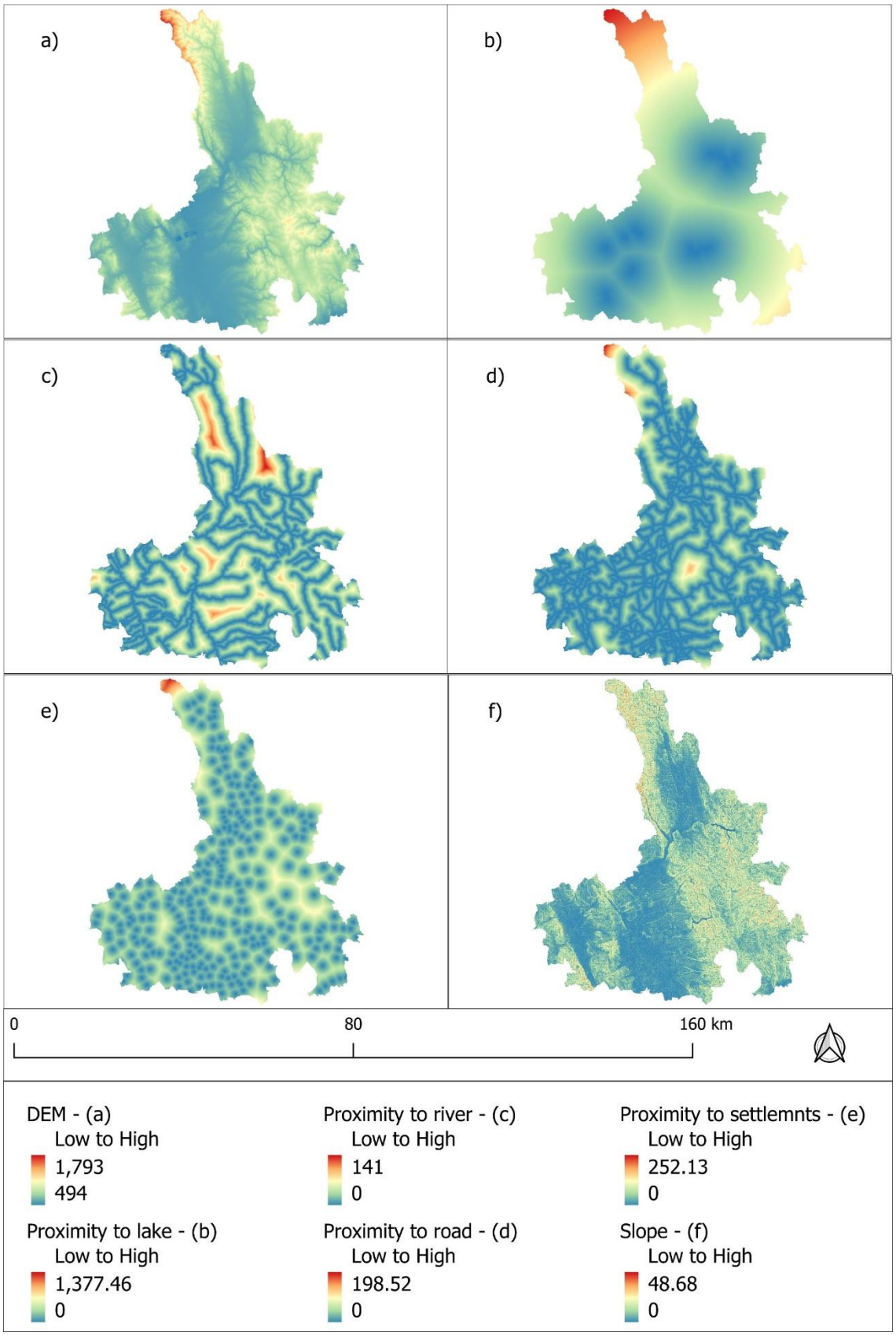

Figure 21. Spatial variables used as driving factors: a) DEM, b) Proximity to lakes, c) Proximity to rivers, d) Proximity to roads, e) Proximity to settlements, f) Slope.

5. RESULTS AND DISCUSSION

In this section, the classification map results for the three time periods (2001, 2009, and 2019) are presented using four classifiers: MD, ML, SVM-RBF, and NN. Next, we present the accuracy map evaluation results based on the error matrix and accuracy metrics. This allows us to find the classifier that did the best job of LCLU classification in the series. Subsequently, we analyze the spatial and temporal variations in LCLU. Finally, we use the spatial variables together with the LCLU classification time series to model and predict future changes in the study area.

5.1 LAND COVER AND LAND USE (LCLU) CLASSFICATION

For the three time periods, 2001, 2009, and 2019, a total of sixteen land cover and use classification maps were generated, applying the MD, ML, SVM RBF, and NN classifiers. Figures 22, 23, and 24 present the generated LCLU maps for 2001, 2009 and 2019. The map interpretation indicates that the classifiers differed in their performance when identifying and classifying LCLU types. On the maps that the MD and ML classifiers labeled, forest areas were overestimated due to the their poor classification performance and missclassified other vegeted areas as forest. On the other hand, the SVMRBF and NN classifiers were better at accurately limiting forest areas than the other classes. In general, if we look at the classification map for each classifier over time, all classifiers show a decreasing trend in forest areas. The agricultural class appears very fragmented in the maps of the MD and ML classifiers, mixed with the grassland and transitional land classes. These class boundaries are well-defined in the SVMRBF and NN classifier maps. The more accurate classification allows for a more reliable analysis of change trends. For instance, urban growth has led to a decrease in agricultural areas between 2001 and 2019. The urban class looks bigger and has fewer clear edges on the maps made by the MD and ML classifiers, while the industrial class is mixed up with the urban and bare-soil classes.

Meanwhile, in the SVMRBF and NN classifiers, the boundaries of these two classes are quite distinct. The grassland class is more distinctly classified by the Machine Learning classifier than by the two traditional classifiers. Generally, the presence of vegetation in the multi-temporal image series misclassifies this class with the agricultural and transitional classes. The MD and ML classifiers tend to overestimate the bare soil class more than the SVMRBF and NN classifiers do.

The spectral properties of the bare soil class were more effectively captured by the MD classifier, and as a result, it was largely classified as this class. The transitional land class is spectrally complex, encompassing processes such as deforestation, reforestation, burning, and desertification; consequently, it is difficult to classify with precise boundaries across all classifiers. However, the SVMRBF and NN classifiers have managed to define the boundaries of this class with precision.

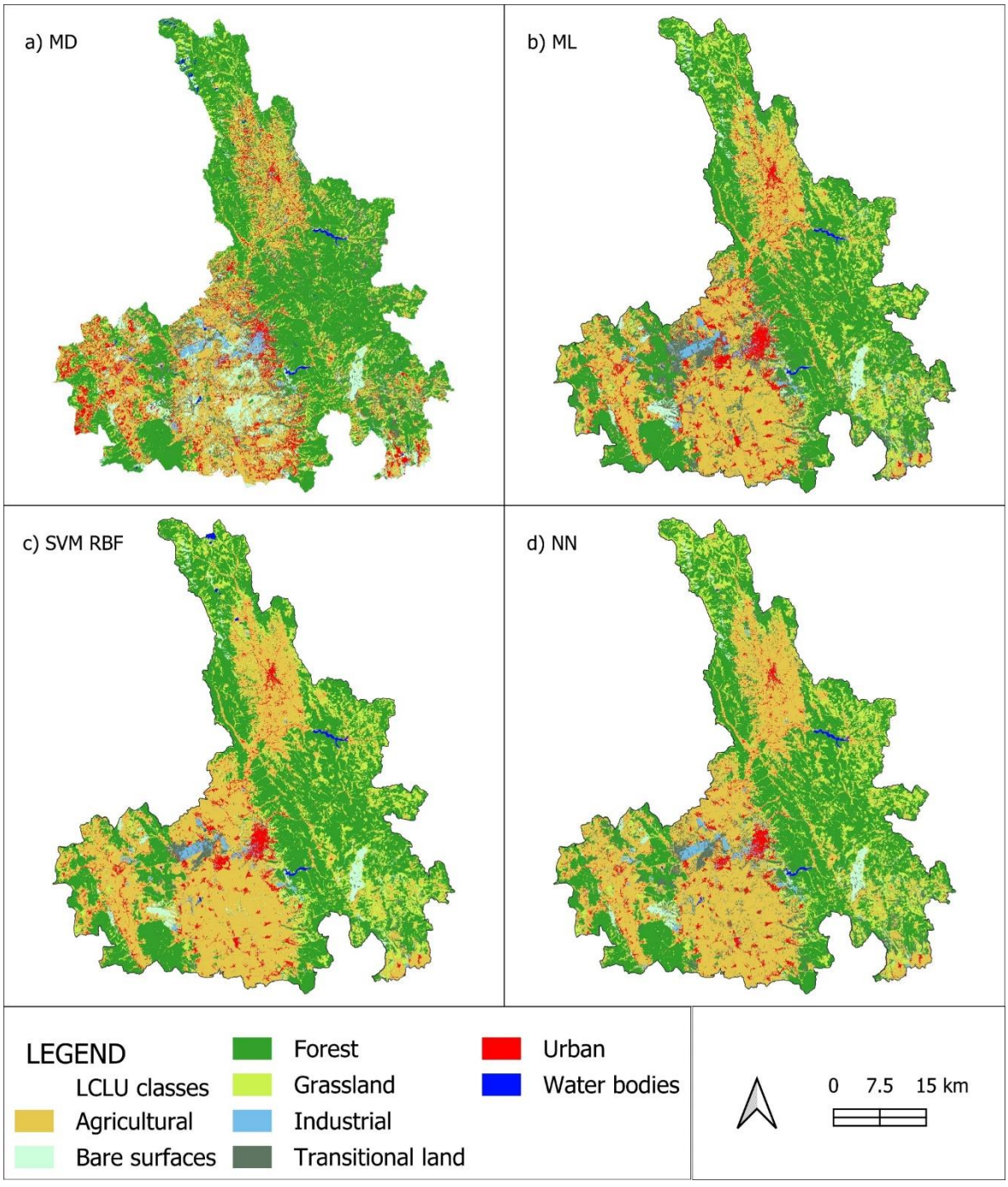

Figure 22. LCLU classification for 2001 using: a) MD, b) ML, c) SVM–RBF, d) NN.

Meanwhile, the water bodies class is particularly accurate in distinction and classification in all classifiers due to its spectral distinction from all classes. To verify and understand which of the four classifiers for a given year has achieved the highest accuracy in classifying LCLU, tabular data will be statistically analysed through the accuracy assessment process.

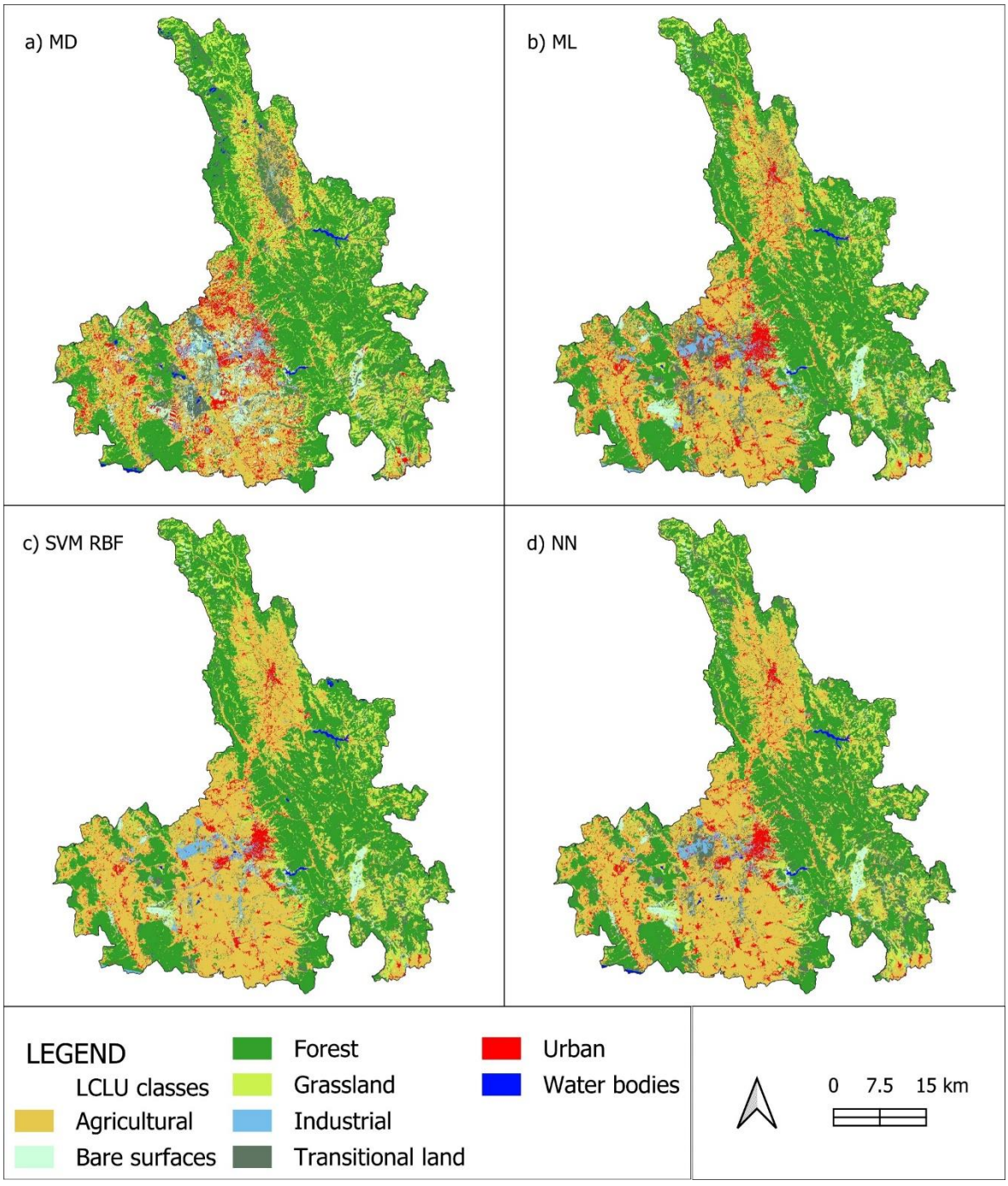

Figure 23. LCLU classification for 2009 using: a) MD, b) ML, c) SVM–RBF, d) NN.

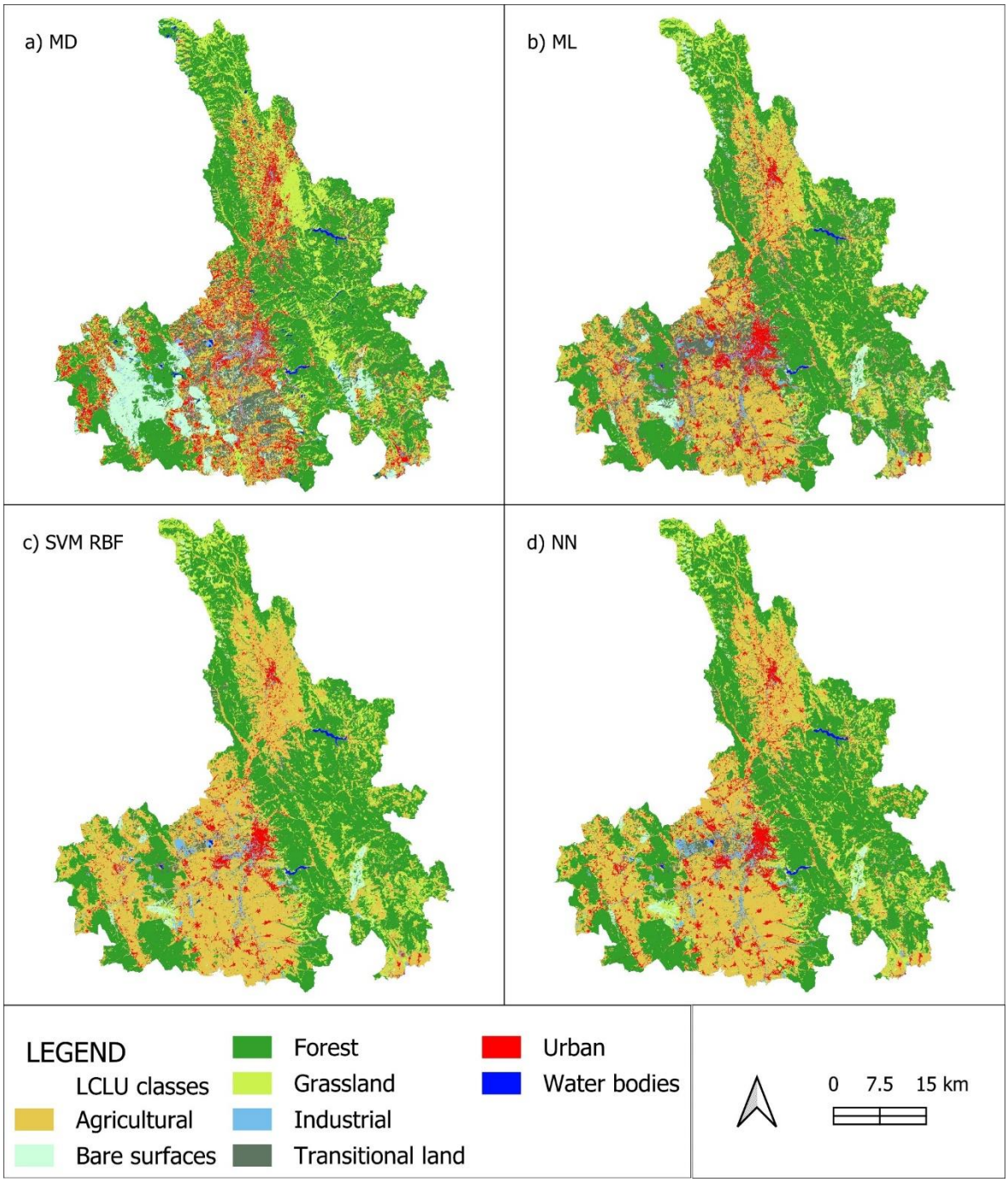

Figure 24. LCLU classification for 2019 using: a) MD, b) ML, c) SVM–RBF, d) NN.

5.2 Accuracy assessment of the classifications

We used the matrix table to check how well the MD, ML, SVM, RBF, and NN algorithms classified the area of interest over three different time periods: 2001, 2009, and 2019. Accuracy metrics like UA, PA, OA, KC, are used to compare the performance of a classification algorithm to the reference data. The matrix is used to perform this analysis, and they are presented through tabels in the Appendices section, from A1 to A12.

5.2.1 ACCURACY ASSESSMENT OF THE CLASSIFICATIONS FOR THE YEAR 2001

The initial step in assessing the accuracy evaluation of the four classifiers for the year 2001 was to examine the matrix error table for each classifier in the LCLU type. We have generated accuracy metrics based on the matrix tables, which demonstrate the performance of each classifier. Table 11 shows the metrics, such as UA, PA, OA, KC.

2001								
Alg	MD		ML		SVM RBF		NN	
LCLU	PA (%)	UA (%)	PA (%)	UA (%)	PA (%)	UA (%)	PA (%)	UA (%)
Ag	46.32	85.29	84.38	93.63	93.17	87.38	78.63	89.85
BS	73.83	31.3	83.36	76.53	75.34	81.64	65.54	69.36
Fo	94.4	76.13	95.21	95.63	96.71	89.26	49.29	46.41
Gr	34.58	38.48	66.57	66.57	68.81	71.30	100	95.58
In	66.14	57.44	71.71	56.69	67.73	66.15	71.91	64.01
TL	32.34	22.08	60.59	44.14	32.49	64.43	92.1	88.35
Ur	56.3	43.79	84.03	83.33	77.07	85.49	95.28	93.97
WB	97.22	86.42	96.3	100	99.54	95.98	62.48	79.88
OA (%)	59.82		82.44		84.00		83.00	
KC	0.50		0.78		0.79		0.78	

Table 11. Accuracy assessment metrics for 2001 (OA, PA, UA, Kappa, MD, ML, SVM-RBF, NN).

The accuracy measures such as UA, PA, OA, KC, were examined in Table 11 for the year 2001 for the four classifiers. The MD classifier had the lowest total accuracy (59.82%). Reaching 82.44%, ML showed notable gains, while SVMRBF showed the best OA (84.00%) and KC (0.79). On the other side, the NN classifier raised questions as it showed a significant misclassification in agriculture. Further offering insights, Table 11 shows PA and UA. SVM-RBF most frequently and accurately classified agriculture (93.17%) and forest (96.71%), having the greatest PA for both. Due to overfitting, the NN classifier had the greatest PA for grassland (100%). Indicating it generally predicted these classes, the ML classifier had high UA for Agriculture (93.63%) and Bare Soil (76.53%). With the best OA (84.00%), KC (0.79), and high PA/UA values for agriculture and forests, SVMRBF excelled generally. Close behind and displaying notable performance gains was the ML classifier. The NN classifier battled low distinction in features and overfitting in the transitional land class. In

conclusion, the SVMRBF had the most constant changes over the classification and was thus the most successful for LCLU categorisation.

5.2.2 ACCURACY ASSESSMENT OF THE CLASSIFICATIONS FOR THE YEAR 2009

Regarding the performance of the classifiers for LCLU classification in 2009, the error matrix is analyzed for one representative example of each classifier. Table 12 showed that the MD classifier had the greatest misclassification rates, particularly in the agricultural, bare soil, and grassland classes. The evaluation of the performance of the classifiers based on the accuracy metrics is shown in Table 12.

2009								
Alg	MD		ML		SVM RBF		NN	
LCLU	PA (%)	UA (%)	PA (%)	UA (%)	PA (%)	UA (%)	PA (%)	UA (%)
Ag	34.01	79.02	90.2	93.42	91.67	82.93	96.02	86.53
BS	48.93	22.13	92.5	65.82	79.64	77.03	92.14	82.83
Fo	88.76	82.72	96.48	92.87	97.04	90.82	93.21	96.20
Gr	53.00	36.65	71.12	76.44	71.66	76.43	74.87	81.24
In	75.28	63.82	85.51	81.78	86.46	87.98	79.53	90.99
TL	34.42	23.9	57.88	57.33	35.1	61.34	55.29	73.81
Ur	48.54	37.88	87.26	90.89	84.26	89.56	88.93	90.97
WB	95.51	59.03	88.76	100.00	99.44	100.00	99.44	100.00
OA (%)	51.17		85.00		83.24		87.21	
KC	0.42		0.81		0.78		0.83	

Table 12. Accuracy assessment metrics for 2009 (OA, PA, UA, Kappa, MD, ML, SVM-RBF, NN).

With an OA of 51.17% and a KC of 0.42, the MD classifier performed poorly and misclassified many types of LCLU. With a PA of only 34.01% for agriculture, notable underclassification occurred. Water bodies exhibited relatively high accuracy, whereas other classes—particularly grassland (Gr) and TL—experienced significant misclassification.

The ML classifier did much better than MD, with an OA of 85.00% and a KC of 0.81. It also showed a lot more agreement between the classified data and the reference data. ML is very

dependable in the areas of agriculture and water bodies because it demonstrated clear advances in them.

Despite this, there are still misclassification issues with transitional land (PA = 57.88%) and industrial land (PA = 85.51%). With an OA of 83.24% and a KC of 0.78, the SVM-RBF classifier also did really well. It performed very well in classifying forests and water bodies, with few misclassifications. Transitional land (PA = 35.10%) remained the lowest class, nonetheless, suggesting that many real TL pixels were misclassified into other groups. With an OA of 87.21% and a high KC of 0.83, the neural network classifier was the most successful, showing great classification dependability. It worked well for classifications of water bodies and forest categories as well as agriculture and urban classes. Transitional Land, meanwhile, had classification problems, somewhat better than ML and SVM-RBF.

Generally speaking, NN was the most accurate and dependable classifier; ML came second, while SVM-RBF also showed excellent performance. The least dependable model is MD, as it performed poorly across all land cover categories.

5.2.3 ACCURACY ASSESSMENT OF THE CLASSIFICATIONS FOR THE YEAR 2019

The accuracy assessment of the classification for the year 2019 was analysed in the same way as in the two previous time series. Based on the confusion matrix presented in Table 13, the MD classifier continued to perform poorly in the 2019 period as well, beginning with the misclassified agriculture class.

Based on evaluation accuracy metrics for LCLU classification for 2019, shown in Table 13, the MD classifier performed poorly, with an OA of 48.00% and a KC of 0.39. This indicates that misclassification was quite common, especially amongst transitional land, grassland, and agriculture classes.

2019								
Alg	MD		ML		SVM RBF		NN	
LCLU	PA (%)	UA (%)	PA (%)	UA (%)	PA (%)	UA (%)	PA (%)	UA (%)
Ag	24.02	70.46	83.4	93.45	89.13	84.33	87.00	89.99
BS	41.81	24.64	88.65	85.02	71.87	91.31	63.87	92.52
Fo	86.53	85.59	91.32	92.82	93.88	90.47	94.46	90.18

Gr	50.56	29.45	65.37	62.71	68.08	64.62	74.41	59.18
In	46.85	48.08	58.43	56.05	62.69	59.26	59.8	56.61
TL	28.75	15.03	49.39	34.00	21.1	37.20	33.18	50.12
Ur	63.88	39.02	88.26	79.05	85.29	86.80	90.41	84.94
WB	97.00	100.00	92.00	100.00	99.00	100.00	97.5	91.55
OA (%)	48.00		81.00		81.30		81.86	
KC	0.39		0.76		0.76		0.77	

Table 13. Accuracy assessment metrics for 2019 (OA, PA, UA, Kappa, MD, ML, SVM-RBF, NN).

In contrast, the ML classifier achieved a KC of 0.76 and an OA of 81.00%, thereby improving classification performance compared to MD. In agriculture (PA = 83.4%) and water bodies (PA = 92.00%), it had a really good accuracy. Still, misclassification remained a challenge in transitional land and grassland classes. While SVM-RBF did about as well as ML at classifying agriculture and forests (OA = 81.30%, KC = 0.76), it did much better at classifying water bodies (PA = 99.00%) and bare soil (71.87%).

With an OA of 81.86% and a KC of 0.77, NN was the most successful classifier, minimizing misclassification errors and maximizing accuracy for agriculture, urban areas, and water bodies. While transitional land still presented difficulties for all classifiers, NN constantly showed better general classification accuracy. With the highest classification accuracy, NN is overall the most suitable model for LCLU classification in 2019.

5.3 LCLU CLASSIFICATION AND CHANGE DETECTION

The LCLU classification maps for the time series were chosen after the classifiers' accuracy was judged by their highest values for items like the KC and OA. For the year 2001, the classification map performed by the SVM RBF was selected (Figure 22 c), while for the years 2009 (Figure 23 d) and 2019 (Figure 24 d), the maps from the NN classifier were selected based on classification performance. Based on the results of the matrix table and the post-classification method for detecting LCLU changes, spatial statistics were calculated for the periods 2001, 2009, and 2019.

5.3.1 SPATIO–TEMPORAL DYNAMICS ANALYSIS OF LCLU CHANGE

The area (in km² and %) statistics of LCLU classes over the study period from 2001 to 2019 are presented in Table 14 and Figure 24 as well. Whereas the magnitude of changes in ha and percentage, as well as annual growth, are presented in Table 15 and Figure 28.

LCLU classes	2001		2009		2019	
	Area (km^2)	%	Area (km^2)	%	Area (km^2)	%
Water bodies	7.16	0.31	6.81	0.30	5.51	0.24
Urban	92.37	4.05	105.04	4.61	140.08	6.14
Transitional land	47.52	2.08	238.74	10.47	95.79	4.20
Industrial	29.07	1.27	34.11	1.50	53.22	2.33
Grassland	326.71	14.32	273.13	11.98	316.42	13.87
Forest	921.67	40.41	786.33	34.48	940.63	41.24
Bare surfaces	46.61	2.04	47.98	2.10	30.72	1.35
Agricultural	809.70	35.50	788.70	34.58	698.45	30.62
Total	2280.81	100.00	2280.84	100.00	2280.82	100.00

Table 14. Distribution of land cover/land use (LCLU) classes, 2001–2019 (km² and %)

The agricultural class experienced continuous shrinkage throughout the study period. Between 2001 and 2019, it decreased by 21.01 km², corresponding to an annual decline of 0.92%. The loss of agricultural land continued at an even greater rate in the period of 2009–2019, with about -90.25 km² or -3.96% annual decrease. This large shrinkage of the agricultural class, especially in the second period, indicates the urban, industrial, and infrastructural expansion towards this class. In the entire period 2001-2019, the agricultural class lost -111.25 km² or -4.88% annually, a value that indicates that this class is more vulnerable and has suffered the greatest shrinkage or transformation.

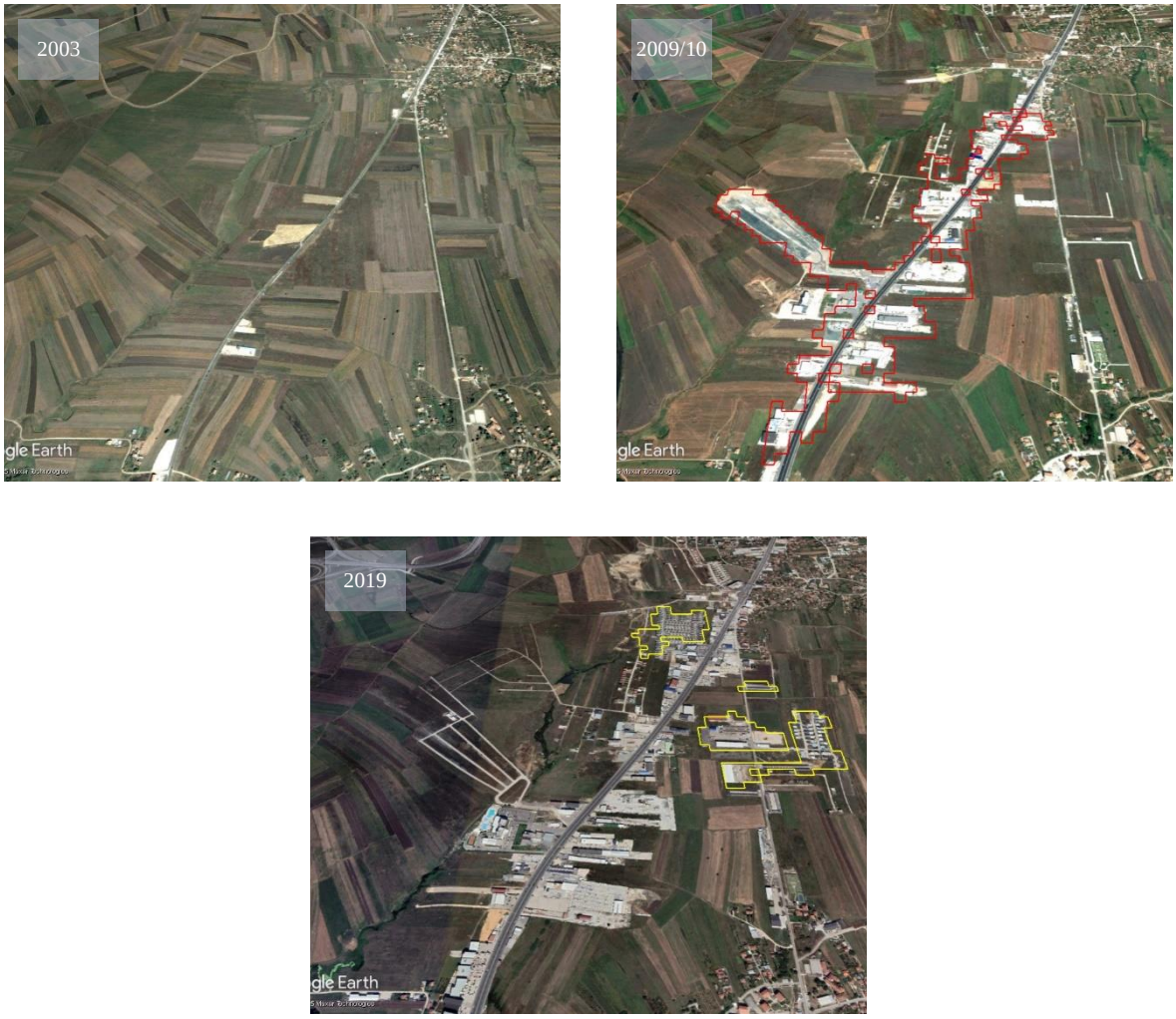

Figure 25. Agricultural land shrinkage due to industrial and urban expansion.

The **bare surfaces** class shows an increase of +1.36 km² or +0.06% annual growth for the first period 2001–2009, which can be related to the new vegetative growth. However, during the second period 2009–2019, it decreases significantly by -17.25 km² or -0.76% annually. While in the entire period 2001–2019, it experiences an annual decrease of -15.89 km² or -0.70%, which shows that this class is undergoing changes as a result of demands for agricultural production, infrastructure, etc.

The **forest** class experienced a large decrease during the period 2001–2009, with –135.34 km², or –5.93% annual decrease, which indicates the occurrence of illegal logging of forests, the increase in agricultural areas, and their burning. On the other hand, in the second period, it marks a large increase in reforestation with a +154.30 km² or 6.77% annual increase. This large increase is related to the regeneration of natural vegetation of burnt areas,

then the abandonment of villages, and artificial reforestation. If we analyse the entire time period of 2001–2019, the forest class shows an increase of 18.95 km² or 0.83% annual increase. However, the dramatic decrease during the first period (Figure 26.) suggests that forests are in constant danger from anthropogenic factors.

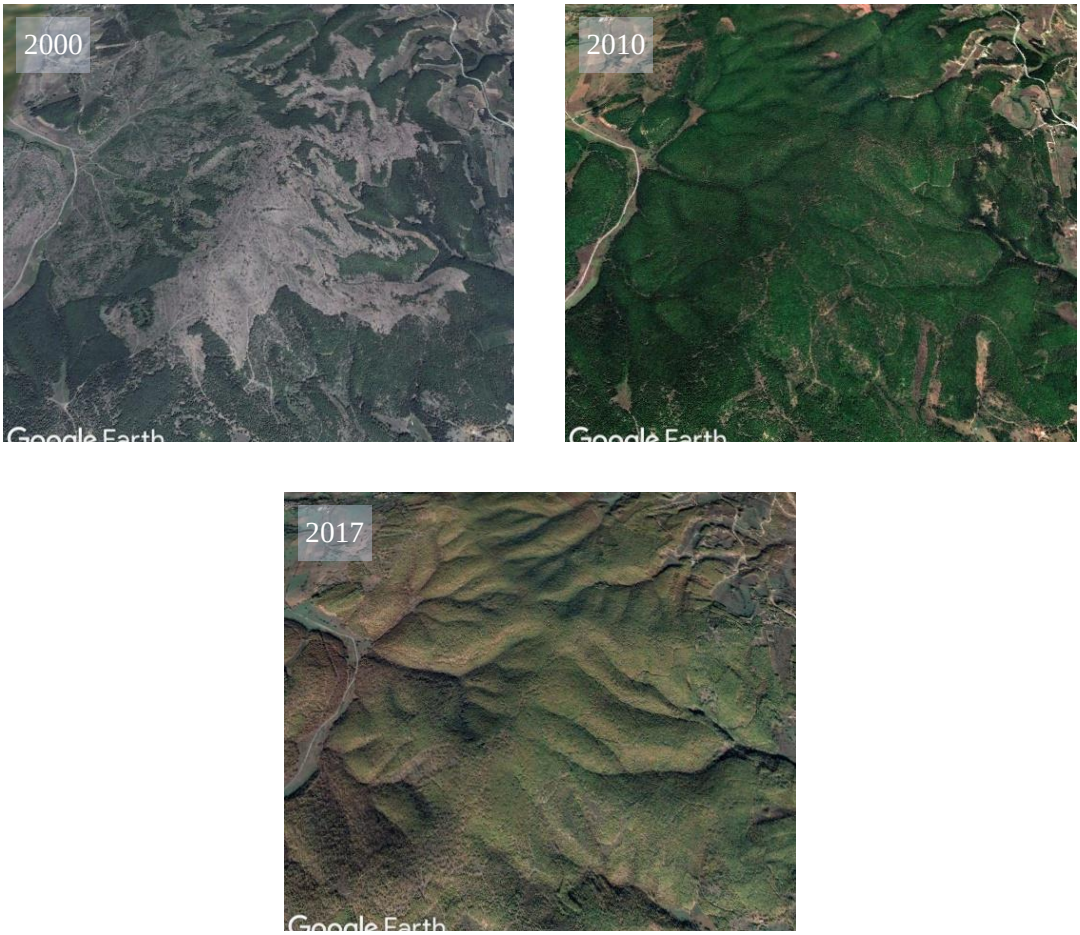

Figure 26. Forest cover gains and losses during 2000–2017.

Grassland class experienced a significant decrease during the first period, 2001-2009, with a -53.58 km² or -2.35% annual decrease, which may be as a result of the return of this class to working lands, the expansion of settlements, or industry. Whereas, in the second period, 2009-2019, it marks an increase of +43.29 km² or a 1.90% annual increase, which may be related to the abandonment of lands or conservation. In the entire period 2001-2019, this class has suffered losses of about -10.29 km² or -0.45% annually, which indicates a trend of its decrease.

The industrial class experienced continuous growth during the study period. Between 2001 and 2009, it increased by 5.04 km², corresponding to an annual growth rate of 0.22%,

followed by even greater growth between 2009 and 2019, with an increase of 19.12 km², or 0.84% per year. This large increase in the industrial class is associated with economic development, the establishment of production areas and commercial activities, mainly with an expansion near urban areas, and new transport routes, which primarily touch the agricultural and grassland areas. With an increase of 24.16 km² or 1.06% annual growth, during the entire period 2001-2019, it shows the trend of growth of industrial capacities in the country.

Transitional land class shows a rapid increase in the first period, 2001–2009, with about 191.22 km² or 8.38% annual growth, which indicates that land degradation is quite widespread and is mainly related to deforestation and agricultural land use. Both of these classes have contributed the most to their growth. In contrast to the first period, during 2009–2019, this class experienced a contraction of 142.95 km², corresponding to an annual decrease of 6.27%, largely due to forest regeneration as well as the expansion of urban and industrial areas. Whereas, during the entire period of 2001-2019, with an increase of +48.27 km^2 or +2.12%, it shows a positive growth trend of this class, which is related to degradation, restoration, or temporal transition between classes.

The **urban** class has grown significantly in the first period, 2001–2009, with about +12.66 km² or 0.56% annual growth, tripling its growth in the second period, 2001–2009, with +35.04 km² or +1.54% annual growth. Meanwhile, during the entire 18-year period, there is an increase of + 47.71 km² or 2.09% annual growth, which shows a trend of growth of the urban class as a result of the urbanisation process, the development of road infrastructure, and the migration of the population to cities. The spatial spread of the urban class mostly affects the agricultural class, the transitional class, and the pastures.

Figure 27. Urban expansion of Prishtina, 2001–2019.

Water bodies. During the period 2001-2009, the area of water bodies has suffered a contraction of -0.35 km² or -0.02% of annual contraction, continuing with an even greater contraction in the second period 2001-2019 with an area of -1.30 km² or -0.06% annual. In the entire period 2001-2019, water surfaces show a trend in their reduction by about -1.65 km² or -0.07% annually. This contraction can be attributed to climatic factors such as drought, as well as to the composite of multi-temporal images used during classification. In the study area, which includes two artificial lakes and several rivers, the reduction is spatially concentrated along the lake shores and riverbeds.

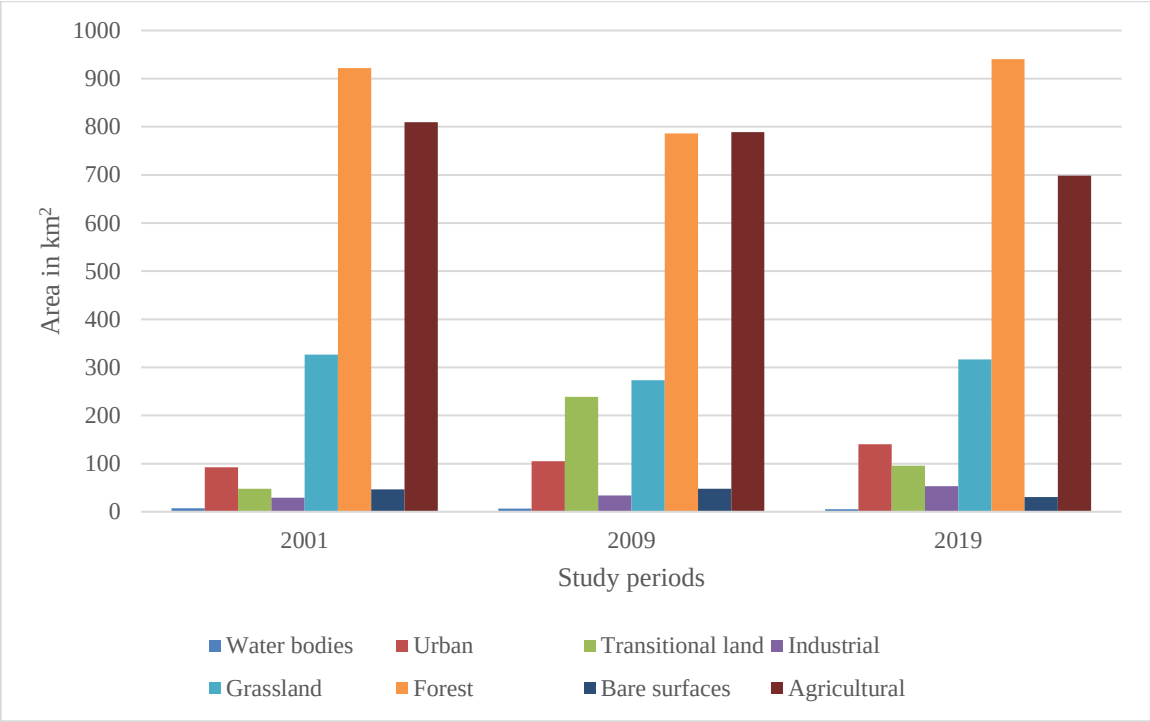

Figure 28. Distribution of LCLU, 2001–2019 (km²).

Whereas the magnitude of changes in ha and percentage, as well as annual growth, are presented in Table 15 and Figure 28.

	2001-2009		2009-2019			2001-2019
LCLU classes	Area (ha)	%	Area (ha)	%	Area (ha)	%
Water bodies	-0.35	-0.02	-1.30	-0.06	-1.65	-0.07
Urban	12.66	0.56	35.04	1.54	47.71	2.09
Transitional land	191.22	8.38	-142.95	-6.27	48.27	2.12
Industrial	5.04	0.22	19.12	0.84	24.16	1.06
Grassland	-53.58	-2.35	43.29	1.90	-10.29	-0.45
Forest	-135.34	-5.93	154.30	6.77	18.95	0.83
Bare surfaces	1.36	0.06	-17.25	-0.76	-15.89	-0.70
Agricultural	-21.01	-0.92	-90.25	-3.96	-111.25	-4.88

Table 15. Magnitude of LCLU change, 2001–2019 (ha and %)

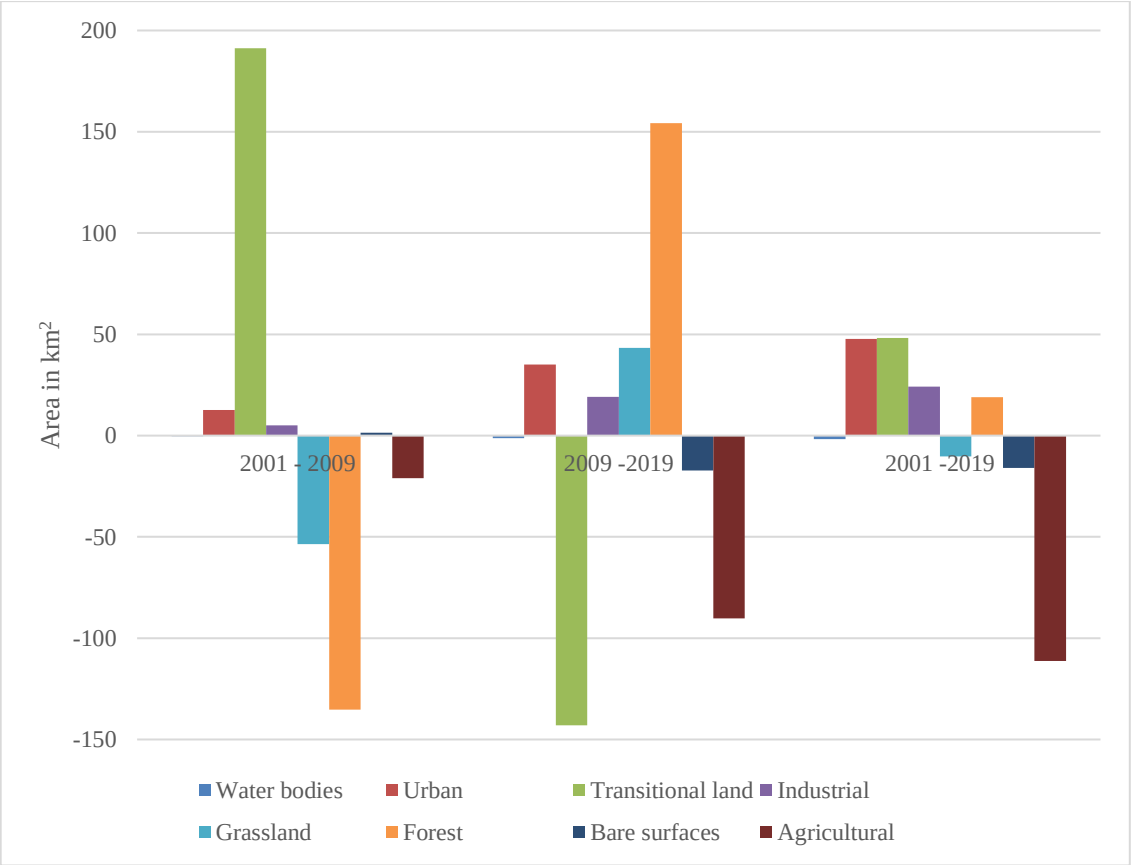

Figure 29. LCLU gains and losses (km²) for 2001–2009, 2009–2019, and 2001–2019.

5.3.2 LCLU TRANSITIONAL PROBABILITIES

To better understand the changes from one class to another that have occurred during the study period, the transitional probability matrix tables will be used.

Table 16 and Figure 31 present the transitional potential between classes for the period 2001–2009. The agricultural class exhibited a relatively high degree of persistence, with 82% remaining unchanged during 2001–2009, followed by a contraction to 74% in the second period, and an overall maintenance rate of 72% across the entire study period (2001–2019). The largest losses of agricultural area occurred to urban areas, transitional land, and grassland, indicating the conversion of agricultural land into urban land as well as abandonment, particularly near industrial and urban zones. The bare surfaces class undergoes frequent transformations within other categories, most notably the Grassland class. Its rate of no change in the period 2001-2009 was about 64%, in 2009-2019 with 45%, and 2001-2019 with about 44%. The forest class had a small decline and mainly a high degree of non-change. In the period 2001-2009, the rate was 82%, in 2009-2019 with 95%, and during the entire period 2001-2019 with 92%. Mainly, it was transformed into the

transitional land class and the grassland class, which is related to the deforestation process. The last two periods show a high degree of regeneration in areas that were deforested during the first period.

The grassland class had a dynamic fluctuation during the entire period. With a rate of non-change of 56% in 2001-2009, 58% in 2009-2019, and 52% in 2009-2019, its main transformation occurred in the forest, agricultural, and transitional land classes. The industrial class had an average stability of no change with 52% in 2001–2009, 51% in 2009–2019, and about 42% in the entire period 2001–2019. Most of it was transformed into urban, transitional land, and agricultural classes. The transformation in the last two classes (Figure 30) is directly related to the spaces and therefore after the exploitation of coal in mines and areas around thermal power plants.

Figure 30. Transformation of the open coal mine area, located in the municipality of Obiliq and FushëKosova (Left – 2010; Right – 2020)

The transitional land class represents the class with the highest rate of mutual transformation between categories and very low rates of non-change throughout the periods: by 36% in 2001–2009, by 11% in 2009–2019, and about 18% in 2001–2019. Its greatest loss occurred towards the Forestry and Agricultural classes, while it gained from the transformation from the Agricultural, Grassland, and Industrial classes. Throughout the period of change, the urban class maintained a high and constant degree of retention. The percentage of the urban class remained at 69% from 2001 to 2009, 73% from 2009 to 2019, and 72% for the entire period from 2009 to 2019. Its loss mainly goes to the agricultural class and, to a lesser extent, to the transitional land and industrial ones. On the other hand, the growth of the urban class occurred mainly on the back of the agricultural class. The water bodies class remained relatively stable, with persistence rates of approximately 60% in 2001–2009, 61% in 2009–

2019, and 57% over the entire study period (2001–2019). Most transitions occurred to the grassland and agricultural classes.

Based on the periodic LCLU transitional probability data, the agricultural class is decreasing, being converted into urban areas, transitional land, and grassland. The bare surfaces and grassland classes show instability throughout the study periods, undergoing continuous changes between the classes. The forest class showed stability in not changing; however, fluctuations with large losses and gains in surfaces were evident between the first two periods. Compared to all other classes, the transitional land class had relatively little stability, due to urban and industrial growth, deforestation, and the transitional change from one category to another. Throughout the study period, the urban and industrial classes experienced continuous growth, primarily due to the transformation of agricultural and transitional land. And finally, the class of water bodies was relatively stable throughout the study period.

LCLU classes		2009							
		Wb	Ur	Tl	In	Gr	Fo	Bs	Ag
2001	Wb	0.60	0.00	0.06	0.03	0.10	0.10	0.01	0.10
	Ur	0.00	0.69	0.02	0.04	0.01	0.00	0.01	0.23
	Tl	0.00	0.02	0.36	0.07	0.15	0.13	0.03	0.24
	In	0.01	0.17	0.06	0.52	0.03	0.00	0.07	0.14
	Gr	0.00	0.00	0.15	0.00	0.56	0.06	0.01	0.22
	Fo	0.00	0.00	0.13	0.00	0.03	0.82	0.00	0.01
	Bs	0.00	0.01	0.11	0.02	0.09	0.03	0.64	0.11
	Ag	0.00	0.04	0.05	0.01	0.06	0.00	0.01	0.82

Table 16. Transition probability matrix of LCLU classes, 2001–2009

LCLU classes		2019							
		Wb	Ur	Tl	In	Gr	Fo	Bs	Ag
2009	Wb	0.61	0.01	0.02	0.05	0.03	0.13	0.00	0.16
	Ur	0.00	0.73	0.01	0.07	0.03	0.01	0.00	0.15
	Tl	0.00	0.02	0.11	0.02	0.14	0.56	0.01	0.14
	In	0.01	0.13	0.14	0.51	0.05	0.00	0.02	0.13
	Gr	0.00	0.01	0.05	0.01	0.58	0.16	0.01	0.18
	Fo	0.00	0.00	0.02	0.00	0.02	0.95	0.00	0.01
	Bs	0.00	0.03	0.05	0.06	0.27	0.04	0.45	0.10
	Ag	0.00	0.06	0.04	0.02	0.12	0.02	0.00	0.74

Table 17. Transition probability matrix of LCLU classes, 2009–2019

LCLU classes		2019							
		Wb	Ur	Tl	In	Gr	Fo	Bs	Ag
2001	Wb	0.57	0.01	0.02	0.03	0.14	0.11	0.01	0.11
	Ur	0.00	0.72	0.02	0.07	0.03	0.01	0.00	0.15
	Tl	0.01	0.03	0.18	0.08	0.18	0.30	0.01	0.22
	In	0.01	0.13	0.15	0.42	0.10	0.00	0.04	0.15
	Gr	0.00	0.01	0.05	0.01	0.52	0.18	0.01	0.21
	Fo	0.00	0.00	0.03	0.00	0.03	0.92	0.00	0.01
	Bs	0.00	0.01	0.06	0.04	0.28	0.08	0.44	0.09
	Ag	0.00	0.07	0.04	0.03	0.11	0.02	0.01	0.72

Table 18. Transition probability matrix of LCLU classes, 2001–2019

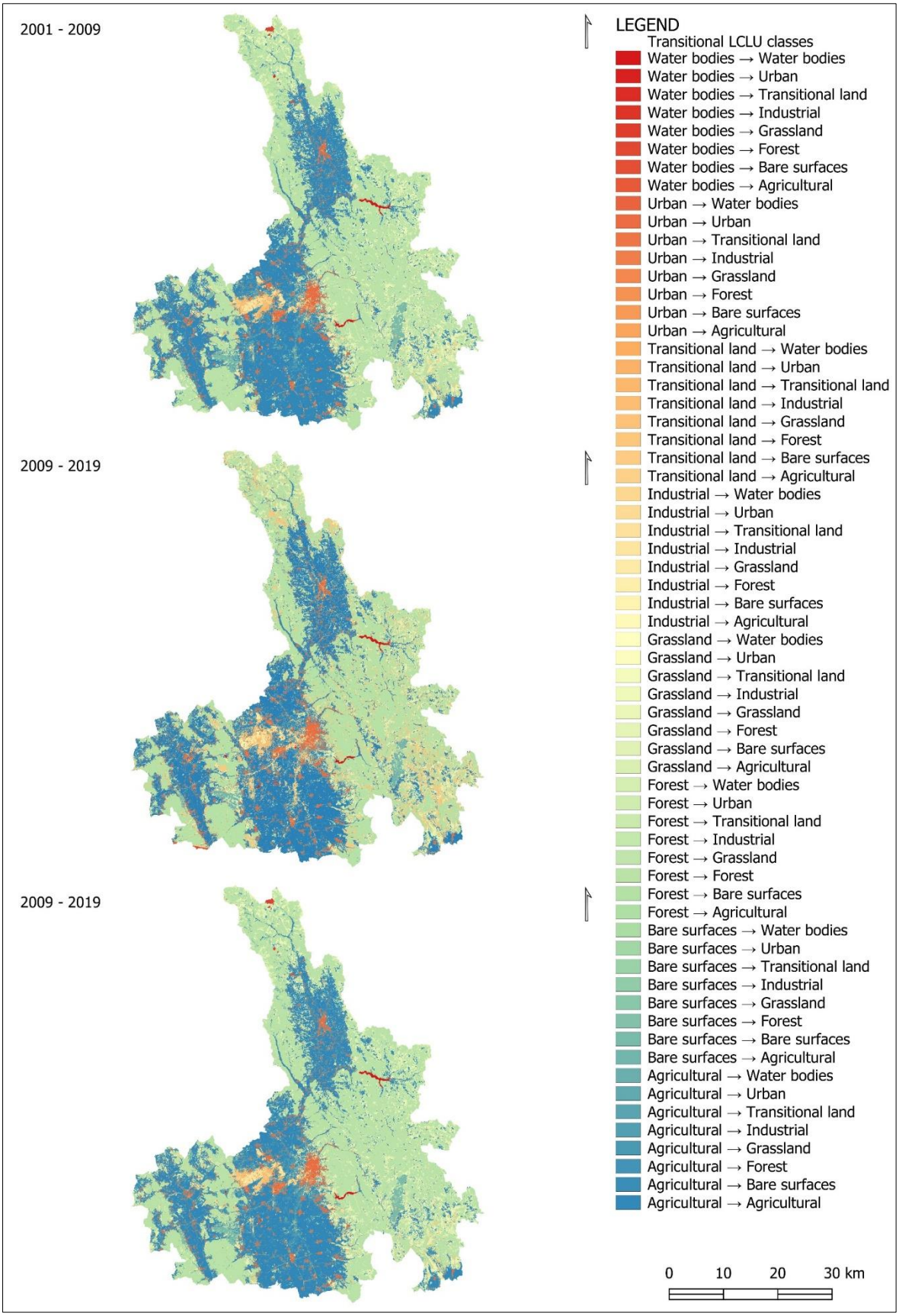

Figure 31. LCLU transition maps: a) 2001–2009, b) 2009–2019, c) 2001–2019.

5.4 LCLU CHANGE MODELLING AND PREDICTIONS

In this section, the results of the LCLU modelling and simulation for the study area will be discussed. The results of the modelling and simulation, carried out through the CA-ANN method, are also influenced by spatial variables, which are influential in the development or reduction of one of the LCLU classes for the study area. Below, the results of variable influence, the development of the transitional potential model, its simulation, and validation are discussed.

5.4.1 SPATIAL VARIABLES EVALUATION

To assess the correlation between spatial variables, the Pearson correlation coefficient was used, as the data incorporated in the model are continuous. Table 19 presents the correlation values among the spatial variables.

	DEM	Proximity to lakes	Proximity to river	Proximity to road	Proximity to settlements	Slope
DEM	--	0.50	0.06	0.54	0.50	0.54
Proximity to lakes		--	0.00	0.29	0.24	0.25
Proximity to river			--	0.10	0.05	0.03
Proximity to road				--	0.48	0.29
Proximity to settlemnts					--	0.29
Slope						--

Table 19. Pearson correlation coefficients among spatial variables

The DEM shows an average positive correlation with lakes and settlements, with a value of 0.50, and a slightly higher one with settlements, with a slope of 0.54. However, there is a very weak correlation with the proximity of rivers. Lakes have a very weak spatial correlation with rivers of 0.004. However, a weak correlation of lakes between the proximity of roads (0.29) and settlements (0.24) indicates human activities that can develop near them, such as tourism. The spatial variable representing rivers exhibits a very weak correlation with the others, suggesting that it may have minimal impact on LCLU changes. On the other hand, the variable roads have an average correlation of 0.49 with how close settlements are to each other. This means that the roads affect the size of settlements and are also the main

cause of changes in the LCLU classes. Also, the average DEM correlation of 0.54 and slope of 0.29 indicate that the roads are built on surfaces with lower altitudes and lower or suitable slopes. The variable settlements show the strongest correlation with the proximity of roads of 0.49 and relief of 0.50, which indicates that the settlements are located close to the roads and at lower, suitable altitudes. On the other hand, the weakest correlation of 0.29 with the slope suggests that the settlements are primarily situated on surfaces with low or medium slopes. Based on the Pearson correlation coefficient values, the only spatial variable that may have a minimal effect on LCLU changes is the river variable that was used to make the TPM.

5.4.2 LCLU CHANGE TRANSITION POTENTIAL MODELLING AND EVALUATION

The learning curve in Figure 31 shows the outcome of learning the MLP-ANN algorithm to create the transitional potential model. This lets us evaluate how well the model works. The x-axis represents the number of iterations, which in this case has a maximum of 100, while the y-axis shows the initial and final values of the mean square error. The learning curve is composed of the training (green) and validation (red) curves, which show that the initial learning phase—zero iterations, the errors drop down—around 20 iterations on both curves and shows the ability of the model to learn quickly from the training data.

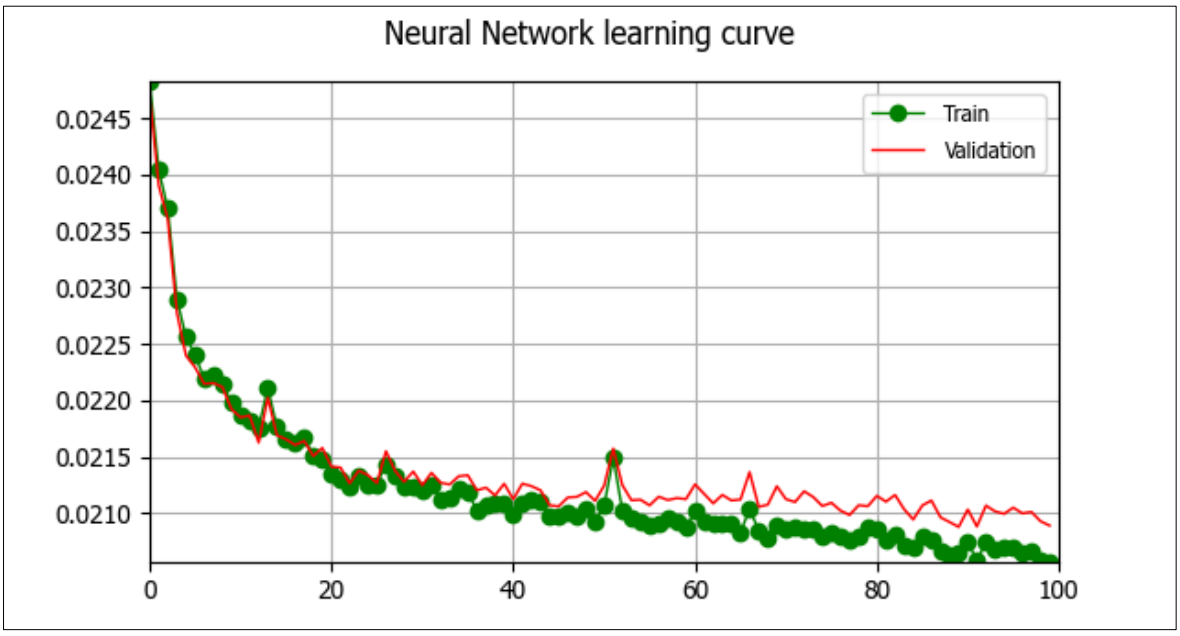

Figure 32. MLP-ANN learning curve.

Between iterations 20 and 60, both curves gradually decrease, with a more pronounced fluctuation in the validation loss curve indicating a stabilization phase. From iterations 60 to

100, on the other hand, the convergence phase starts. This means that the model has fully learned from the data, which means that training is stable and validity has been lost. Since both curves from the graph show a common decline with small fluctuations, it can be concluded that the model is well trained.

5.4.3 LCLU Simulation and Validation

We performed LCLU simulations for the periods 2019, 2029, and 2039 after training and validating the model. Figure 31 shows the simulated maps.

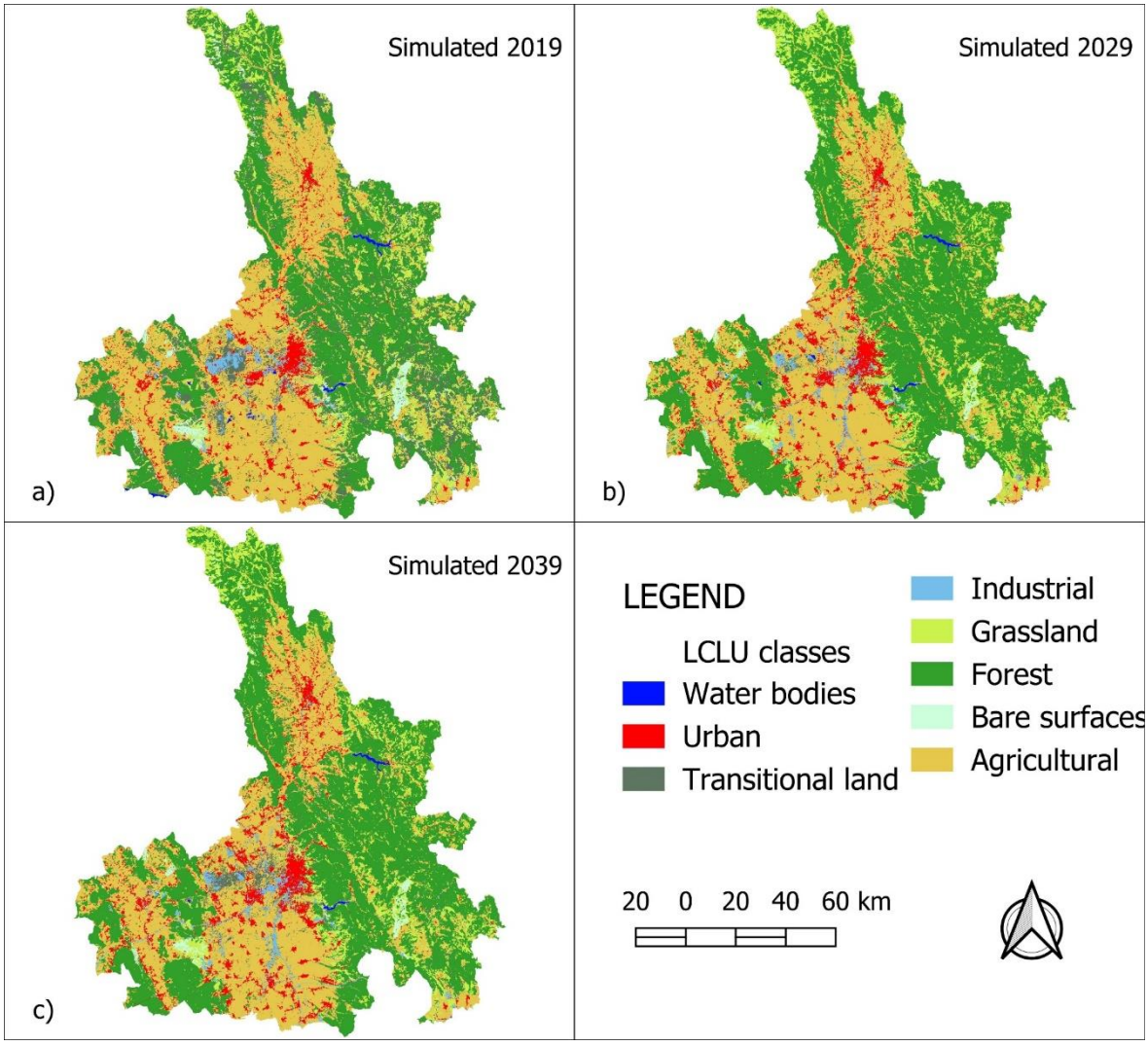

Figure 33. Simulated LCLU maps for 2019, 2029, and 2039.

To simulate the LCLU 2019 map, the model generated by using the LCLU 2001 and 2009 maps, as well as the spatial variables, was used. For the 2029 simulation, the LCLU 2009 and LCLU 2019 maps were used together with the variables, and for the 2039 simulation, the LCLU 2019 map and the simulated map 2029 were used.

5.4.4 VALIDATION OF THE SIMULATION

We compared and validated the simulated 2019 map from the previously generated model with the current LCLU 2019 map using KAPPA coefficients. The overall kappa (0.59) indicates an average agreement between the simulated and reference maps. The histogram reveals a relatively high compatibility between the values of kappa and the spatial distribution of the LCLU classes. The kappa location, with a value of 0.74, demonstrates a strong correlation, indicating that the model successfully predicts changes in LCLU classes. The Multiple-Resolution Budget (MRB) graph in Figure 33 also supports the validation assessment.

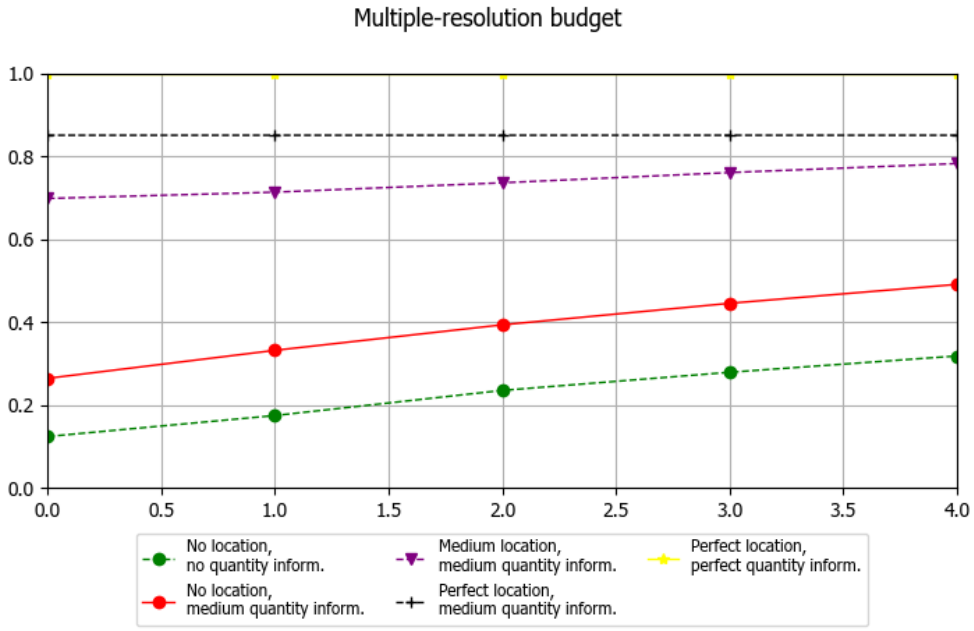

Figure 34. Validation of 2019 Simulated Map vs. Observed LCLU

The yellow line in the graph - perfect location, perfect quantity inform, with a value close to or 1.0, shows that the model has performed well, because both the quantitative and spatial accuracy are reaching their maximum. Below it, there is the black line—a perfect location, medium quantity of information with a high value of 0.85, which shows the impact of location accuracy on validation and seems to be in line with the location cap. On the other hand, the purple line—medium location, medium quantity of information—shows that the more accurate the spatial information is, the more accurate the model's prediction is. Although Multi - resolution budgets are rising, the red and green lines show a declining accuracy, indicating that a perfect amount of information is not enough to significantly

improve validation accuracy. The modest overall kappa of the model (0.59) points to some spatial differences; therefore, it stresses the need for accurate spatial data.

5.4.5 LCLU CHANGE PREDICTION

Table 20 presents the LCLU 2029 and 2039 prediction maps, as well as the LCLU 2019 actual map statistics area in kilometres and percentages. As the table shows, across the three periods—2019, 2029, and 2039—the agricultural and forest classes are predicted to predominate in the landscape of the study area.

	2019		2029		2039	
LCLU classes	Area (km^2)	%	Area (km^2)	%	Area (km^2)	%
Water bodies	5.51	0.24	4.9	0.21	4.12	0.18
Urban	140.08	6.14	148.43	6.51	160.71	7.05
Transitional land	95.79	4.2	8.48	0.37	69.23	3.04
Industrial	53.22	2.33	48.21	2.11	52.49	2.30
Grassland	316.42	13.87	266.6	11.69	253.6	11.12
Forest	940.63	41.24	1049.99	46.03	1006.15	44.11
Bare surfaces	30.72	1.35	15.41	0.68	19.9	0.87
Agricultural	698.45	30.62	738.88	32.39	714.71	31.33
Total	2280.81	100	2280.84	100	2280.82	100

Table 20. Projected LCLU distribution for 2019, 2029, and 2039 (km² and %)

Forests cover 41.24% of the area in 2029, with a small decline to 44.11% in 2039; their percentage is 46.03%. With a proportion of 30.62% in 2019 and 32.39% in 2029, the agricultural class comes in as the second biggest category. Grasslands also have a significant abundance, although with time this decreases. Urban areas see a growth rate of 7.05%, up from 6.14% in 2019 to 2039; industrial land stabilises at around 2%. Conversely, the areas of transitional land, water bodies, and bare surfaces exhibit a decreasing trend. Below, we explain a more detailed change analysis for LCLU prediction classes, based on the data presented in Table 11 and Figure 34.

Agricultural. From 2019 to 2029 (see Figure 31 as well), agricultural land expanded by 40.43 km² (+1.77%), while, in the second period from 2029 to 2039, it declined by 24.17 km² (-1.06%), due to urban or industrial expansion or transitional land class transformation. Despite this, agriculture saw a net gain of 16.25 km² (+0.71%) over the whole period (2019–2039) with a notable slowdown in the second decade.

LCLU classes	2019 -2029	2029-2039	2019-2039

	(Δ km^2)	%	(Δ km^2)	%	(Δ km^2)	%
Water bodies	-0.61	-0.03	-0.77	-0.03	-1.39	-0.06
Urban	8.35	0.37	12.28	0.54	20.63	0.90
Transitional land	-87.31	-3.83	60.75	2.66	-26.57	-1.16
Industrial	-5.01	-0.22	4.27	0.19	-0.74	-0.03
Grassland	-49.84	-2.19	-13	-0.57	-62.82	-2.76
Forest	109.31	4.79	-43.84	-1.92	65.47	2.87
Bare surfaces	-15.32	-0.67	4.49	0.20	-10.82	-0.47
Agricultural	40.43	1.77	-24.17	-1.06	16.25	0.71

Table 21. Projected LCLU changes, 2019–2039 (km² and %)

Bare Surfaces. This class saw a decline in the first period (2019–2029) by decreasing by 15.31 km² (-0.67%), indicating a conversation to other classes. In the second decade, a small net gain occurred with 4.49 km^2. (+0.20%), while over the full period, bare surfaces experienced a net loss of 10.82 km² (-0.47%), indicating the trend transformation to the other classes.

Forest. Forest classes show a significant gain in the first decade (2019–2029), reaching 109.36 km² (4.79%). However, in the second decade, it decreased by 43.84 sq. km² (-1.91%). Despite this, during the whole period (2019–2039), the forest area gained 65.47 sq. km^2. (+2.87%).

Grassland. The grasslands class showed a consistent decline in the first period (2019 to 2029) with 49.82 km² (-2.18%), continuing to lose in the second period (2029 to 2039) with 13.00 km² (-0.57%), resulting in a total loss of 62.82 km² (-2.76%) during the whole period. This suggests continuous conversion into other land cover or uses, such as transitional land, agriculture, industrial, or urban, etc.

Industrial. In contrast to the urban class, the industrial class declined by 5.01 km² (–0.22%) during the first period, followed by an increase of 4.28 km² (+0.19%) in the second period. Throughout the entire period, the industrial class experienced a net loss of 0.74 km^2 (-0.03%).

Transitional Land. The transitional class experienced a significant loss of 87.31 km² (–3.83%) during the first period, followed by a gain of 60.75 km² (+2.66%) in the second

period. Overall, despite a net decline of 26.57 km² (–1.16%) across the entire study period, the class shows a slight decreasing trend.

Urban. Urban class has grown steadily in both decades. In the first period, 2019 to 2029, it increased by 8.35 km² (+0.37%), continuing to increase with 12.28 km² (+0.54%) in the second period, resulting in a 20.63 km² (+0.90%) gain during the full period of the study area. This growth is attributed to population growth and infrastructure development.

Water Bodies. Water bodies class saw a decline in trends across both periods, losing 0.61 km² (-0.03%) in the first decade (2019 to 2029) and further increasing with 0.78 km² (-0.03%) in the second decade, resulting in 1.39 km² (-0.06%) over the entire period.

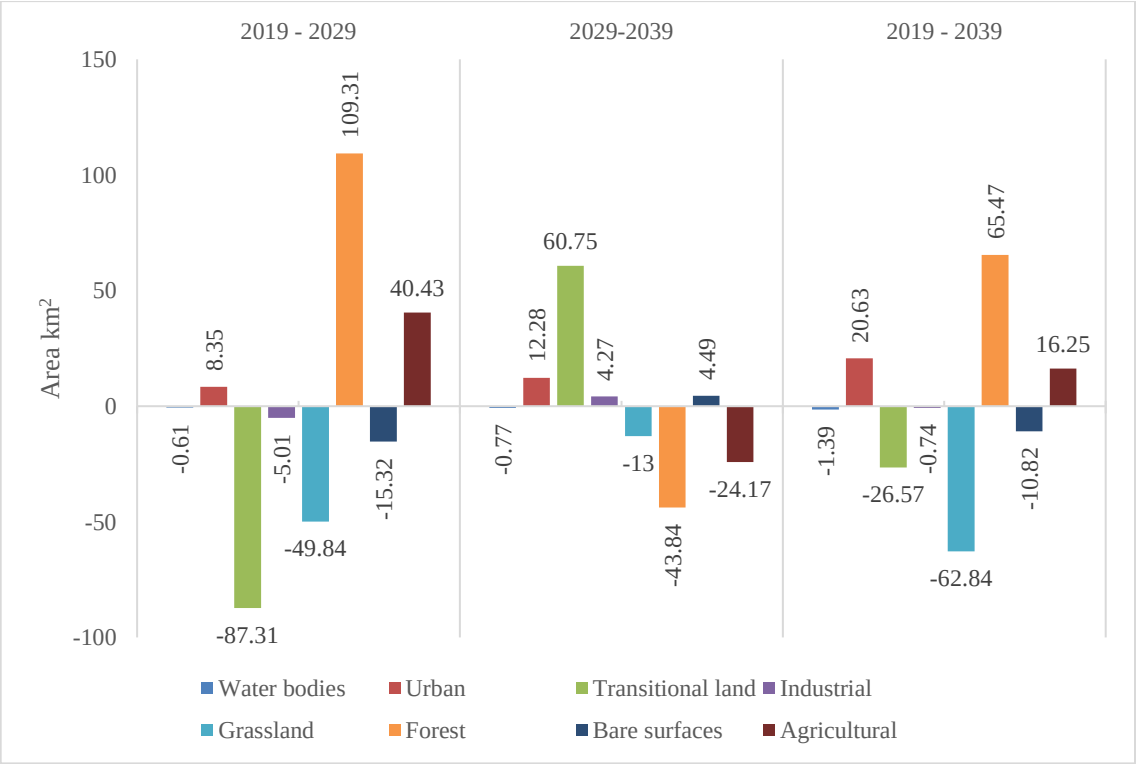

Figure 35. Predicted LCLU gains and losses, 2019–2039.

6. CONCLUSIONS AND RECOMMENDATIONS

In this study, spatial changes in land cover and use were successfully analysed during 18 years (2001–2019) in the Prishtina region. This was achieved using remote sensing technology and key steps, including image classification, change detection, and prediction of how eLCLU classes will be in the future. The classification was carried out primarily using multi-temporal images from Landsat 5, 7, and 8 sensors. Complementary data, including local orthophotos and very high-resolution images from Google Earth, ensured the collection of high-quality samples for classifying LCLU categories in the study area. But when the samples for the eight class categories were looked at, it was clear that images with similar reflective values could lead to mistakes when putting them into the wrong class. Therefore, we utilised numerous time series images over a year. We implemented the supervised image classification method using four different algorithms: MD, ML, SVM-RBF, and NN. These last two are also known as Machine Learning algorithms. Accuracy evaluation results, including Kappa and OA, indicate that traditional algorithms such as MD and ML performed poorly in classification. The highest classification result for the map in 2001 was given by the SVM-RBF algorithm, while for the two LCLU maps in 2009 and 2019, the NN algorithm performed better.

According to their interpretation, the spatial distribution of each LCLU class for the study area was also understood, with the forest and agricultural classes dominating and the water bodies to a lesser extent. These maps, along with the transitional probability matrix, also made it possible to see changes. From 2001 to 2019, it was clear that the urban and industrial classes were growing faster than the agricultural class, especially as time went on. This shows that the study area is experiencing urban and industrial growth, which is a phenomenon for post-transition and war regions. To see if this trend will continue in the future, the ANN and CA model was used. The LCLU time series from 2001 to 2019 and spatial variables like distance from roads, rivers, terrain, etc. were used to make predictions for the time series in 2019, 2029, and 2039. Also, the validation of the actual 2019 series with the predicted 2019, with an above-average Kappa accuracy, series showed that this model can be used to predict future LCLU changes for this region. The 2029 and 2039 series predictions revealed a growth trend in urbanisation in the future. Meanwhile, the other classes showed fluctuations—losses and decreases in their surfaces in the predicted models. We can say that the findings of this study show that the use of geospatial technology—

remote sensing—is valuable in creating, monitoring, and predicting LCLU inventories. These inventories would help environmentalists, planners, policy makers, etc., to see the trend of changes and to take measures for sustainable strategies for LCLU. Furthermore, future research should incorporate additional data with a higher spatial resolution, followed by more advanced algorithms and using online platforms like Google Earth Engine, to take into account other spatial, socio-economic, and climatic variables.

7. SUMMARY

Our research analysed the spatial extent of LCLU from 2001 to 2019, as well as predicted future changes from 2019 to 2039 in the Prishtina region. Satellite data from the Landsat TM5 sensor series were used to create the LCLU of 2009, ETM+7 of 2001, and OLI8 of 2019 through the supervised classification method. The sample classes collected to train the algorithm—an essential step in this method—often exhibited overlap. We quantitatively assessed the samples using the JM distance measure for spectral differences, in addition to the qualitative assessment. While the water bodies class showed the highest spectral dissimilarity of 2.0 among all classes, it was the grassland and transitional land classes that showed the lowest spectral dissimilarity, above 1.50 (year 2009), which would result in misclassification. We split the samples in a ratio of 80% for training and 20% for classifier validation to perform the classification.

Out of the four classifiers that were applied, namely MD, ML, SVM-RBF, and NN, an accuracy assessment revealed that the SVM-RBF classifier performed best for the year 2001, with an OA of 87.21% and a 0.83 kappa coefficient. The NN classifier, on the other hand, demonstrated an OA of 87.21% and a 0.83 KC for the year 2009 and an accuracy of 81.86% and a 0.77 KC in 2019. We selected these classifications for further analysis based on their accuracy. Based on the LCLU 2019 map, the largest spatial distribution of 940.63 km², or 41.24%, is over forest, then agricultural with 698.45 km², or 30.62%, and the least is with 5.51 km², or 0.24%, that of water bodies. We also analysed the changes in the series using the transition matrix tables. The agricultural class experienced a decreasing of -111.25 km² during the entire study period of 2001–2019; the water bodies class also experienced a contraction during the entire period of -1.65 km². On the other hand, the urban class had a continuous increase during the entire period with 47.71 km², and the industrial class had 24.16 km². Other classes, such as the forest class and the transitional land class, experienced fluctuations between periods.

Using transition probability matrices, we were able to understand the losses and gains of areas between classes. As expected, the urban and industrial classes grew at the expense of the agricultural classes, which is mainly related to the rapid trend of urban, infrastructural, and industrial-commercial development in this region. As a result of applying the ANN and CA methods, it was possible to predict the change of land area for the 20-year period (2019–

2039). The validation of the transnational potential modelling resulted in an average kappa value of 0.71 in 2019, 0.73 in 2029, and 0.70 in 2039.

According to the results from the predicted maps, the urban class is projected to continue its growth from 2019 to 2039, reaching an area of 20.63 km², the forest class 2.87 km², and the agricultural class 0.71 km². On the other hand, the water bodies class is expected to decrease during the entire period by -1.39, while the other classes will have fluctuations between periods that will result in losses during the entire period. These results demonstrate the successful application of remote sensing for monitoring and forecasting LCLU, while also supporting the development of policies for sustainable land management and environmental protection.

8. THESIS

1. It aims to analyse the spatiotemporal evolution of LCLU changes in the Prishtina region from 2001 to 2019 using multi-temporal and multi-stack Landsat imagery and supervised Machine Learning classification methods.

2. Exploring how optimising training samples and classifier parameters can improve classification reliability and why similar spectral signatures can lead to misclassification among LCLU categories.

3. The aim is to utilise and compare the performances of the Machine and Deep Learning methods (MD, ML, SVM-RBF, NN) for LCLU mapping in the study area and assess classification accuracy to identify the most suitable algorithm for complex urban and rural landscape classification.

4. To explore and apply the LCLU change methods for quantifying the changes and investigate the socio-economic driving factors in the modelling.

5. The goal is to predict how the LCLU will change in the study area from 2019 to 2039, using a Deep Learning (CA-ANN) model, different types of spatial variables, and transitional probability matrices. Moreover, the validation of the predicted model is a key to understanding the properties of functions.

Acknowledgment

I am grateful to:

- my supervisor, Dr. Géza Király, for his helpful assistance, counsel, and encouragement in developing the thesis,
- all my colleagues at the Institute of Geomatics and Civil Engineering, for their hospitality and help throughout my study visits,
- all my colleagues from the Department of Geography and the Faculty of Mathematical and Natural Sciences at University of Prishtina, for their spiritual support,
- I am particularly grateful to those who assisted me with language editing and proofreading, ensuring clarity and precision in the final version of this work.

Last but not least, I would like to extend my heartfelt appreciation to my family and friends, whose unconditional love, patience, and encouragement gave me the strength to persevere during challenging times.

Sopron, 2025

Ferat Krasniqi

9. REFERENCES

Albertz, J. (2007). *Einführung in die Fernerkundung: Grundlagen der Interpretation von Luft- und Satellitenbildern* [Introduction to remote sensing: Basics of interpreting aerial and satellite images]. Wissenschaftliche Buchgesellschaft.

Almeida, C. M., Gleriani, J. M., Castejon, E. F., & Soares-Filho, B. S. (2008). Using neural networks and cellular automata for modeling intra-urban land-use dynamics. *International Journal of Geographical Information Science, 22*(9), 943–963. https://doi.org/10.1080/13658810701717867

Bakker, W. H., Feringa, W., Gieske, A. S., Gorte, B. G., Grabmaier, K. A., Hecker, C. A., … Woldai, T. (2001). *Principles of remote sensing*. International Institute for Geo-Information Science and Earth Observation (ITC).

Benediktsson, J. A., & Sveinsson, J. R. (1997). Feature extraction for multisource data classification with artificial neural networks. *International Journal of Remote Sensing, 18*(4), 727–740. https://doi.org/10.1080/014311697218530

Bischof, H., Schneider, W., & Pinz, A. J. (1992). Multispectral classification of Landsat images using neural networks. *IEEE Transactions on Geoscience and Remote Sensing, 30*(3), 482–490. https://doi.org/10.1109/36.134085

Bonham-Carter, G. F. (1994). *Geographic information systems for geoscientists: Modelling with GIS*. Elsevier.

Büttner, G., Kosztra, B., Maucha, G., Pataki, R., Kleeschulte, S., Hazeu, G., Vittek, M., Schröder, C., & Littkopf, A. (2021). *Copernicus Land Monitoring Service CORINE Land Cover user manual*. European Environment Agency. https://www.eea.europa.eu/publications/technical_report_2007_17

Campbell, J. B., & Wynne, R. H. (2011). *Introduction to remote sensing* (5th ed.). Guilford Press.

Campbell, J. D., Lusch, P. D., Smucker, P. D., & Wangui, E. E. (2003). Root causes of land use change in the Loitokitok area, Kajiado District, Kenya. *LUCID Working Paper Series, 19,* 1–37. https://cgspace.cgiar.org/handle/10568/1906

Canada Centre for Remote Sensing. (2019). *Fundamentals of remote sensing*. Natural Resources Canada. https://naturalresources.canada.ca/sites/nrcan/files/earthsciences/pdf/resource/tutor/fundam/pdf/fundamentals_e.pdf

Cheng, Q., & Agterberg, F. P. (1999). Fuzzy weights of evidence method and its application in mineral potential mapping. *Natural Resources Research, 8*(1), 27–35. https://doi.org/10.1023/A:1021631613503

China National Space Administration. (n.d.). *Gaofen and Yaogan missions*. http://www.cnsa.gov.cn

CNES (Centre National d'Études Spatiales). (n.d.). *How to prepare SPOT Vegetation C1/C2*. European Space Agency. https://earth.esa.int/web/sppa/documentation/generic-documentation/how-to-prepare-spot-vegetation-c1-c2

Cochran, W. G. (1977). *Sampling techniques* (3rd ed.). John Wiley & Sons.

Congalton, R. G. (1991). A review of assessing the accuracy of classifications of remotely sensed data. *Remote Sensing of Environment, 37*(1), 35–46. https://doi.org/10.1016/0034-4257(91)90048-B

Congalton, R. G. (2001). Accuracy assessment and validation of remotely sensed and other spatial information. *International Journal of Wildland Fire, 10*(4), 321–328. https://doi.org/10.1071/WF01031

Congalton, R. G., & Green, K. (2009). *Assessing the accuracy of remotely sensed data: Principles and practices* (2nd ed.). CRC Press. https://doi.org/10.1201/9781420055139

Congedo, L. (n.d.). Accuracy. In *Semi-Automatic Classification Plugin manual*. Retrieved September 9, 2022, from https://semiautomaticclassificationmanual.readthedocs.io/en/latest/remote_sensing.html#accuracy-assessment

Congedo, L. (2021). Semi-automatic classification plugin: A Python tool for the download and processing of remote sensing images in QGIS. *Journal of Open Source Software, 6*(64), 3172. https://doi.org/10.21105/joss.03172

Copernicus. (2023, March 12). *CORINE Land Cover (CLC) inventory*. Copernicus Land Monitoring Service. https://land.copernicus.eu/pan-european/corine-land-cover

Copernicus. (n.d.). *CORINE Land Cover (CLC) database*. Copernicus Land Monitoring Service. Retrieved September 10, 2025, from https://land.copernicus.eu/pan-european/corine-land-cover

Coppin, P., & Bauer, M. (1996). Digital change detection in forest ecosystems with remote sensing imagery: A review. *Remote Sensing Reviews, 13*(3–4), 207–234. https://doi.org/10.1080/02757259609532305

Coppin, P., Jonckheere, I., Nackaerts, K., Muys, B., & Lambin, E. (2004). Digital change detection methods in ecosystem monitoring: A review. *International Journal of Remote Sensing, 25*(9), 1565–1596. https://doi.org/10.1080/0143116031000101675

Cortes, C., & Vapnik, V. (1995). Support-vector networks. *Machine Learning, 20*(3), 273–297. https://doi.org/10.1007/BF00994018

Cristianini, N., & Shawe-Taylor, J. (2000). *An introduction to support vector machines and other kernel-based learning methods*. Cambridge University Press.

Dabboor, M., Howell, S., Shokr, M., & Yackel, J. (2014). The Jeffries–Matusita distance for improved sea ice classification from RADARSAT-2 data. *Remote Sensing, 6*(5), 3742–3762. https://doi.org/10.3390/rs6053742

Deer, P. (1995). Digital change detection techniques: Some recent developments. *International Institute for Aerospace Survey and Earth Sciences (ITC).*

Di Gregorio, A., & Jansen, L. J. M. (1998). *Land cover classification system (LCCS): Classification concepts and user manual*. Food and Agriculture Organization of the United Nations.

Di Gregorio, A., & Jansen, L. J. M. (2005). *Land cover classification system (LCCS): Classification concepts and user manual* (Version 2). Food and Agriculture Organization of the United Nations. https://www.fao.org/3/y7220e/y7220e00.htm

DigitalGlobe. (n.d.). *QuickBird* [Satellite]. DigitalGlobe. https://www.digitalglobe.com/products/quickbird

Dutta, S., Das, S., & Paul, R. (2016). Geospatial analysis of land use/land cover change using weights of evidence modeling. *Journal of Environmental Management, 182,* 601–621. https://doi.org/10.1016/j.jenvman.2016.07.040

Eastman, J. R., Jin, W., Kyem, P. A. K., & Toledano, J. (2013). *Raster procedures for multi-criteria/multi-objective decisions*. Clark Labs, Clark University.

Esri. (2023). *ArcGIS Pro user guide*. Environmental Systems Research Institute.

European Space Agency. (n.d.). *Sentinel-2 mission*. Copernicus – The Sentinel Missions. https://sentinel.esa.int/web/sentinel/missions/sentinel-2

European Space Agency. (n.d.). *WorldCover dataset*. https://esa-worldcover.org/en

European Space Agency. (n.d.). *WorldView mission*. European Space Agency. https://earth.esa.int/eogateway/missions/worldview

Fisher, P., Comber, A., & Wadsworth, R. (2005). Land use and land cover: Contradiction or complement. In P. Fisher & D. Unwin (Eds.), *Re-presenting GIS* (pp. 85–98). John Wiley & Sons.

Foody, G. M. (1994). The use of supervised training area selection in classification of remotely sensed data. *International Journal of Remote Sensing, 15*(5), 1113–1131. https://doi.org/10.1080/01431169408954150

GeeksforGeeks. (2025, February 4). *Multi-layer perceptron learning in TensorFlow*. GeeksforGeeks. https://www.geeksforgeeks.org/multi-layer-perceptron-learning-in-tensorflow/

GeeksforGeeks. (n.d.). *Types of neural networks*. GeeksforGeeks. Retrieved September 10, 2025, from https://www.geeksforgeeks.org/types-of-neural-networks

Giacinto, G., & Roli, F. (2001). Design of effective neural network ensembles for image classification purposes. *Image and Vision Computing, 19*(9–10), 699–707. https://doi.org/10.1016/S0262-8856(01)00036-6

Herold, M., Couclelis, H., & Clarke, K. C. (2005). The role of spatial metrics in the analysis and modeling of urban land use change. *Computers, Environment and Urban Systems, 29*(4), 369–399. https://doi.org/10.1016/j.compenvurbsys.2003.12.001

Hosmer, D. W., Lemeshow, S., & Sturdivant, R. X. (2013). *Applied logistic regression* (3rd ed.). Wiley. https://doi.org/10.1002/9781118548387

Hsu, C.-W., Chang, C.-C., & Lin, C.-J. (2010). *A practical guide to support vector classification*. National Taiwan University. https://www.csie.ntu.edu.tw/~cjlin/papers/guide/guide.pdf

ITC. (n.d.). *Concept: Feature space*. International Institute for Geo-Information Science and Earth Observation. https://ltb.itc.utwente.nl/page/498/concept/81578

ITC. (n.d.). *Concept: Minimum distance algorithm*. International Institute for Geo-Information Science and Earth Observation. https://ltb.itc.utwente.nl/page/498/concept/81518

Jansen, L. J. M., & Di Gregorio, A. (2002). Parametric land cover and land-use classifications as tools for environmental change detection. *Agriculture, Ecosystems & Environment, 91*(1–3), 89–100. https://doi.org/10.1016/S0167-8809(01)00243-2

Jensen, J. R. (2007). *Remote sensing of the environment: An earth resource perspective* (2nd ed.). Pearson Education.

Jensen, J. R., Rutchey, K., Koch, M. S., & Narumalani, S. (1997). Inland wetland change detection in the Everglades Water Conservation Area 2A using a time series of normalized remotely sensed data. *Photogrammetric Engineering & Remote Sensing, 63*(7), 839–849.

Karasiak, N. (2016). *Dzetsaka: Supervised classification plugin for QGIS* (Version 1.0) [Computer software]. QGIS. https://plugins.qgis.org/plugins/Dzetsaka/

Kastrati, B., Ramadani, I., Lika, I., & Ismajli, F. (2014). Demographic changes and internal migration in Kosovo after the 1999 conflict. *[Details needed: journal, report, or conference proceedings]*.

Khatami, R., Mountrakis, G., & Stehman, S. V. (2016). A meta-analysis of remote sensing research on supervised pixel-based land-cover image classification processes: General guidelines for practitioners and future research. *Remote Sensing of Environment, 177*, 89–100. https://doi.org/10.1016/j.rse.2016.02.028

Kulkarni, S. A., & Patil, R. K. (2011). Comparison of artificial neural network and maximum likelihood classification approach for land cover classification using Landsat multispectral data. In *Proceedings of the 2011 IEEE International Conference*

on Computational Intelligence and Computing Research (ICCIC) (pp. 1–4). IEEE. https://doi.org/10.1109/ICCIC.2011.6079300

Lillesand, T. M., Kiefer, R. W., & Chipman, J. W. (2015). *Remote sensing and image interpretation* (7th ed.). Wiley.

Liu, J., & Mason, P. (2016). *Essential image processing and GIS for remote sensing*. Wiley.

Liu, T., Yang, L., & Lunga, D. (2021). Change detection using deep learning approach with object-based image analysis. *Remote Sensing of Environment, 256,* 112308. https://doi.org/10.1016/j.rse.2021.112308

Loveland, T. R., Reed, B. C., Brown, J. F., Ohlen, D. O., Zhu, Z., Yang, L., & Merchant, J. W. (2000). Development of a global land cover characteristics database and IGBP DISCover from 1 km AVHRR data. *International Journal of Remote Sensing, 21*(6–7), 1303–1330. https://doi.org/10.1080/014311600210191

Lu, D., Mausel, P., Brondízio, E., & Moran, E. (2004). Change detection techniques. *International Journal of Remote Sensing, 25*(12), 2365–2407. https://doi.org/10.1080/0143116031000139863

Lu, D., & Weng, Q. (2007). A survey of image classification methods and techniques for improving classification performance. *International Journal of Remote Sensing, 28*(5), 823–870. https://doi.org/10.1080/01431160600746456

Malczewski, J. (2006). GIS-based multicriteria decision analysis: A survey of the literature. *International Journal of Geographical Information Science, 20*(7), 703–726. https://doi.org/10.1080/13658810600661508

Mas, J. F., Kolb, M., Paegelow, M., Camacho Olmedo, M. T., & Houet, T. (2014). Inductive pattern-based land use/cover change models: A comparison of four software packages. *Environmental Modelling & Software, 51,* 94–111. https://doi.org/10.1016/j.envsoft.2013.09.010

Mather, P. M., & Koch, M. (2011). *Computer processing of remotely-sensed images: An introduction* (4th ed.). Wiley.

Matusita, K. (1967). A measure of similarity between distributions. *Annals of the Institute of Statistical Mathematics, 19*(1), 181–190. https://doi.org/10.1007/BF02911662

Mertens, B., & Lambin, E. F. (2000). Land-cover-change trajectories in southern Cameroon. *Annals of the Association of American Geographers, 90*(3), 467–494. https://doi.org/10.1111/0004-5608.00205

Mochizuki, S., & Murakami, T. (2012). Accuracy comparison of land cover mapping using object-oriented classification. *Remote Sensing Letters, 3*(6), 521–528. https://doi.org/10.1080/01431161.2011.644593

Mountrakis, G., Im, J., & Ogole, C. (2011). Support vector machines in remote sensing: A review. *ISPRS Journal of Photogrammetry and Remote Sensing, 66*(3), 247–259. https://doi.org/10.1016/j.isprsjprs.2010.11.001

Muhammad, R., Zhang, W., Abbas, Z., Guo, F., & Gwiazdzinski, L. (2021). Spatiotemporal change analysis and prediction of future land use and land cover changes using QGIS MOLUSCE plugin and remote sensing big data: A case study of Linyi, China. *Environmental Monitoring and Assessment, 193*(7), 1–15. https://doi.org/10.1007/s10661-021-08650-2

NASA Earth Observing System Data and Information System. (n.d.). *MODIS overview*. NASA. https://modis.gsfc.nasa.gov/overview/

NASA Landsat. (n.d.). *Landsat 9 spectral bands*. NASA. https://landsat.gsfc.nasa.gov/satellites/landsat-9/landsat-9-bands/

Nedd, R., Light, K., Owens, M., James, N., Johnson, E., & Anandhi, A. (2021). A synthesis of land use/land cover studies: Definitions, classification systems, meta-studies, challenges and knowledge gaps on a global landscape. *Land, 10*(9), 909. https://doi.org/10.3390/land10090994

NextGIS. (2025). *Modules for Land Use Change Simulations (MOLUSCE)* [QGIS plugin]. NextGIS. https://nextgis.com/molusce/

Olofsson, P., Foody, G. M., Herold, M., Stehman, S. V., Woodcock, C. E., & Wulder, M. A. (2014). Good practices for estimating area and assessing accuracy of land change. *Remote Sensing of Environment, 148*, 42–57. https://doi.org/10.1016/j.rse.2014.02.015

Pal, M., & Mather, P. M. (2005). Support vector machines for classification in remote sensing. *International Journal of Remote Sensing, 26*(5), 1007–1011. https://doi.org/10.1080/01431160512331314083

Pedregosa, F., Varoquaux, G., Gramfort, A., Michel, V., Thirion, B., Grisel, O., Blondel, M., Prettenhofer, P., Weiss, R., Dubourg, V., Vanderplas, J., Passos, A., Cournapeau, D., Brucher, M., Perrot, M., & Duchesnay, É. (2011). Scikit-learn: Machine learning in Python. *Journal of Machine Learning Research, 12*, 2825–2830. http://jmlr.org/papers/v12/pedregosa11a.html

Penn State e-Education Institute. (n.d.). *Spectral response patterns*. In *The nature of geographic information*. Pennsylvania State University. Retrieved September 10, 2025, from https://www.e-education.psu.edu/natureofgeoinfo/node/1906

Pennsylvania State University. (n.d.). *Lesson 18.7: Cohen's Kappa*. Penn State Online: STAT 509. Retrieved September 10, 2025, from https://online.stat.psu.edu/stat509/lesson/18/18.7

Planet Labs. (n.d.). *PlanetScope constellation*. Planet Labs. https://www.planet.com/products/planet-scope/

Pontius, R. G., & Malanson, J. (2005). Comparison of the structure and accuracy of two land change models. *International Journal of Geographical Information Science, 19*(2), 243–265. https://doi.org/10.1080/13658810410001713434

PyCodeMates. (2022, July). *Support vector machines: Detailed overview*. PyCodeMates. https://www.pycodemates.com/2022/07/support-vector-machines-detailed-overview.html

Quinn, G. P. (2001). *Remote sensing applications for natural resource management*. [Publisher details missing — please provide].

Rindfuss, R. R., Walsh, S. J., Turner, B. L., Fox, J., & Mishra, V. (2004). Developing a science of land change: Challenges and methodological issues. *Proceedings of the National Academy of Sciences, 101*(39), 13976–13981. https://doi.org/10.1073/pnas.0401545101

Rodríguez-Galiano, V. F., Ghimire, B., Rogan, J., Chica-Olmo, M., & Rigol-Sánchez, J. P. (2012). An assessment of the effectiveness of a random forest classifier for land-cover classification. *ISPRS Journal of Photogrammetry and Remote Sensing, 67,* 93–104. https://doi.org/10.1016/j.isprsjprs.2011.11.002

Rumelhart, D. E., Hinton, G. E., & Williams, R. J. (1986). Learning representations by back-propagating errors. *Nature, 323*(6088), 533–536. https://doi.org/10.1038/323533a0

Schölkopf, B., & Smola, A. J. (2002). *Learning with kernels: Support vector machines, regularization, optimization, and beyond*. MIT Press.

Schowengerdt, R. A. (2006). *Remote sensing: Models and methods for image processing* (3rd ed.). Elsevier.

Serpico, S. B., & Bruzzone, L. (1999). A new supervised method for change detection in multitemporal SAR images. *IEEE Transactions on Geoscience and Remote Sensing, 37*(3), 1425–1439. https://doi.org/10.1109/36.763302

SEOS Project. (n.d.). *Introduction to remote sensing: Physical basics*. SEOS Project. https://seos-project.eu/remotesensing/remotesensing-c01-p01.html

Sheykhmousa, M., Mahdianpari, M., Ghanbari, H., Mohammadimanesh, F., Ghamisi, P., & Homayouni, S. (2020). Support vector machine versus random forest for remote sensing image classification: A meta-analysis and systematic review. *IEEE Journal of Selected Topics in Applied Earth Observations and Remote Sensing, 13,* 6308–6325. https://doi.org/10.1109/JSTARS.2020.3026724

Sim, J., & Wright, C. C. (2005). The kappa statistic in reliability studies: Use, interpretation, and sample size requirements. *Physical Therapy, 85*(3), 257–268. https://doi.org/10.1093/ptj/85.3.257

Singh, A. (1989). Digital change detection techniques using remotely sensed data. *International Journal of Remote Sensing, 10*(6), 989–1003. https://doi.org/10.1080/01431168908903939

Sokal, R. R. (1974). Classification: Purposes, principles, progress, prospects. *Science, 185*(4157), 1115–1123. https://doi.org/10.1126/science.185.4157.1115

Store, R., & Kangas, J. (2001). Integrating spatial multi-criteria evaluation and expert knowledge for GIS-based habitat suitability modeling. *Landscape and Urban Planning, 55*(2), 79–93. https://doi.org/10.1016/S0169-2046(01)00120-7

Swain, P. H., & Davis, S. M. (1978). *Remote sensing: The quantitative approach*. McGraw-Hill.

Thenkabail, P. S. (2016). *Remote sensing handbook* (Vol. 1). Taylor & Francis Group.

Tso, B., & Mather, P. M. (2009). *Classification methods for remotely sensed data* (2nd ed.). Taylor & Francis Group.

Turner, B. L., Meyer, W. B., & Skole, D. L. (1994). Global land-use/land-cover change: Towards an integrated study. *Ambio, 23*(1), 91–95. https://www.jstor.org/stable/4314168

Turner, W., Rondinini, C., Pettorelli, N., Mora, B., Leidner, A. K., Szantoi, Z., Buchanan, G., Dech, S., Dwyer, J., Herold, M., Koh, L. P., Leimgruber, P., Taubenboeck, H., Wegmann, M., Wikelski, M., & Woodcock, C. (2015). Free and open-access satellite data are key to biodiversity conservation. *Biological Conservation, 182*, 173–176. https://doi.org/10.1016/j.biocon.2014.11.048

United Nations Programme, & Food and Agriculture Organization. (2000). *Land cover classification system: Classification concepts and user manual*. FAO.

U.S. Geological Survey. (n.d.). *Earth Explorer*. U.S. Department of the Interior. Retrieved September 10, 2025, from https://earthexplorer.usgs.gov

U.S. Geological Survey. (n.d.). *Landsat Collection 2*. U.S. Geological Survey. https://doi.org/10.3133/fs20213002

U.S. Geological Survey. (n.d.). *Landsat Collection 2: Surface reflectance scaling*. U.S. Geological Survey. https://www.usgs.gov/core-science-systems/nli/landsat

U.S. Geological Survey. (n.d.). *What are the best Landsat spectral bands for use in my research?* U.S. Geological Survey. Retrieved September 10, 2025, from https://www.usgs.gov/faqs/what-are-the-best-landsat-spectral-bands-use-my-research

U.S. Geological Survey. (2021). *Landsat Collection 2*. U.S. Geological Survey. https://doi.org/10.3133/fs20213002

U.S. Geological Survey. (2022). *Landsat—Earth observation satellites*. U.S. Geological Survey. https://www.usgs.gov/landsat

U.S. Geological Survey. (2023, March 30). *Landsat Next*. U.S. Geological Survey. https://www.usgs.gov/landsat-missions/landsat-next

Vali, A., Comai, S., & Matteucci, M. (2020). Deep learning for land use and land cover classification based on hyperspectral and multispectral Earth observation data: A review. *Remote Sensing, 12*(15), 2495. https://doi.org/10.3390/rs12152495

Vapnik, V. N. (1982). *Estimation of dependences based on empirical data*. Springer.

Vapnik, V. N. (1995). *The nature of statistical learning theory*. Springer. https://doi.org/10.1007/978-1-4757-2440-0

Verburg, P. H., van de Steeg, J., Veldkamp, A., & Willemen, L. (2009). From land cover change to land function dynamics: A major challenge to improve land characterization. *Journal of Environmental Management, 90*(3), 1327–1335. https://doi.org/10.1016/j.jenvman.2008.08.005

Wacker, A. G., & Landgrebe, D. A. (1972). Minimum distance classification in remote sensing (LARS Technical Report No. 25). Laboratory for Applications of Remote Sensing, Purdue University. https://www.lars.purdue.edu/home/references/LTR_030772.pdf

Wulder, M. A. (2019). Current status of Landsat program, science, and applications. *Remote Sensing of Environment, 225,* 127–147. https://doi.org/10.1016/j.rse.2019.02.015

Xia, J., Bombrun, L., Briottet, X., & Chanussot, J. (2017). Hyperspectral image classification with ensemble learning and extended morphological attribute profiles. *IEEE Transactions on Geoscience and Remote Sensing, 55*(6), 3318–3332. https://doi.org/10.1109/TGRS.2017.2669900

Yang, H., Li, S., Zhang, X., & Xu, S. (2017). The standardization and harmonization of land cover classification systems towards harmonized datasets: A review. *ISPRS International Journal of Geo-Information, 6*(5), 154. https://doi.org/10.3390/ijgi6050154

Yuan, D., Elvidge, C. D., & Lunetta, R. S. (1998). Survey of multispectral methods for land cover change analysis. In R. S. Lunetta & C. D. Elvidge (Eds.), *Remote sensing change detection: Environmental monitoring, methods, and applications* (pp. 21–39). Taylor & Francis.

Yuan, F., Sawaya, K. E., Loeffelholz, B. C., & Bauer, M. E. (2005). Land cover classification and change analysis of the Twin Cities (Minnesota) metropolitan area by multitemporal Landsat remote sensing. *Remote Sensing of Environment, 98*(2–3), 317–328. https://doi.org/10.1016/j.rse.2005.08.006

Zhang, T., Wang, L., & Chen, M. (2023). A comparative analysis of SVM-based classification for remote sensing applications. *Remote Sensing Letters, 14*(2), 123–135. https://doi.org/10.1080/2150704X.2023.2165678

Zhu, Z., & Woodcock, C. E. (2012). Object-based cloud and cloud shadow detection in Landsat imagery. *Remote Sensing of Environment, 118,* 83–94. https://doi.org/10.1016/j.rse.2011.10.028

Zhu, Z., Wang, S., & Woodcock, C. E. (2015). Improvement and expansion of the Fmask algorithm: Cloud, cloud shadow, and snow detection for Landsats 4–7, 8, and Sentinel-2 images. *Remote Sensing of Environment, 159,* 269–277. https://doi.org/10.1016/j.rse.2014.12.014

Appendices

Appendix A. Supplementary tables

Table A1. Error matrix for MD classification, 2001.

		Reference data (pixels)								
Classification data (pixels)	LCLU	Ag	Bs	Fo	Gr	In	Tl	Ur	Wb	Total
	Ag	2075	1	3	162	48	74	70	0	2433
	BS	703	488	3	216	42	84	17	6	1559
	Fo	439	7	2580	310	0	49	4	0	3389
	Gr	500	134	88	603	5	191	46	0	1567
	In	9	1	0	7	332	45	184	0	578
	Tl	445	26	24	247	23	229	43	0	1037
	Ur	309	4	2	199	52	36	469	0	1071
	Wb	0	0	33	0	0	0	0	210	243
	Total	4480	661	2733	1744	502	708	833	216	11877

Table A2. Error matrix for ML classification, 2001.

		Reference data (pixels)								
Classification data (pixels)	LCLU	Ag	Bs	Fo	Gr	In	Tl	Ur	Wb	Total
	Ag	3780	3	15	128	44	24	41	5	4037
	Bs	3	551	2	139	0	25	0	0	720
	Fo	13	3	2602	47	0	53	3	0	2721
	Gr	362	63	42	1161	1	98	17	0	1744
	In	83	12	2	32	360	76	69	1	635
	Tl	190	26	63	231	28	429	3	2	972
	Ur	49	6	7	6	69	3	700	0	840
	Wb	0	0	0	0	0	0	0	208	208
	Total	4480	661	2733	1744	502	708	833	216	11877

Table A3. Error matrix SVM-RBF classification for the year 2001.

		Reference data (pixels)								
Classification data	LCLU	Ag	Bs	Fo	Gr	In	Tl	Ur	Wb	Total
	Ag	4174	24	27	244	80	127	101	0	4777
	BS	13	498	3	59	13	24	0	0	610
	Fo	40	6	2643	170	0	100	1	1	2961
	Gr	166	112	50	1200	0	148	7	0	1683
	In	6	15	0	9	340	77	67	0	514

	Tl	46	5	7	53	1	230	15	0	357
	Ur	35	1	3	0	68	2	642	0	751
	Wb	0	0	0	9	0	0	0	215	224
	Total	4480	661	2733	1744	502	708	833	216	11877

Table A4. Error matrix for NN classification for the year 2001

		Reference data (pixels)								
Classification data (pixels)	LCLU	Ag	Bs	Fo	Gr	In	Tl	Ur	Wb	Total
	Ag	99	243	70	0	71	4126	26	35	4670
	BS	0	72	19	0	1	8	4	413	517
	Fo	0	76	72	0	0	16	2604	3	2771
	Gr	13	1143	95	0	8	193	77	119	1648
	In	46	15	100	0	361	15	0	27	564
	Tl	20	192	349	0	15	91	22	63	752
	Ur	655	3	2	0	46	22	0	1	729
	Wb	0	0	1	216	0	9	0	0	226
	Total	833	1744	708	216	502	4480	2733	661	11877

Table A5. Error matrix for MD classification, 2009.

		Reference data (pixels)								
Classification data (pixels)	LCLU	Ag	Bs	Fo	Gr	In	Tl	Ur	Wb	Total
	Ag	1548	1	2	155	9	101	143	0	1959
	BS	538	274	0	93	74	204	49	6	1238
	Fo	159	0	1738	89	0	113	2	0	2101
	Gr	1067	39	52	892	0	231	153	0	2434
	In	47	2	0	0	478	0	222	0	749
	Tl	565	134	57	326	7	358	49	2	1498
	Ur	627	110	0	128	67	24	583	0	1539
	Wb	0	0	109	0	0	9	0	170	288
	Total	4551	560	1958	1683	635	1040	1201	178	11806

Table A6. Error matrix for ML classification, 2009.

		Reference data (pixels)								
Classification data	LCLU	Ag	Bs	Fo	Gr	In	Tl	Ur	Wb	Total
	Ag	4105	0	8	132	3	84	59	3	4394
	BS	14	518	0	180	2	73	0	0	787
	Fo	15	0	1889	14	0	116	0	0	2034
	Gr	197	11	4	1197	1	150	7	0	1566

	In	13	6	0	1	543	7	77	17	664
	Tl	180	23	55	155	25	602	10	0	1050
	Ur	27	2	2	4	62	8	1048	0	1153
	Wb	0	0	0	0	0	0	0	158	158
	Total	4551	560	1958	1683	635	1040	1201	178	11806

Table A7. Error matrix SVM-RBF classification for the year 2009.

		Reference data (pixels)								
Classification data (pixels)	LCLU	Ag	Bs	Fo	Gr	In	Tl	Ur	Wb	Total
	Ag	4172	79	14	278	31	339	118	0	5031
	BS	42	446	1	74	5	10	0	1	579
	Fo	27	0	1900	51	0	114	0	0	2092
	Gr	138	19	4	1206	0	210	1	0	1578
	In	0	6	0	0	549	0	69	0	624
	Tl	108	8	39	74	0	365	1	0	595
	Ur	64	2	0	0	50	2	1012	0	1130
	Wb	0	0	0	0	0	0	0	177	177
	Total	4551	560	1958	1683	635	1040	1201	178	11806

Table A8. Error matrix for NN (Neural Net) classification for the year 2009

		Reference data (pixels)								
Classification data (pixels)	LCLU	Ag	Bs	Fo	Gr	In	Tl	Ur	Wb	Total
	Ag	4370	26	10	293	33	236	82	0	5050
	BS	13	516	4	69	12	4	5	0	623
	Fo	14	0	1825	14	0	44	0	0	1897
	Gr	101	9	3	1260	0	178	0	0	1551
	In	1	3	0	0	505	1	44	1	555
	Tl	32	6	113	47	4	575	2	0	779
	Ur	20	0	3	0	81	2	1068	0	1174
	Wb	0	0	0	0	0	0	0	177	177
	Total	4551	560	1958	1683	635	1040	1201	178	11806

Table A9. Error matrix of MD classification for the year 2019

		Reference data (pixels)								
Classification	LCLU	Ag	Bs	Fo	Gr	In	Tl	Ur	Wb	Total
	Ag	1114	223	1	135	17	34	57	0	1581
	BS	590	324	18	33	130	77	138	5	1315
	Fo	105	2	2204	172	0	92	0	0	2575

	Gr	1316	40	137	727	10	199	40	0	2469
	In	89	1	17	0	275	3	187	0	572
	Tl	722	70	59	170	26	188	15	1	1251
	Ur	702	115	10	201	119	61	773	0	1981
	Wb	0	0	101	0	10	0	0	194	305
	Total	4638	775	2547	1438	587	654	1210	200	12049

Table A10. Error matrix of ML classification for the year 2019

		Reference data (pixels)								
Classification data (pixels)	LCLU	Ag	Bs	Fo	Gr	In	Tl	Ur	Wb	Total
	Ag	3868	2	10	143	41	34	41	0	4139
	BS	3	687	2	85	25	6	0	0	808
	Fo	9	4	2326	43	0	124	0	0	2506
	Gr	285	42	84	940	2	140	6	0	1499
	In	108	10	40	4	343	12	80	15	612
	Tl	252	24	83	218	35	323	15	0	950
	Ur	113	6	2	5	141	15	1068	1	1351
	Wb	0	0	0	0	0	0	0	184	184
	Total	4638	775	2547	1438	587	654	1210	200	12049

Table A11. Error matrix SVM-RBF classification for the year 2019

		Reference data (pixels)								
Classification data (pixels)	LCLU	Ag	Bs	Fo	Gr	In	Tl	Ur	Wb	Total
	Ag	198	0	0	0	0	0	0	0	198
	BS	0	1032	2	103	1	2	0	49	1189
	Fo	0	2	138	1	82	25	11	112	371
	Gr	2	52	28	368	1	28	24	118	621
	In	0	1	168	5	979	78	135	149	1515
	Tl	0	0	148	0	46	2391	3	55	2643
	Ur	0	0	20	7	5	0	557	21	610
	Wb	0	123	150	103	324	23	45	4134	4902
	Total	200	1210	654	587	1438	2547	775	4638	12049

Table A12. Error matrix fo NN (Neural Net) classification for the year 2019

		Reference data (pixels)								
Classificati	LCLU	Ag	Bs	Fo	Gr	In	Tl	Ur	Wb	Total
	Ag	4035	2	15	257	49	72	54	0	4484
	BS	10	495	0	12	16	1	1	0	535

	Fo	50	7	2406	50	0	155	0	0	2668
	Gr	228	236	54	1070	47	169	4	0	1808
	In	128	8	35	9	351	28	57	4	620
	Tl	110	27	29	38	11	217	0	1	433
	Ur	77	0	8	2	95	12	1094	0	1288
	Wb	0	0	0	0	18	0	0	195	213
	Total	4638	775	2547	1438	587	654	1210	200	12049